SUPPRESSION OF DISORDER-INDUCED SCATTERING IN OPTOMECHANICAL SYSTEMS

BY

SEUNGHWI KIM

DISSERTATION

Submitted in partial fulfillment of the requirements
for the degree of Doctor of Philosophy in Mechanical Engineering
in the Graduate College of the
University of Illinois at Urbana-Champaign, 2018

Urbana, Illinois

Doctoral Committee:

Associate Professor Gaurav Bahl, Chair and Director of Research
Professor Kent D. Choquette
Associate Professor Sanjiv Sinha
Assistant Professor Kejie Fang

Abstract

High-Q optical and mechanical resonators have been utilized in ultra-high precision metrology, transducers, sensor applications, and even investigating quantum mechanics at mesoscales. However, these low-loss devices are often limited by sub-wavelength fluctuations within the host material, that may be frozen-in or even dynamically induced. Rayleigh scattering is observed in nearly all wave-guiding technologies today and can lead to both irreversible radiative losses as well as undesirable intermodal coupling. The mitigation of disorder-induced scattering is extremely challenging for micro and nanoscale devices, as surface roughness, which causes Rayleigh scattering, is unavoidable in microfabrication processes (Appl Phys Lett 85, 17, 2004; J Lightwave Technol 24, 12, 2006). Minimizing disorder-induced Rayleigh backscattering has thus been a significant challenge until now. It has been shown that backscattering from disorder can be suppressed by breaking time-reversal symmetry in magneto-optic (Sov Phys JETP, 59, 1, 1984; Phys Rev B, 37, 1988) and topological insulator materials (Phys Rev B, 38, 1988; Nature, 461, 7265, 2009). Yet, common monolithic dielectrics, which are basic building ingredients of high-Q resonators, possess neither of these properties.

Fortunately, we develop a novel technique to break time-reversal symmetry without magneto-optic in a high-Q optical cavity pumped by a single-frequency laser through parity-selective optomechanics. Such optomechanical interaction is achieved

by Brillouin scattering, owing to the phase-matching condition. This method enables complete linear optical isolation without requiring magnetic fields. Instead, the isolation originates from a nonreciprocal induced transparency based on a coherent light-sound interaction, where light and sound are coupled bv a traveling-wave Brillouin scattering interaction. That breaks time-reversal symmetry within the waveguide-resonator system. Our result demonstrates that material agnostic and wavelength-agnostic optical isolation is far more accessible in chip-scale photonics than previously thought. However, isolators block backscattering from systems, but cannot prevent disorder-induced backscattering inherently.

In order to minimize disorder-induced backscattering, we experimentally demonstrate robust phonon transport in the presence of material disorder. This is achieved by explicitly inducing chirality through the parity-selective optomechanical coupling. We show that asymmetric optical pumping of a symmetric resonator enables a dramatic chiral cooling of clockwise and counterclockwise phonons, while simultaneously suppressing the hidden action of disorder. Surprisingly, this passive mechanism is also accompanied by a chiral reduction in heat load leading to optical cooling of the mechanics without added damping, an effect that has no optical analog. This technique can potentially improve upon the fundamental thermal limits of resonant mechanical sensors, which cannot be attained through sideband cooling.

This new mechanism can be also expanded to the optics domain, where Rayleigh scattering severely limits the performance of devices in the limit of microscale. We have demonstrated an optomechanical approach for dynamically suppressing Rayleigh light backscattering within optical resonators. Similar to the previous method, we achieve this by locally breaking time-reversal symmetry in a silica resonator through a Brillouin scattering interaction that is available in all materials. Near-complete suppression of Rayleigh backscattering is experimentally confirmed

through three independent measurements – the reduction of the back-reflections caused by scatterers, the elimination of a commonly seen normal-mode splitting effect, and by measurement of the reduction in intrinsic optical loss. More broadly, our results suggest that it is possible to dynamically suppress Rayleigh backscattering within any optical dielectric medium using time-reversal symmetry breaking, for achieving robust light propagation in spite of scatterers or defects. Our proposal is not limited by a specific form of time-reversal symmetry breaking through Brillouin scattering in optical cavities. It can be realized in linear waveguides under different time-reversal symmetry approaches such as acousto-optic, nonlinear-optics, and PT symmetry breaking technique.

Acknowledgments

This dissertation is based on research conducted during my PhD program at Illinois. The cornfield here that I have spent the time is to make me as a genuine researcher with several others, which I used to dream of. That is why I would like to give my thank to people who have worked with me and even supported me during the last five years.

First and foremost, I would like to thank my academic advisor, professor Gaurav Bahl, for the guidance and patience that he has given throughout my PhD program in his group. It has been honored to be one of his students. He sets a good example for being a faculty in the academia, as he is always curious about everything and even leads me whenever I was stuck with my experiments by his incredible intuition. Besides, he has spent his time to correct me in terms of presentation and writing which are essential to scientists, though he was extremely busy at that time. I have truly learned a lot from him, not just science itself, but his careful manner as well.

I also would like to give my thank to the Committee, Professor Kent Choquette, Professor Sanjiv Sinha, Professor Kejie Fang, and the preliminary exam Committee, Professor Yuri Vlasov, and Professor Kimani Toussaint for their useful comments and support to the work included in this thesis.

Also, I would like to express my appreciation to Professor Jacob M. Taylor and his group at the University of Maryland for their contributions to my publications.

Also, I would like to thank Professor Peter Dragic for his suggestions regarding optical fibers.

I have enjoyed working with labmates in Bahl group, and would like to thank, JunHwan Kim, Kewen Han, Shiyi Chen, Yinchung Chen, Donggyu Sohn, Kitt Peterson, Jeewon Suh, Inbar Grinberg, Soonwook Kim, Rhinithaa Thanalakshme, Jianing Zhao, Austen Motily, Peter Sokalski, Cameron Harris, Nathan Dostart, Jafir Haidri, Shengtai Shi, Indronil Ghosh, Anudeep Mangu, Alan Luo, and other students. Especially my credit should go to JunHwan Kim who always discusses with me whenever I have issues with the experiments.

Outside of the labmates, I do give my gratitude to my friends at UIUC, Jongchul Shin, Woowon Lee, Wookyong Lee, Seonghee Cho, and all former members in Korean Church at Champaign-Urbana.

Of course, my thanks go to my wife, Heejin Kim, for all her love, support, and even patience during the last three years. She always looks after me first before herself every time and every day, and helps me always stay motivated. With her devotion and her love that has shown me, I could move forward full of hope in my graduate life.

Finally, I cannot forget to mention my parents and my sister. Although I have been to South Korea just twice during the last five years, they always take care of me and give me their love and encouragement. All works I have done so far is dedicated to my beloved family.

Contents

Chapter 1

Introduction

1.1 Overview

Optical and mechanical devices with low loss are useful for sensing, transducing, and communication applications. However, loss introduced by disorder used to construct such devices limits their performance. For instance, when optical fibers were first developed in the early 20th century, they were not capable of providing long-distance optical communication due to large attenuation induced by small defects in the silica glass media. Kao et al. reported that the attenuation rate per length must be lower than 20 dB/km for achieving optical fiber communications [1]. Researchers eventually reached this theoretical limit by effectively removing disorder in fibers, thus optical fibers are widely used for long-range optical communication today. Since this success, the aim to reduce the effect of disorder has gained broader interest. However, scattering loss induced by disorder is in principle unavoidable, as inhomogeneities exist inherently inside any material and can even be induced during fabrication processes.

1.1.1 Overview of disorder-induced scattering

To address the fundamental challenge created by disorder, we first must understand the physics for disorder-induced scattering loss. In general, scattering loss can be induced by defects inside wave-guiding systems as illustrated in Fig. 1.1(a). Rayleigh scattering occurs when light scatters from defects which are smaller than its wavelength [2]. The intensity of Rayleigh scattering is given by

$$I_{\text{scatter}} \propto \frac{\omega^4}{c^4}(1 + \cos^2 \theta_{\text{sc}}), \tag{1.1}$$

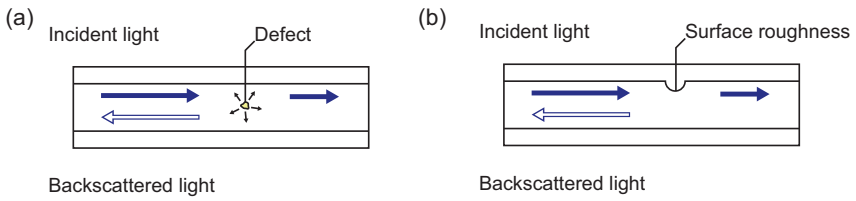

Figure 1.1: (a-b) Schematic of disorder-induced scattering in waveguides. In both cases, backscattered light is partially guided into the systems, and the rest of fields radiates.

where $\theta_{\rm sc}$ is the angle of scattered light by the defects. Equation (1.1) indicates that the scattering intensity is maximized in the forward and backward directions (at $\theta_{\rm sc} = 0$ or π), meaning that disorder-induced scattering is generally due to backscattering.

Surface roughness is the other major cause of scattering loss, as shown in Fig. 1.1(b). Scattering loss from a rough surface is mainly caused by interference between scattered light rays. Figure 1.2(a) shows how specular reflection occurs on a smooth surface, where the scattered light remains coherent.[1] For a slightly rough surface, individual rays incident on the surface can be scattered in different directions, resulting in both specular and diffuse reflections as shown in Fig 1.2(b) [3].[2] When a surface is very rough, incident rays are randomly scattered into every angle as shown in Fig. 1.2(c) [3]. Surprisingly, the scattering intensity in the backward direction can be enhanced by multiple scattering [4] as shown in Fig. 1.2(d).[3]

In principle, each incident light ray scatters from a rough surface many times due to the randomness of the surface, thereby different scattering paths exist. Among the random scattering paths, there is a path which is identical to the incident light path but in the opposite propagating direction, i.e., the time-reversal path as illustrated in Fig. 1.2(d). The constructive interference between these two paths can lead to backscattering enhancement, and it occurs by satisfying the following

[1] Specifically, a group of scattered light fields has an equiphase to give the coherent field, thus the scattered light angle is identical to the incident angle.

[2] In the limit of low scattering intensity, the mean scattering intensity can be analyzed by Kirchhoff theory $\langle I_s(r)\rangle \propto \cos^2\theta_{\rm in}\cos^2\theta_{\rm sc}/r^2\lambda^4$, where $\theta_{\rm in}$ and $\theta_{\rm sc}$ are the angles of incident light and scattered light, respectively.

[3] Similar to coherent backscattering in a disordered media, the incident light path constructively interferes with its time-reversal path because of multiple scattering on a strongly rough surface.

condition [5]:

$$\Delta\phi = \frac{2\pi}{\lambda}(\vec{k}_{in} - \vec{k}_{tr}) \cdot (\vec{r}_n - \vec{r}_1) = 2\pi m,$$

where $\vec{k}_{in}$ and $\vec{k}_{tr}$ are the wave numbers of the incident light and its time-reversal pair, respectively, and m is the integer. $\vec{r}_n$ is the position where individual scatterings happen. Here, $\Delta\phi$ is the phase difference between the two paths. As backscattering from a rough surface can be coherent, it is sometimes referred to as Rayleigh scattering [3, 6].

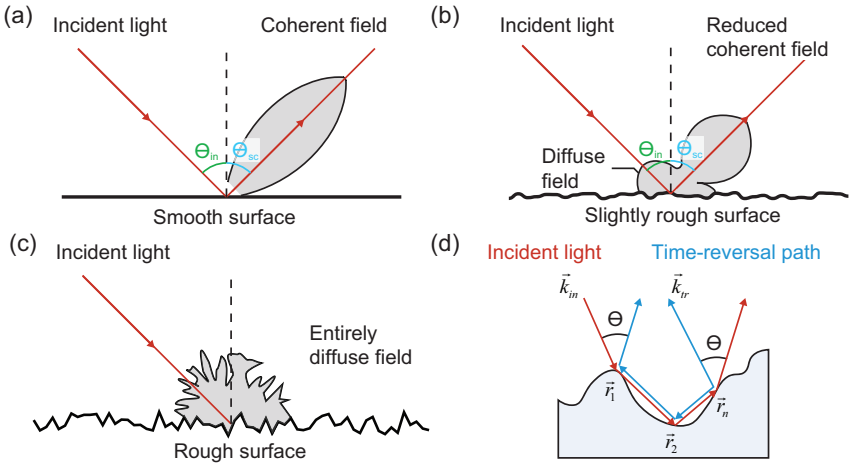

Figure 1.2: Illustration of scattering from surface roughness with increased roughness. (a) The scattered light on the smooth surface is coherent. (b) Due to the destructive inference of scattered fields, the coherent field is reduced and dissipated on the slightly rough surface. (c) The scattered fields are entirely diffused on the rough surface. (d) Schematic of multiple scattering on the rough surface. The incident light (red) $\vec{k}_{in}$ can constructively interfere with the time-reversal path (blue) $\vec{k}_{tr}$ when the phase difference is $2\pi m$, where m is the integer.

Rayleigh scattering is observed in nearly all wave-guiding technologies today, as geometric imperfection is inevitable during the fabrication process. More importantly, disorder-induced backscattering in waveguiding systems can lead to be irreversible radiative losses as well as undesirable intermodal coupling [6, 7, 8, 9, 10, 11]. Rayleigh scattering also occurs in optical whispering gallery mode (WGM) resonators, and leads to limiting photon transport efficiency (See the detailed discussion of WGM resonators in Chapter 2). A fused-silica resonator, as shown in Fig. 1.3(a), is one of the simplest high-Q optical WGM resonators. The fused-silica resonators

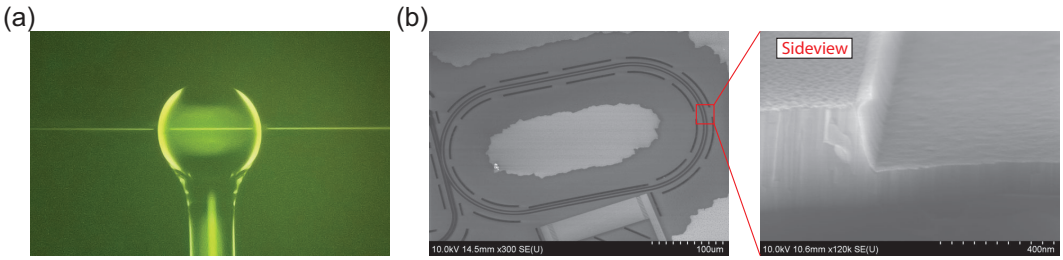

Figure 1.3: (a) Fused-silica microsphere resonator of diameter $\sim 200\ \mu m$. (b) (Left) SEM images of aluminum nitride racetrack resonator. (Right) Sideview of the resonator. The resonator is fabricated by anisotropic etching, therefore it sacrifices its Q-factor by using the RIE etching, due to the surface roughness. Courtesy of Donggyu B. Sohn for (b) photos.

are fabricated by melting glass, which produces an extremely smooth surface. However, the structure of silica is amorphous due to the frozen-in fluctuation during the cooling down process [10]. As a result, silica-based resonators are fundamentally limited by these randomized defects. Compared to amorphous materials, crystalline dielectrics such as Si, Si_3N_4, MgF_2 or CaF_2 have much less random defects. Yet, the crystalline dielectrics suffer from additional surface roughness during the microfabrication processes, such as low resolution of anisotropic etching, or even stitching errors in e-beam lithography as shown in Fig 1.3(b). This inevitable backscattering in both crystalline and amorphous materials causes severe drawback in application at the microscale, such as destabilizing sources, or creating interference in communication systems.

1.1.2 How to mitigate disorder-induced scattering

One of the simplest methods to mitigate disorder-induced scattering is to remove disorder through an annealing process. However, annealing can easily change material properties which can lead to additional difficulties in applications. Alternatively, optical isolators – nonreciprocal devices – are widely used to block backscattering by defects [12]. Nonetheless, optical isolators cannot inherently suppress disorder-induced backscattering, and do not reduce scattering losses.

On the other hand, Golubentsev [13] and John [14] suggested that coherent backscattering inside a disordered medium can be suppressed by breaking time-reversal symmetry through the Faraday rotation. Later, their ideas were experimentally demonstrated by Lenke et al. [15]. Similarly, in 1988 Buttiker also claimed

that the Chern insulators[4] are immune to backscattering from disorder [16]. Wang et al. experimentally demonstrated Buttiker's idea in the microwave domain by using gyrotropic materials [17]. Despite these promising results, these works are only limited to magneto-optic materials whose on-chip integration is not practical. Moreover, as conventional dielectrics are monolithic and topologically trivial, their ideas are not applicable in many photonic and phononic systems.

Inspired by above described ideas, this thesis develops new methods for mitigating disorder-induced scattering in common and monolithic dielectrics. Specifically, I propose an optomechanical approach for dynamically suppressing disorder-induced scattering in phononic and photonic systems using simple whispering gallery mode (WGM) resonators. This is achieved using direction-selective optomechanical interactions that have been utilized to induce nonreciprocity [18, 19, 20]. The direction-selective interactions come from the phase-matching condition via Brillouin interaction [21, 22]. Theses approaches have been experimentally validated in photonic and phononic resonant devices through optomechanical interactions, which are available in conventional materials [23, 24]. A potential future study can extend this technique to on-chip resonators [25] and waveguides [26, 27].

1.2 Thesis organization

The works presented in this dissertation are based on what I have achieved during the Ph.D. program.

Chapter 2 introduces the basic concepts of spherical whispering gallery mode resonators and Brillouin optomechanics. The mode and field distributions are presented both analytically and numerically. Resonator-coupled waveguide systems are also studied by means of the coupled mode theory. A simple theoretical model for studying Brillouin optomechanics is also introduced. Additionally, optical loss mechanisms in waveguiding systems are discussed in detail.

Chapter 3 describes a practical analysis for fabrication and measurement techniques that I have developed so far. Specifically, the experimental methods are well discussed with actual pictures for devices and setups. An understanding of a calibration method in the coupled resonator-waveguide systems is essential to obtain proper measurements. Here, I present the detailed explanation of calibration during

[4]Two dimensional topological insulators not symmetric to the time-reversal operator.

measuring optical transmissions and reflections.

Chapter 4 discusses a basic concept of time-reversal symmetry and how time-reversal symmetry is broken in optics. In particular, breaking time-reversal symmetry through Brillouin scattering is introduced. I experimentally demonstrate an optical isolator from successfully breaking time-reversal symmetry via Brillouin optomechanics [20]. This work has been done with my colleague JunHwan Kim.

Chapter 5 has two parts; the first part discusses Brillouin cooling in a "conventional" Brillouin system having two optical modes, while the second describes suppression of disorder-induced scattering in phonon through Brillouin cooling. The Brillouin cooling – direction-selective – relies on two optical mode shapes, i.e., the optical density of states based on the theoretical model presented here [28]. I demonstrate cooling very close to the strong coupling regime in a room temperature system.

In the second part, I experimentally demonstrate optically induced chirality for phonons in an optomechanical system [23]. This phenomenon shows robust phonon propagation in the presence of disorder, improving phonon coherence. This mechanism is also accompanied by a chiral reduction in heat load leading to optical cooling of the mechanics without added damping. This technique can potentially improve upon the fundamental thermal limits of resonant mechanical sensors.

Chapter 6 presents an optomechanical approach for dynamically suppressing disorder-induced backscattering [24]. I achieve this phenomenon by locally breaking time-reversal symmetry in a silica resonator through a Brillouin scattering interaction. Near complete suppression of disorder-induced backscattering is experimentally confirmed through three independent measurements – the reduction of the back-reflections caused by scatterers, the elimination of a commonly seen normal-mode splitting effect, and by measurement of the reduction in intrinsic optical loss.

Chapter 7 describes alternative methods to break time-reversal symmetry in different platforms, leading to the suppression of disorder-induced scattering. With Yin-Chung Chen, we showed Brillouin cooling for high-velocity phonons is effective, where time-reversal breaking symmetry is achievable in linear waveguides [26]. In Chapter 7, I further analyze how to mitigate disorder-induced backscattering by the Brillouin interaction in waveguides. Additionally, Donggyu B. Sohn and I experimentally demonstrated that time-reversal symmetry can be broken by an acousto-optic interaction in AlN on-chip devices [25]. Such an acousto-optic technique may also be used to suppress disorder-induced backscattering.

Chapter 2

Whispering gallery resonators and Brillouin optomechanics

In this chapter, we will examine Brillouin interactions in the WGM resonators.

2.1 Whispering gallery modes

A specific form of resonators is whispering gallery mode (WGM) resonators set by periodic boundary conditions in a closed topology. Whispering gallery modes were first coined by Lord Rayleigh to investigate the case of St. Paul's Cathedral dome in 1878 [29]. In this case, whispers can be heard distinctly at any other point around the gallery. These acoustic waves are circulating due to repeated reflection, i.e., total internal reflection, and can be confined in the gallery as illustrated in Fig. 2.1(b). Compared to the simple 1D resonator [30] shown in Fig. 2.1(a), the whispering gallery waves travel along the perimeter of the resonator, thereby these waves are in traveling waveforms instead of standing waveforms.[1] The WGMs have a finite lifetime (or a finite Q-factor), as losses can be present through disorder on a surface and even evanescent coupling to environment. It is worth noting that these WGMs have relatively high Q factors compared to other resonators at the similar scale [31, 30].

Interestingly, light in optical cavities can also be confined as WGMs in a similar manner to the acoustic WGMs owing to total internal reflection. Within a dielectric whose refractive index is n, light is traveling along the circumference of the cavity. Particularly, the wavelength for traveling light must be proportional to the perimeter for satisfying the resonance condition in the dielectric $m\lambda/n = 2\pi a$, where λ is the wavelength of light, a is the radius of the cavity, and m is the integer.[2] This

[1] It is because of the periodic boundary condition making closed domain, which is similar to Bloch's theorem.

[2] This integer m corresponds to the azimuthal number which is described later.

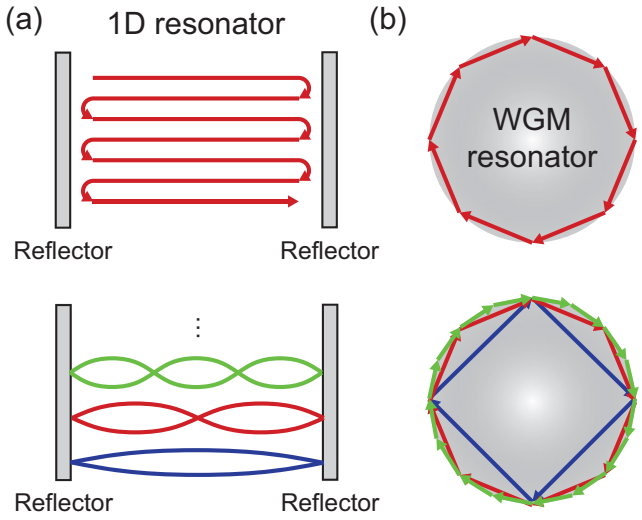

Figure 2.1: (a) Waves travel inside the resonator in the simple 1D resonator having two reflectors. The traveling waves are reflected back from the mirrors to form standing wave patterns. These standing waves are discretized by eigenvalues which can be interpreted to wavelengths or frequencies. (b) Similarly, traveling waves can be confined within whispering gallery mode resonators through total internal reflection. The waves are traveling along the perimeter owing to the closed domain under the periodic boundary condition.

WGM resonator confining "microwave" fields were first reported by Richtmyer in 1936 [32] and have been developed for engineering applications. In 1989, Braginsky et al. first demonstrated the "optical" WGM resonators with the quality factor of $\sim 10^8$ [33]. These ultra high-Q optical WGM resonators have been utilized from the initial proposal of quantum optics applications [34] to stabilizing optical sources, optical filters, optoelectronic oscillators, frequency combs [35, 36], atomic clocks [37], and sensor applications [38]. The WGMs can be supported by any circular optical resonator [39], but here I only focus on spherical resonators.

As a general analytic solution for WGMs in spherical resonators does not exist, it has to be examined by numerical or experimental methods [40, 41]. Luckily, one could obtain the analytic solution under axial symmetry with a refractive index which only depends on radial direction. The Helmholtz equation – derived from Maxwell's equation – can describe electric fields in spherical resonators [39, 42].

$$\nabla^2 E + k^2 n^2(r) E = 0. \tag{2.1}$$

Let us assume the refractive index is $n(r < a) = n$ and $n(r > a) = 1$, where

a is the radius of the cavity. With the separation of variables, one can divide the electric field $E(r, \theta, \phi)$ into radial $U(r)$ and angular components i.e., vectorial spherical harmonics $\boldsymbol{Y}_{lm}$ [39, 42]. Here l is the order of spherical harmonics and m is the azimuthal number which can vary from $-l$ to l. Consequently, the radial component inside of the dielectric is $U(r) = \psi_l(nkr)$, while the component outside of the dielectric is $U(r) = A\psi_l(kr) + B\chi_l(kr)$.[3] This radial function, which is a solution of Ricatti-Bessel radial equation [43], must satisfy the continuous conditions on the boundary for TE modes (See the detailed explanation in Appendix A).

$$n\frac{\psi_l'(nka)}{\psi_l(nka)} = \frac{\chi_l'(nka)}{\chi_l(nka)}. \tag{2.2}$$

Unfortunately, this transcendental equation Eq. (2.2) cannot be solved directly,

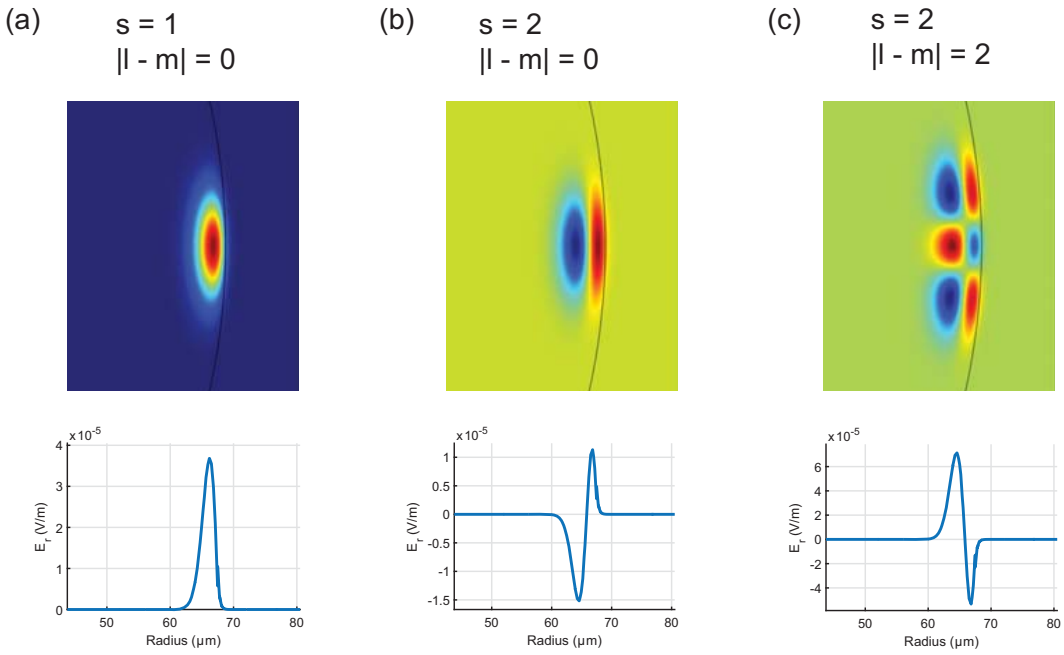

Figure 2.2: Radial components distributed in (r, θ) plane and cross-sectioned in the radial direction for (a) fundamental TE mode, (b) TE mode at ($s = 2$, and $p = 0$), and (c) TE mode at ($s = 2$, and $p = 2$) by FEM simulation.

therefore one must estimate its solution through an asymptotic series [44]. With consideration of the radial components and its corresponding vectorial spherical

[3]Here, $\psi_l(x) = xj_l(x)$ and $\chi_l(x) = xy_l(x)$ are functions of spherical Bessel and Neumann functions, $j_l(x)$ and $y_l(x)$.

harmonics, families of modes eventually come from the solution of Eq. (2.2). These families are identified by three modal indices (s, l, m), where s is the radial number which indicates an order of radial functions. For simplicity, I define the angular mode number $p = |l - m|$ that represents the order of polar-angled field distribution as illustrated in Fig. 2.2.[4]

Here, let us investigate the fundamental properties of WGM resonators. As light is confined with traveling along a circumference of the resonators in microscale, that is $\lambda \ll a$, the cavity has many modes separated by free spectral ranges (FSRs). Assuming the cavity is a perfect sphere, we provide the resonant frequencies of WGMs, characterized by the three modal indices $\omega_{s,l,p}$ as follows [45]:

$$\omega_{s,l,p} = \frac{c}{2\pi n a}\left[l + \alpha_s\left(\frac{l}{2}\right)^{1/3} - \frac{\chi n}{\sqrt{n^2-1}}\frac{1}{2} + \frac{3\alpha_s^2}{20}\left(\frac{l}{2}\right)^{-1/3} + O(l^{-2/3})\right], \quad (2.3)$$

where α_s is the s-th root of the Airy function, and $\chi = 1$ for quasi-TE and $\chi = 1/n^2$ for quasi-TM modes. To evaluate the FSRs, we must understand the spacings depend on three independent parameters (s, l, p). In spheroidal resonators, only the radial index s and the order of spherical harmonics l are major variables to determine the FSRs. As illustrated in Fig. 2.3.(a), the FSRs (or spacings) are different within distinguishable mode families characterized by (s, l) [46].

The intensity spectrum of WGMs, $I(\omega)$ show the Lorentzian function defined by:

$$I(\omega) = I_o \frac{(\kappa/2)^2}{(\omega - \omega_o)^2 + (\kappa/2)^2}, \quad (2.4)$$

where I_o is the intensity at resonance, κ is its full-width at half maximum (FWHM) and ω_o is the resonant frequency. Note that κ denotes the loss rate of the WGM. Figure 2.3.(b) illustrates one of mode spectra showing a Lorentzian line-shape described in Eq. (2.4).

The linewidth of the Lorentzian κ is unambiguously related to the Q-factor of

[4]Though Figure 2.2 shows numerical results through FEM simulation, it illustrates how the three indices (s, l, p) play a role in modal shapes. The analytic solution is presented in Appendix A.

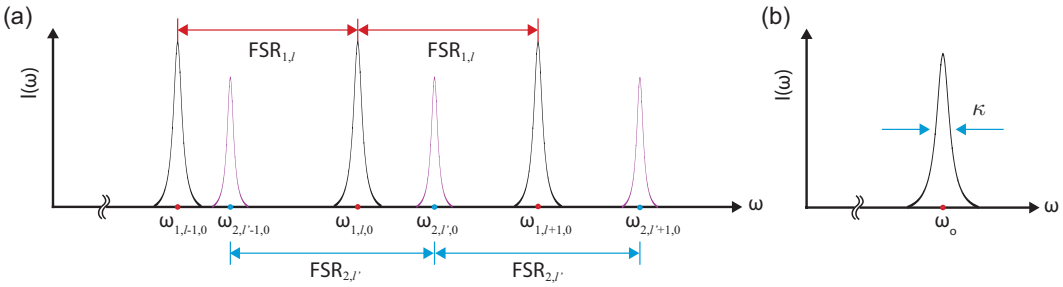

Figure 2.3: (a) Schematic of $\mathrm{FSR}_{s,l}$ in spherical resonators. In this specific example, the FSRs are evaluated with different l at fixed the radial mode number s. Each FSR is not identical, as distinguished by s and l in Eq. (2.3). (b) The spectrum at the resonance frequency ω_o has its linewidth κ .

WGM given by:[5]

$$Q = 2\pi \frac{\text{Stored energy}}{\text{Dissipated energy per cycle}} = \frac{\omega_o}{\kappa}. \tag{2.5}$$

Optical WGM resonators can have the Q factor up to 10^{11} which is one of the highest values in any other optical platforms [30]. An understanding of the Q-factor is essential for investigating loss mechanisms in resonators. Here, Gorodetsky et al. have characterized the Q-factor of optical WGM resonators as follows [47]:

$$\frac{1}{Q_{\text{tot}}} = \frac{1}{Q_{\text{mat}}} + \frac{1}{Q_{\text{rad}}} + \frac{1}{Q_{\text{scat}}} + \frac{1}{Q_{\text{ext}}}, \tag{2.6}$$

where Q_{tot} is the total Q-factor, Q_{mat} is the intrinsic material loss-related Q factor, Q_{rad} is the radiative loss-related factor, Q_{scat} is the scattering loss-related factor, and $Q_{\text{ext}}$is the external coupling related factor. Further discussion on loss mechanisms in optical WGM resonators is described in the next section.

It is of interest to develop equations for electromagnetic fields inside optical cavities, therefore it enables investigation on coupling to other modes and external sources. Considering the Maxwell equation, one can examine intracavity electric fields by using the method of separation of variables to find the temporal variation of the field amplitude.

$$\boldsymbol{E}(\boldsymbol{r}, t) = \sum_i \boldsymbol{\phi}_i(\boldsymbol{r}) \mathcal{E}_i(t) e^{-i\omega t} + c.c, \tag{2.7}$$

[5] A detailed derivation of the optical Q-factor is presented in Appendix C.

where $\boldsymbol{\phi}_i(\boldsymbol{r})$ is the vectorial spatial mode function, and $\mathcal{E}_i(t)$ is the temporal variation of amplitude [48]. By the slowly varying amplitude approximation, i.e. $\frac{\partial^2 \mathcal{E}}{\partial t^2} \ll \left|2i\omega\frac{\partial \mathcal{E}}{\partial t}\right|$, the equation of motion for $\mathcal{E}$ is written by the coupled-theory formula with the input-output theory [49, 50, 51].

$$\frac{da_i(t)}{dt} = -\left(\frac{\kappa}{2} + i\omega_o\right) a_i + \sqrt{\kappa_{\text{ex}}} a_{\text{in}}^i e^{-i\omega_{\text{in}} t}, \tag{2.8}$$

where κ_{ex} is the external coupling rate due to resonator-waveguide coupling, a_{in}^i is the input signal from a source through couplers, and ω_o and ω_{in} are the resonant frequency of a_i and the laser frequency, respectively. Here a_i is the dimensionless amplitude defined by $2\pi\frac{\hbar\omega_o}{\epsilon}|a_i|^2 = |\mathcal{E}|^2$, and a_{in}^i is the normalized input field from $\hbar\omega_{\text{in}}\langle(a_{\text{in}}^i)^* a_{\text{in}}\rangle = P$, where P is the input power driven into the mode a_i [51]. The linewidth, which is the total optical loss rate, is comprised of the intrinsic loss κ_i and the external coupling rate κ_{ex}, i.e. $\kappa = \kappa_i + \kappa_{\text{ex}}$. The following section will look into further discussion on the coupling to the resonators from external couplers.

2.2 Light coupling to WGM resonators

A fundamental understanding of the coupled mode theory is a key for studying light coupling to WGMs. Figure 2.4(a) shows that two modes a_1 and a_2 reside in individual waveguiding systems, and are overlapped outside the waveguides. These two blue curves shown in Fig. 2.4(a) are the spatial mode functions which we discussed in the last section, distributed in (x, y) space. At the same time, a_1 and a_2 modes are propagating in the z-direction guided by the two waveguides. Note that electromagnetic fields in dielectric waveguides are generally confined inside the dielectric, but the evanescent fields can be distributed outside the dielectric. In planar waveguides, the evanescent field is given by $\phi_z(x, y) \propto \exp(-\gamma_m y)$, where $\phi_z(x, y)$ is the z-component of eigenfunctions of a electromagnetic field and γ_m is the extinction coefficient, which indicates how the effective penetration length leaks outside dielectrics.[6] Hence, these two modes can be coupled evanescently outside the dielectric if a distance between the two waveguides is small. Mathematically, this coupling can be described as overlapping the spatial mode functions. Let's con-

[6]The extinction coefficient γ_m decreases with increasing the order of modes in the dielectric, therefore higher order modes tend to penetrate and reside outside. For more detailed information, please refer to the discussion in [30]

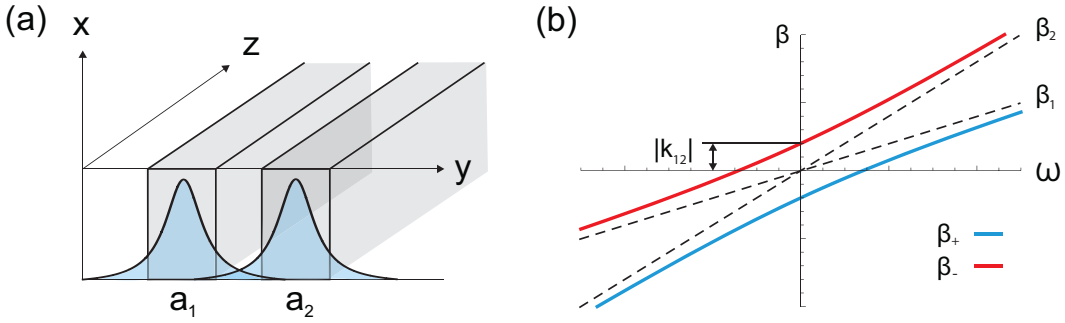

Figure 2.4: (a) EM fields guided in the two waveguides are coupled, as evanescent fields leaking from the dielectric pass through another dielectric. As long as the penetrated fields are overlapped with each other, these two fields are coupling along the z-direction. (b) Anti-crossing in the dispersion relation on β-ω space for the copropagating waves. Dotted lines indicate the original dispersions without the coupling $|k_{12}|$, which are crossed at the origin, yet these dispersions cannot be crossed, owing to the coupling.

sider the modes propagate in the z-direction, and they are coupled through the small overlap of each evanescent fields. These systems can be explained by the coupled mode theory.[7]

$$\begin{aligned} \frac{da_1}{dz} &= i\beta_1 a_1 + k_{12} a_2, \\ \frac{da_2}{dz} &= i\beta_2 a_2 + k_{21} a_1, \end{aligned} \tag{2.9}$$

where β_1 and β_2 are the propagation constants of guided electromagnetic fields a_1 and a_2, respectively, and k_{12} and k_{21} are the coupling constants. In the case where these two modes propagate in the same direction, the coupling constants become $k_{21} = -k_{12}^*$ via the energy conservation [49]. Considering the codirectional case, one can obtain propagation constants of two normal modes by the eigenvalue analysis as follows.

$$\begin{aligned} \beta_\pm &= \frac{\beta_1 + \beta_2}{2} \pm \sqrt{\left(\frac{\beta_1 - \beta_2}{2}\right)^2 + |k_{12}|^2} \\ &= \frac{\beta_1 + \beta_2}{2} \pm \beta_o. \end{aligned} \tag{2.10}$$

If the phase-matching condition is satisfied ($\beta_1 = \beta_2$), the mode split frequency β_o becomes the coupling constant $|k_{12}|$. If the phase-matching condition is not

[7] The loss rates and any higher order effects are not considered in Eq. (2.9).

satisfied ($\beta_1 \neq \beta_2$), the frequencies of normal modes $\beta_\pm$ split unevenly. Figure 2.4(b) illustrates the anti-crossing of two modes separated by $2|k_{12}|$ in dispersion relations based on Eq. (2.10). Equation (2.10) describes the propagation constants must be real values in any coupling rate, thereby it enables exchanging energy of these two modes in the Rabi oscillation form. To observe the dynamics of these two modes a_1 and a_2, one can simply solve Eq. (2.10) by using the diagonalization method [49].

$$
\begin{aligned}
a_1(z) &= \left[a_1(0)\left(\cos(\beta_o z) - i\frac{\beta_2-\beta_1}{2\beta_o}\sin(\beta_o z)\right) + \frac{k_{12}}{\beta_o}a_2(0)\sin(\beta_o z)\right] e^{i(\beta_1+\beta_2)/2}, \\
a_2(z) &= \left[-\frac{k_{12}^*}{\beta_o}a_2(0)\sin(\beta_o z) + a_1(0)\left(\cos(\beta_o z) - i\frac{\beta_1-\beta_2}{2\beta_o}\sin(\beta_o z)\right)\right] e^{i(\beta_1+\beta_2)/2}.
\end{aligned}
\tag{2.11}
$$

Here, $a_1(0)$ and $a_2(0)$ are the amplitudes of two modes at the initial position $z = 0$. To understand the energy exchange of a_1 and a_2, normalized powers are first defined as $P_1 = |a_1|^2$ and $P_2 = |a_2|^2$. Suppose that only a_1 is driven at $z = 0$, while a_2 is free at the initial, i.e., $a_1(0) = 1$ and $a_2(0) = 0$. For the phase-matching case ($\beta_1 = \beta_2$), the power of these two modes represented in Fig. 2.5(a) shows the Rabi-like oscillation, which indicates the energy is entirely transferred from a mode to another along the propagation direction, z. On the other hand, for the phase-mismatching case ($\beta_1 \neq \beta_2$), two modes partially exchange their energies to each other as illustrated in Fig. 2.5(b).

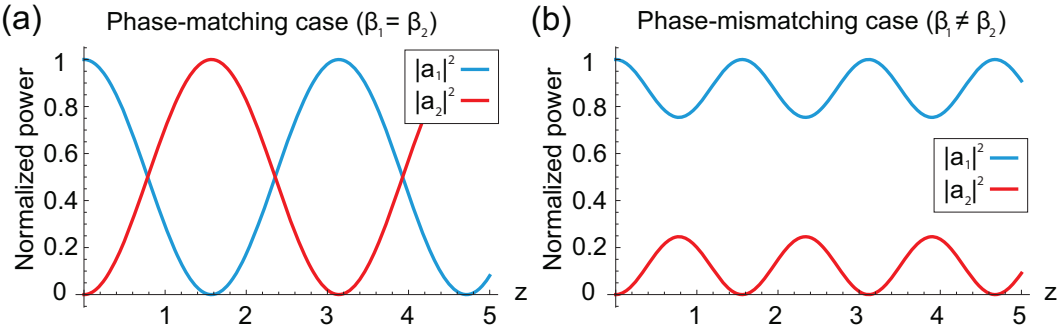

Figure 2.5: (a) For the phase-matching case ($\beta_1 = \beta_2 = 0.5$), energies between two modes are entirely exchanged with oscillating in the z-direction. (b) Meanwhile, energy transfer between two modes is inefficient for the phase-mismatching case ($\beta_1 = 4$ and $\beta_2 = 0.5$).

Left-side of Fig. 2.6 illustrates the schematic of a resonator-waveguide coupled system. Zooming in the interaction region, one can readily find that light from

the waveguide is transferred into the loaded side, the resonator through evanescent coupling.

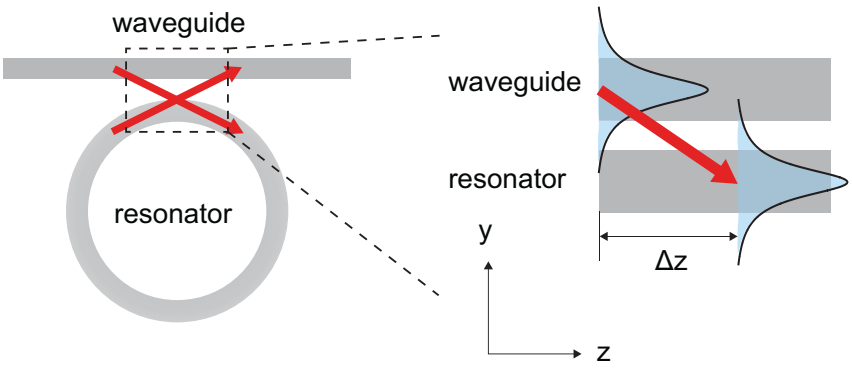

Figure 2.6: Schematic of a resonator-waveguide coupled system. Light driven through the waveguide is coupled to the resonator when the evanescent field from the waveguide can be absorbed into the resonator. Here I assume that the system satisfies the phase-matching condition.

So far, we have assumed that the external coupling κ_{ex} is large that we can observe proper energy transfer in the coupled system. Now let us consider the coupling κ_{ex} represented in Eq. (2.8) quantitatively. Suppose that the z-component of EM fields in the waveguide and in the resonator are expressed by $E_z^{\mathrm{wg}}(\boldsymbol{r},t) = \phi_z^{\mathrm{wg}}(x,y)\exp(-i(\omega_{\mathrm{wg}}t - \beta_{\mathrm{wg}}z))$ and $E_z^{\mathrm{res}}(\boldsymbol{r},t) = \phi_z^{\mathrm{res}}(x,y)\exp(-i(\omega_{\mathrm{wg}}t - \beta_{\mathrm{wg}}z))$, respectively.[8] The external coupling κ_{ex} can be thus given by [52]:

$$\kappa_{\mathrm{ex}} \propto \left| \int_{\mathcal{C}} d\Omega \exp(i(\beta_{\mathrm{wg}} - \beta_{\mathrm{res}})z)\phi_z^{\mathrm{wg}}(x,y)\phi_z^{\mathrm{res}}(x,y) \right|^2, \tag{2.12}$$

where $\phi_z^{\mathrm{wg}}(x,y)$ and $\phi_z^{\mathrm{res}}(x,y)$ are the spatial mode functions in the waveguide and resonator, and β_{wg} and β_{res} are the propagation constants for EM fields in the waveguide and resonator. Here the integration over a solid angle Ω in Eq. (2.12) can be done within the cross-section of the waveguide denoted by the subscript $\mathcal{C}$. In the case of the phase-matching ($\beta_{\mathrm{res}} = \beta_{\mathrm{wg}}$), the external coupling is entirely dependent on an overlap of two modes in the waveguide and resonator. This overlap of each evanescent field is subsequently associated with the distance of the waveguide to the resonator, as evanescent fields outside systems are distributed in the transverse directions of the systems.

[8] Assume that the relative phase difference is zero for the simplicity.

To obtain proper evanescent coupling in resonator-waveguide systems, one must consider required operational characteristics of couplers based on 1) phase-matching, 2) optimal overlap integral, 3) selectivity and 4) criticality [42]. Many distinct approaches of evanescent couplers in resonator-waveguide coupled systems have been demonstrated: prism couplers [11] (up to$\sim$ 90% coupling efficiency), polished optical fiber couplers [53](limited efficiency due to phase-mismatch), and tapered fiber couplers [54](∼100% efficiency achievable). In this thesis, we will use single-mode

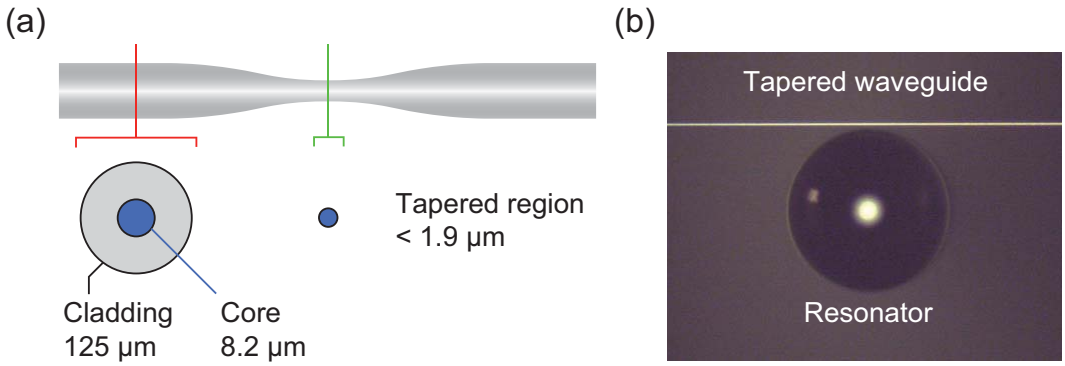

Figure 2.7: (a) The typical single mode fiber (SMF) with tapered region; the SMF has core and cladding, while the tapered region consists of only core with less than 1.9 μm diameter. (b) Image of the tapered waveguide and resonator coupled system. The taper is fabricated from the SMF-28 manufactured by Corning, the fused silica resonator from the residue of a taper.

tapered fibers to couple light into resonators due to high coupling efficiency. The tapered fiber fabricated by pulling SMF-28 under a hydrogen torch represents a single-mode waveguide which is comprised of a silica core as shown in Fig. 2.7(a). From the formula for achieving a single-mode in fibers $d_c = 2.405\lambda/\pi\sqrt{n_{\text{core}}^2 - n_{\text{clad}}^2}$, the critical diameter d_c can be determined 1.9 μm in 1550 nm for allowing only a HE_{11} mode. Here, n_{core} and n_{clad} are the refractive index of a core and cladding, respectively, λ is the wavelength of light, and 2.405 is a first zero of first kind of Bessel function $J_0(x = 2.405) = 0$. Figure 2.6(b) illustrates that light is driven into a fused silica microsphere resonator through the tapered fiber.

Adjusting the relative position of a taper or resonator, one can achieve almost perfect coupling, i.e., critical coupling of a taper to a resonator. Cai et al. demonstrated how the coupling rate is affected by a distance of a tapered waveguide to a resonator [54] (See Fig. 2.8(a)). Now let us look into the mathematical formal-

ism for resonator-waveguide coupled systems. The spectrum of transmission inside waveguides coupled to resonators is represented as follows:

$$\frac{da(t)}{dt} = -\left(\frac{\kappa_i + \kappa_{\text{ex}}}{2} + i\Delta\right) a + \sqrt{\kappa_{\text{ex}}} a_{\text{in}}, \tag{2.13a}$$

$$a_{\text{out}} = a_{\text{in}} - \sqrt{\kappa_{\text{ex}}} a, \tag{2.13b}$$

$$T = \frac{a_{\text{out}}}{a_{\text{in}}} = \frac{\kappa_i - \kappa_{\text{ex}} + i2\Delta}{\kappa_i + \kappa_{\text{ex}} + i2\Delta}. \tag{2.13c}$$

The equation of motion for the mode in a resonator from Eq. (2.8) is rewritten by rotating a frame with the laser frequency[9] as described in Eq. (2.13a). Here $\Delta = \omega_o - \omega_{\text{in}}$ is the detuning. The output signal a_{out} is determined by using the input-output formalism in Eq. (2.13b), therefore it enables calculating the transmission T as described in Eq. (2.13c). Figure 2.8(b) shows the transmission spectrum with evolving the external coupling κ_{ex}. A relatively narrow dip in the transmission is

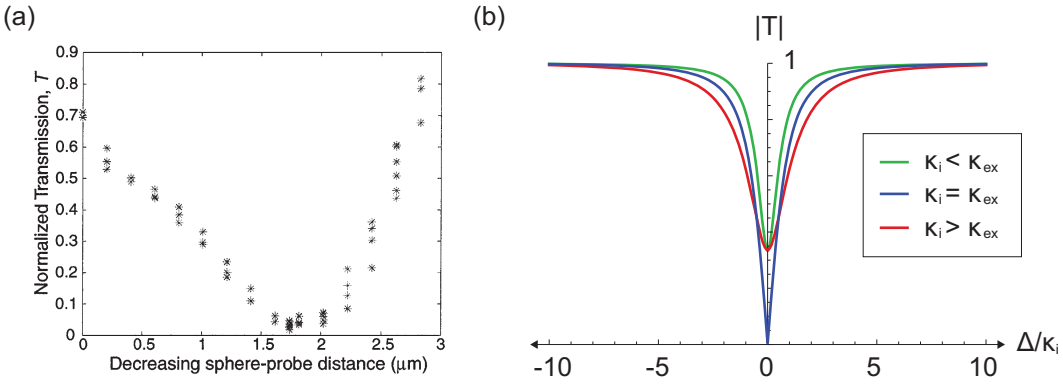

Figure 2.8: (a) Normalized transmission as a function of the probe position for a near fundamental WGM in a 150 μm microsphere (Reproduced from [54]). (b) Calculated transmission as a function of the external coupling κ_{ex}: 1) The under-coupled case in $\kappa_i < \kappa_{\text{ex}}$, 2) The critical coupled case in $\kappa_i = \kappa_{\text{ex}}$ 3) The over-coupled case in $\kappa_i > \kappa_{\text{ex}}$

shown in the under-coupled case $\kappa_i < \kappa_{\text{ex}}$, while a broader dip illustrated in the over-coupled one $\kappa_i > \kappa_{\text{ex}}$. When the external coupling is same to the intrinsic loss $\kappa_i = \kappa_{\text{ex}}$, which refers to the critical coupling, one should observe 100% coupling efficiency on resonance in resonator-waveguide coupled systems (See Fig. 2.8(b)).

[9]The reference frame can be shifted as $a \rightarrow ae^{-i\omega_{\text{in}}t}$.

2.3 Theory of Brillouin Optomechanics

2.3.1 Review of Brillouin scattering

Molecular scatterings of light – mainly photon-phonon interaction – have been intensively studied since the early 20th century. Such scatterings can take place under permittivity perturbed by thermal elastic waves (isobaric) or pressure driven acoustic waves (isothermal).[10] One of these scatterings caused by the isothermal process is called Brillouin scattering, which is scattering from acoustic phonons in a microscopic aspect [55, 56]. This Brillouin scattering is one of the strongest $\chi^{(3)}$ processes; it is orders of magnitude higher than optical Kerr effect and Raman scattering [56, 57]. Thus, Brillouin scattering, which is generally known as an undesirable effect, inhibits photon transport in waveguiding systems, e.g., a parasitic loss in optical fibers to prevent communications [1, 58, 59]. However, Brillouin scattering has been employed in a wide range of applications recently [60] in ultra-narrow linewidth lasers [61, 62, 63, 21, 64], optical sensors [65], optical isolators [22, 18, 19, 23], slow-fast light [66, 67], optical cooling [68], and light storage [69, 70].

Brillouin first reported this spontaneous scattering in 1922 [71], however, it is believed that Mandelstam first suggested scattering from thermal phonons in 1918 but published later in 1926 [72]. 40 years later, the first demonstration of stimulated Brillouin scattering (SBS) process was shown by Chiao, Townes, and Stoicheff [73]. In principle, scattered light by thermally excited phonons induces electrostriction and radiation forces through the interference of scattered and incident light. Simultaneously, these forces excite density waves which can change its refractive index and cause diffraction via a photoelastic effect, as the acoustic waves are much slower than incident light waves. This SBS is generally orders of magnitude stronger than a spontaneous process [56]. Previously, only backward Brillouin scattering was achievable due to the phase matching condition in bulk medium [56] until Shelby demonstrated forward Brillouin scattering in optical fibers in 1985 [74, 75]. Instead of bulk acoustic waves, guided acoustic modes can be employed to satisfy the phase matching condition for the forward scattering (Fig. 2.9).[11] In Figure 2.9, k and ω

[10] The permittivity is susceptible to temperature and pressure.

$$d\epsilon \simeq \left(\frac{\partial \epsilon}{\partial S}\right)_P dS + \left(\frac{\partial \epsilon}{\partial P}\right)_S dP,$$

where S is the entropy and P is the pressure.

[11] Schwab and Roukes clearly state the distinction between the (bulk) phonons and guided acoustic

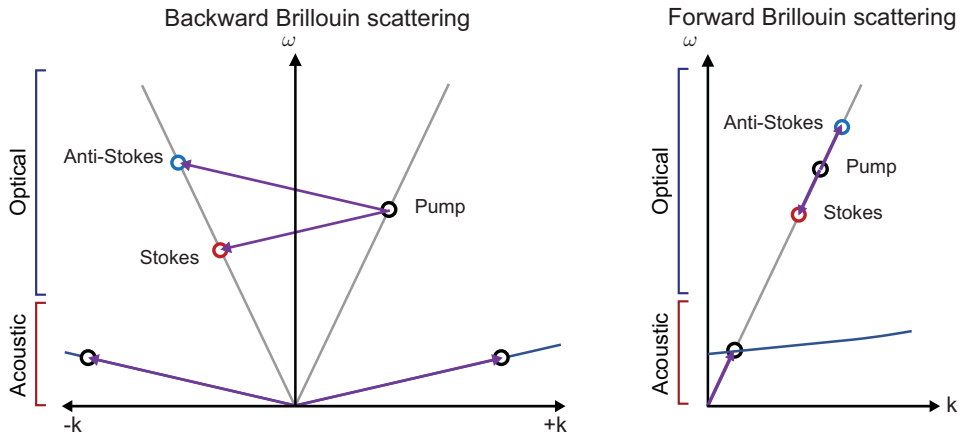

Figure 2.9: The $\omega - k$ diagram for backward and forward Brillouin scattering in order to show the phase matching condition. Backward scattering (left) is associated with the bulk phonons whose dispersion in the $\omega - k$ diagram is determined by the lattice model. On the other hand, forward scattering (right) can be achievable by the guided acoustic modes whose frequency and momentum are smaller.

indicate momentum in a traveling direction and its frequency, respectively.

Figure 2.10 shows forward SBS demonstrated by different mechanisms in multiple platforms. As illustrated in Fig. 2.10(a), the forward SBS achieved by intramodal transition has been reported in photonic crystal fibers [77] and nanoscale waveguides [78].[12] Note that such intramodal scattering enables generation of multiple sidebands as shown in 2.10(a). On the other hand, the forward SBS by intermodal transition has been shown by various groups [21, 80, 81]. Compared to the intramodal transition, forward SBS by intermodal transition can only generate single sideband due to the phase matching condition illustrated in Fig. 2.10(b) [80, 81]. The intermodal Brillouin scattering can also be realized in whispering gallery mode (WGM) resonators as shown in Fig. 2.10 (c). As these traveling acoustic waves are confined onto a perimeter of resonators due to acoustic total internal reflection, the linear acoustic dispersion makes it possible to satisfy the phase matching condition [21]. As selecting a pump and anti-Stokes optical mode pair via this intermodal transition, Bahl et al. first reported spontaneous Brillouin cooling in silica spherical

modes [76]. The phonons tend to have higher frequency and wavenumber, while the guided modes do have smaller frequency and wavenumber which are determined by the geometry at nano/micro scale. Instead, the bulk phonons are distributed within broad frequency range governed by the Bose-Einstein distribution.

[12] Rakich et al. first reported that boundary forces due to radiation pressure and electrostriction force boost SBS gain significantly in the subwavelength limit [79].

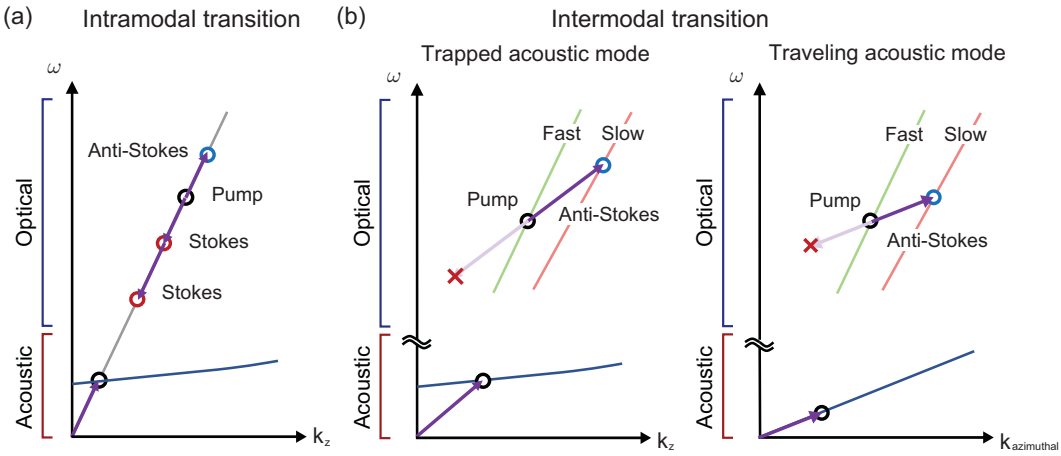

Figure 2.10: (a) Forward intramodal Brillouin scatterings give multiple cascaded Stokes and anti-Stokes sidebands with the guided acoustic modes. (b-c) Forward Brillouin scatterings via intermodal transition happen with trapped acoustic modes and traveling acoustic modes, respectively. These intermodal scatterings only provide single Stokes (or anti-Stokes) scattering. The trapped acoustic modes, having a low group velocity, is available in photonic crystal fibers or waveguides, while the traveling acoustic modes, having a rather high group velocity, is observed in WGM resonators. Here, k_z is the wavevector in the propagating direction, and $k_{\text{azimuthal}}$ is the azimuthal wavevector in the WGM resonators.

resonators [68]. Subsequently, many attempts have been made with the purpose of realizing Brillouin cooling in various platforms [26, 82]. In this thesis, silica microsphere resonators are utilized as illustrated in Fig. 2.11(a). The next section presents a further rigorous analysis.

2.3.2 Theoretical model

An understanding of SBS enhanced by boundary forces is essential to obtain Brillouin optomechanical interaction at the micro/nanoscale. SBS is caused by bulk electrostriction which results from pump and scattered light, while it is also affected by boundary forces in the subwavelength limit. The boundary forces are dominantly induced by the coherent interaction of radiation pressure and an electrostrictive force at boundaries in the nanoscale waveguides [79]. In a similar manner, SBS gain is also enhanced by such boundary forces in WGM resonators [83]. In WGM resonators, the optical pressure exciting mechanical modes are $F_i = F_i^{\text{E.S, body}} + F_i^{\text{E.S, boundary}} + F_i^{\text{RP}}$, where $F_i^{\text{E.S, body}}$ and $F_i^{\text{E.S, boundary}}$ are the body and boundary components of the

electrostrictive forces, and F_i^{RP} is the radiation pressure.[13] To understand these pressures, the Maxwell stress tensor should be explained first.[14]

$$\sigma_{ij} = -\frac{1}{2}\epsilon_o n^4 p_{klij} E_k^{\mathrm{p}} E_l^{\mathrm{s}},$$

where n is the refractive index and p_{klij} is the photoelastic tensor. As described, σ_{ij} results from the electrostriction force caused by the pump and scattered fields E_k^{p} and E_l^{s}. Now one obtains that every pressure acting on the mechanical modes is given by[15]:

$$F_i^{\text{E.S, body}} = \int dz \frac{\partial \sigma_{ij}}{\partial x_j} \tag{2.14a}$$

$$F_i^{\text{E.S, boundary}} = \sigma_{ij}\hat{n}_j \tag{2.14b}$$

$$F_i^{\mathrm{RP}} = \frac{\epsilon_o \epsilon}{2}(\epsilon - 1) E_j^{\mathrm{p}} E_j^{\mathrm{s}} \hat{n}_i \tag{2.14c}$$

where $\hat{n}_i$ is the boundary surface normal vector. Here, the electrostriction force density is integrated over the traveling direction z in Eq. (2.14a). Note that the pump and scattered fields must be aligned to obtain nonzero radiation pressure.

Figure 2.11(a) illustrates acting forces for achieving the forward SBS in silica microspherical WGM resonators. The electrostriction and radiation pressure on the boundary are not negligible along the modal volume; therefore they increase the SBS gain in the resonators. Both the SBS gains for the intramodal scattering (TE00/TE00) and intermodal scattering (TE00/TE01) are approximately ten times more than the SBS gain induced by the bulk electrostriction[16] as shown in Fig. 2.11(b).

The phenomenological expression can readily provide the equations of motion for each of the fields. The quantum mechanical formalism enables quantization of

[13] These expressions are written in tensor notation.

[14] Assume that the medium is isotropic.

[15] Suppose that the system is surrounded by air, thus equations (2.14) focus on the Maxwell stress tensor inside the system only.

[16] Here, the bulk electrostriction actuates a longitudinal traveling acoustic wave. Suppose that transverse optical fields act on the acoustic wave so that the photoelastic tensor p_{klij} can be simplified to p_{12}. Such a scalar SBS gain is thus given by $G_B = \frac{M}{m_s}\frac{n^7 p_{12}^2 \omega_s^2}{2c^3 \rho V_L}\frac{Q}{\omega_m}\eta$, where M and m_s are the mechanical and scattered modes m numbers, ρ is the density, V_L is the longitudinal sound velocity, Q is the mechanical Q factor, and ω_m is the mechanical resonant frequency. Here, η is the overlap integral of the optical and mechanical fields [83].

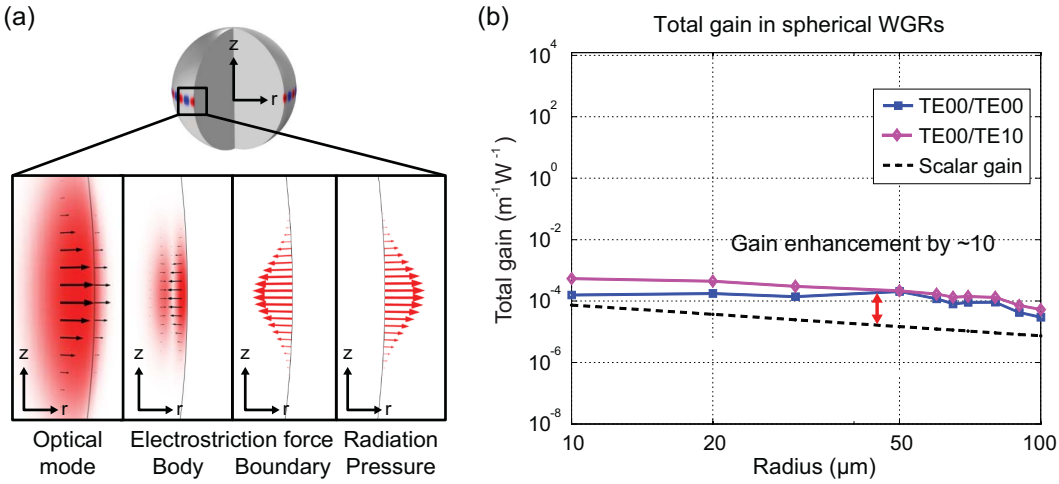

Figure 2.11: (Adapted from [83]) (a) Illustration of forces and WGM in the microsphere resonator. The optical mode simulation represents the radial component of EM field. In addition the bulk electrostriction force happens inside the resonator, while the boundary force acts on the surface. The radiation pressure is also seen on the boundary. (b) The SBS gain in intra- and intermodal transition can be increased by 10 times, as the boundary electrostriction forces and radiation pressures contribute this gain constructively. Note that (quasi) TE modes are defined in the axial direction, z.

the electric field $\boldsymbol{E}$ and acoustic field $\boldsymbol{u}$ in cylindrical coordinates as follows:

$$\boldsymbol{E}(\boldsymbol{r},t) = \sum_i \sqrt{\frac{\hbar\omega}{2\epsilon_o}}\vec{\phi}_i(r,z)\hat{a}_i^\dagger e^{-i(\omega_i t + m_i\theta)} + \text{h.c} \tag{2.15a}$$

$$\boldsymbol{u}(\boldsymbol{r},t) = \sum_i \sqrt{\frac{\hbar}{2\omega_m}}\vec{\psi}_i(r,z)\hat{b}_i^\dagger e^{-i(\omega_{m,i} t + M_i\theta)} + \text{h.c}, \tag{2.15b}$$

where $\vec{\phi}_i(r,z)$ and $\vec{\psi}_i(r,z)$ are the vectorial mode shape functions for the optical and mechanical waves, and $\hat{a}_i^\dagger(\hat{a}_i)$ and $\hat{b}_i^\dagger(\hat{b}_i)$ are the creation (annihilation) operators for the optical and mechanical mode, respectively.[17] Here ω_i and $\omega_{m,i}$ are the optical and mechanical frequencies, and m_i and M_i are the azimuthal mode orders of the optical and mechanical waves.[18] Let us consider the system consists of two optical modes pair and mechanical modes, thereby its interaction Hamiltonian is given

[17] One should find quantum mechanical relations in Eq. (2.15) [84]:

$$[\hat{a}_i, \hat{a}_j^\dagger] = [\hat{b}_i, \hat{b}_j^\dagger] = \delta_{ij}.$$

Here, these modes are quantized by the quantum number i in momentum spaces

[18] Assume that waves travel in the radial direction, so these modes $\phi(r,\theta)$ and $\psi(r,\theta)$ are transverse.

by[19] [85]:

$$H_{i,j}^{\text{int}} = \int dV \frac{\Delta(\epsilon_{ij})}{2} \langle E_i^{\text{p}} E_j^{\text{s}} \rangle \simeq \int dV \frac{1}{2} \frac{\partial \epsilon_{ij}}{\partial S_{kl}} S_{kl} \langle E_i^{\text{p}} E_j^{\text{s}} \rangle, \tag{2.16}$$

where $\Delta(\epsilon_{ij})$ is the permittivity change due to the radiation pressure and electrostriction force, S_{kl} is the strain tensor, and $\langle \ldots \rangle$ is the ensemble average (or time average). The Hamiltonian matrix in Eq. (2.16) is not generally diagonalized, as acting force tensors are not isotropic as described in Eq. (2.14) . However, the major component $H_{2,2}^{\text{int}}$ is dominant, as copropagating the pump and Stokes (or anti-Stokes) is necessary to achieve the forward SBS in this case. Thus, this component is primarily considered in this thesis, which is now called H_{int}. As shown in Fig. 2.11(a), the radial components of the electrostriction and radiation pressure mainly act on driving traveling acoustic waves along the perimeter. Consequently, the strain is simplified as $S_{kl} \rightarrow S = \partial u_\theta / \partial r$, where u_θ is the polar component of the acoustic wave. Considering $\partial \epsilon / \partial S$ is a constant, the simplified Hamiltonian can be rewritten as:

$$\begin{aligned} H_{\text{int}} = \hbar \frac{1}{4\epsilon_o} \frac{\partial \epsilon}{\partial S} \int \sum_{i,j,k} \sqrt{\frac{\hbar \omega_i \omega_j}{2\omega_m}} \left(\phi_i^\theta \phi_j^\theta \frac{\partial \psi_k^\theta}{\partial r} \right) \\ \left[\hat{a}_i \hat{a}_j e^{i(m_i+m_j)\theta} + \hat{a}_i \hat{a}_j^\dagger e^{i(m_i-m_j)\theta} + \text{h.c} \right] \left[\hat{b}_k^\dagger e^{-iM_k\theta} + \text{h.c} \right] r dr d\theta dz, \end{aligned}$$

where ϕ_i^θ and ψ_i^θ are the polar components of the optical and mechanical mode functions. Here, the modes can be sorted out through the selection rules for Brillouin scattering, i.e. satisfying the phase-matching condition[20]. As a result, this Hamiltonian becomes:

$$H_{\text{int}} = \hbar g (\underbrace{\hat{a}_p^\dagger \hat{a}_s \hat{b}}_{\text{Stokes}} + \underbrace{\hat{a}_p \hat{a}_s^\dagger \hat{b}}_{\text{anti-Stokes}} + \text{h.c}), \tag{2.17}$$

where the subindices describe the pump and scattered modes. Here, g is the single photon Brillouin optomechanical coupling defined by $g \propto \int dr dz \left(\phi_p^\theta \phi_s^\theta \frac{\partial \psi^\theta}{\partial r} \right)$. Now,

[19] Here, the subindices of H_{ij}^{int} denotes $i = 1$ for the radial, $i = 2$ for the polar, and $i = 3$ for the axial component, respectively.

[20] The phase matching condition is $m_p - m_s = M$ for the forward Stokes Brillouin scattering, while $m_s - m_p = M$ for the forward anti-Stokes Brillouin scattering

the total Hamiltonian including unperturbed modal Hamiltonians is written by:

$$H = \hbar\omega_p \hat{a}_p^\dagger \hat{a}_p + \hbar\omega_s \hat{a}_s^\dagger \hat{a}_s + \hbar\omega_m \hat{b}^\dagger \hat{b} + \hbar g(\hat{a}_p^\dagger \hat{a}_s \hat{b} + \hat{a}_p \hat{a}_s^\dagger \hat{b} + \text{h.c}). \tag{2.18}$$

Consequently, one obtains the equations of motion for the optical and mechanical mode through the Heisenberg picture.[21] When the anti-Stokes Brillouin scattering only occurs in the intermodal transition, the equations become

$$\dot{\hat{a}}_p = -\left(\frac{\kappa_p}{2} + i\omega_p\right)\hat{a}_p - ig\hat{a}_s\hat{b}^\dagger + \sqrt{\kappa_i}\hat{a}_{\text{vac}}(t), \tag{2.19a}$$

$$\dot{\hat{a}}_s = -\left(\frac{\kappa_s}{2} + i\omega_s\right)\hat{a}_s - ig\hat{a}_p\hat{b} + \sqrt{\kappa_i}\hat{a}_{\text{vac}}(t), \tag{2.19b}$$

$$\dot{\hat{b}} = -\left(\frac{\Gamma}{2} + i\omega_m\right)\hat{b} - ig\hat{a}_p^\dagger\hat{a}_s + \sqrt{\Gamma}\hat{b}_{\text{th}}(t). \tag{2.19c}$$

Here, the $\hat{a}_{\text{vac}}(t)$ and $\hat{b}_{\text{th}}(t)$ are the optical vacuum noise[22] and thermal noise, i.e. Langevin noise. Equations (2.19) illustrate the dynamics of the triply-resonant coupled modes. Note that the loss rates added into these equations do not result from the Hamiltonian in Eq. (2.18) through the Heisenberg picture, but from the fluctuation-dissipation theorem described in the next section.

Unfortunately, these triply-resonant equations in Eq. (2.19) have nonlinear interaction terms, thereby they are not solvable analytically. In cases of pump or pump-probe experiments, the pump is generally orders of magnitude higher than these interactions and Langevin noise terms. The pump field $\hat{a}_p$ is thus a constant under the non-deplete approximation, i.e. $\hat{a}_p \to \bar{a}_p$.[23] Equations (2.19) are simplified to:

$$\dot{\hat{a}}_s = -\left(\frac{\kappa_s}{2} + i\omega_s\right)\hat{a}_s - iG\hat{b} + \sqrt{\kappa_i}\hat{a}_{\text{vac}}(t), \tag{2.20a}$$

$$\dot{\hat{b}} = -\left(\frac{\Gamma}{2} + i\omega_m\right)\hat{b} - iG^*\hat{a}_s + \sqrt{\Gamma}\hat{b}_{\text{th}}(t), \tag{2.20b}$$

where $G = g\bar{a}_p$ is the optomechanical coupling rate. The scattered and mechanical

[21] The dynamics of an observable can be extracted in the Heisenberg picture, $\frac{dA}{dt} = \frac{i}{\hbar}[H, A(t)]$.

[22] The vacuum noise is caused from the Heisenberg uncertainty which is a source of the Casimir effect. Note that the optical thermal noise is generally negligible, as the optical frequency is a bit high.

[23] When it comes to the upper boundary region, where the nonlinear interaction term in Eq. (2.19a) is comparable to the pump input, this interaction cannot be negligible. The nonlinear features - limit cycle and chaotic behaviors- are observed in the high pump power regime.

modes are coupled mediated via the pump so that equations (2.20) are treated as the simple two-mode coupled system [49]. Applying the Fourier transform to Eq. (2.20) enables analysis of the solutions readily. As a result, the response functions of the observables, $\hat{b}$ or $\hat{a}_s$ are acquired by using the linear response theory.[24]

$$\chi_a^{-1}(\omega) = \frac{\kappa_s}{2} + i(\omega_s - \omega) + \frac{G^2}{\frac{\Gamma}{2} + i(\omega_m - \omega)}, \tag{2.21a}$$

$$\chi_b^{-1}(\omega) = \frac{\Gamma}{2} + i(\omega_m - \omega) + \frac{G^2}{\frac{\kappa_s}{2} + i(\omega_s - \omega)}. \tag{2.21b}$$

Here $\chi_a^{-1}(\omega)$ and $\chi_b^{-1}(\omega)$ are the inverse spectrum of susceptibilities (or response functions) for the anti-Stokes and mechanical mode. The real parts of the susceptibilities give the effective loss rates of each mode, while the imaginary parts yield the effective resonant frequencies, which are related to the optical spring effect.

From Eq. (2.21), one may realize the optical mode a_s and the mechanical mode b are coupled through Brillouin optomechanical interaction as shown in Fig. 2.12(a). Figure 2.12(b) illustrates the evolving susceptibilities for the a_s and b modes with the increased optomechanical coupling G. Note that these two susceptibilities are normalized by using the maximum value of each susceptibility at zero optomechanical coupling (G = 0). These responses clearly show Brillouin optomechanical normal-mode splitting. Interestingly, the mechanical response becomes smaller with the increased coupling G, implying spontaneous Brillouin cooling (See the detailed explanation in Chapter 5).

2.3.3 Fluctuation-dissipation theorem for analyzing noise

An understanding of interacting with environment in quantum mechanical systems is important for analyzing the systems. Any fully quantized system associated with damping can be explained by the fluctuation–dissipation theorem. Let us consider

[24] If any observable $u(t)$ has a linear input-output relation, $\mathcal{L}u(t) = f(t)$, the response of $u(t)$ can be explained through the Green's function.

$$u(t) = \int_{-\infty}^{t} \chi(t-\tau) f(\tau) d\tau,$$

where $\chi(t-\tau)$ is the response function or the susceptibility. A spectral of the response function is $\chi(\omega) = \frac{\tilde{u}(\omega)}{\tilde{f}(\omega_s)}$ via the Fourier transform.

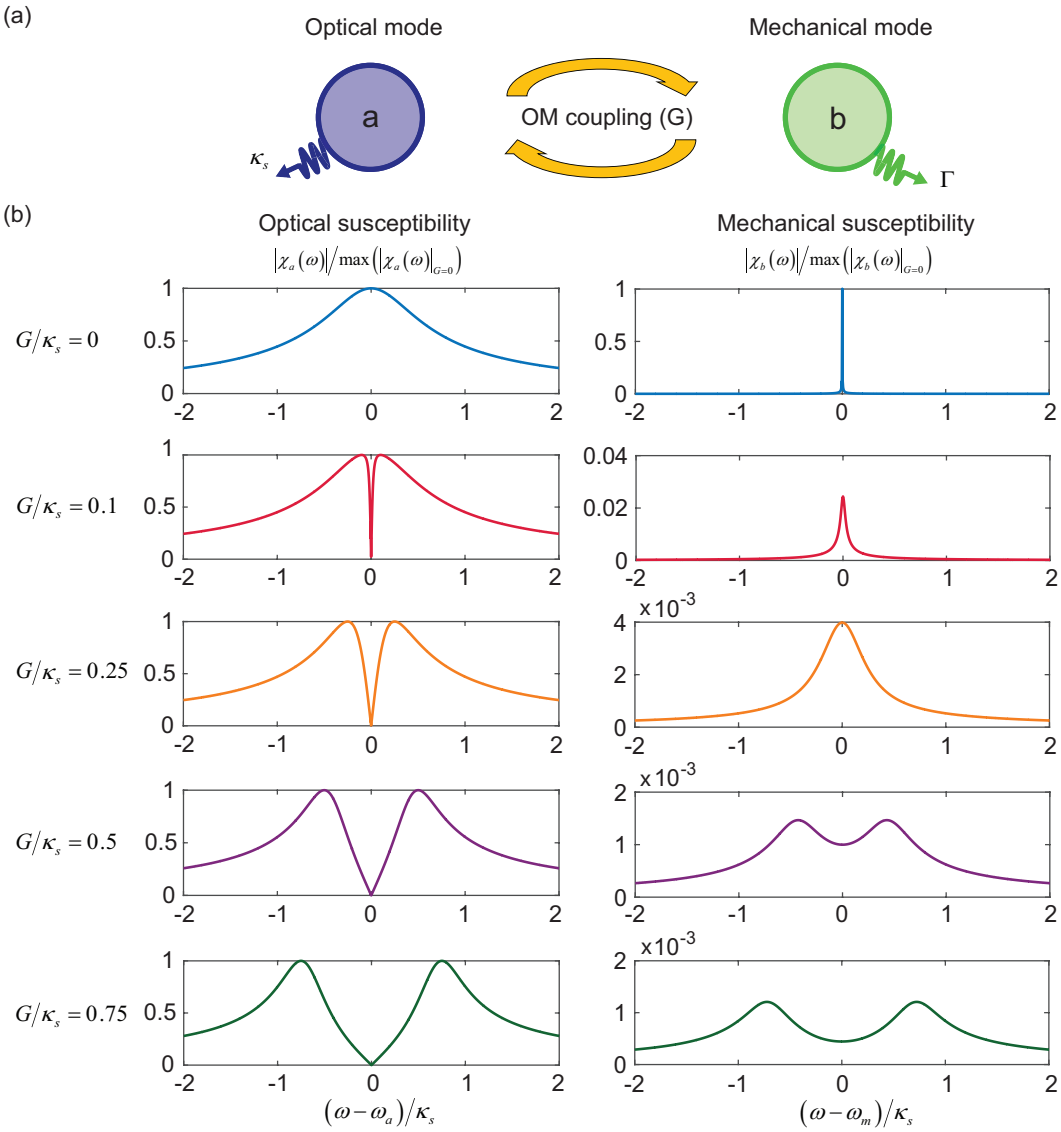

Figure 2.12: (a) Illustration of the two-mode coupling mediated by Brillouin optomechanical coupling (G). The optical and mechanical modes are coupled each other as well as coupled to the bath. (b) The evolving susceptibilities of the optical and mechanical modes with increased the optomechanical coupling. Here, these susceptibilities are normalized by each susceptibility at G = 0, and the x-axis is also normalized by the optical loss rate κ_s.

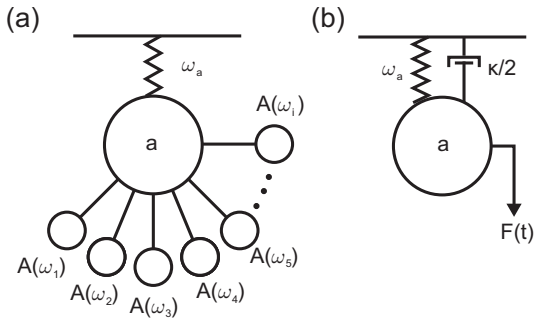

Figure 2.13: (Reproduced from [87]) (a) Illustration of system-bath interaction. The quantized bath modes $A(\omega_i)$ are coupled to the system whose resonance frequency is ω_a. (b) These bath couplings are simplified to the damping rate κ and Langevin force $F(t)$.

the Hamiltonian of a simple system with bath interaction.[25]

$$H = \hbar\omega_a \left(a^\dagger a + \frac{1}{2}\right) + \sum_\omega \hbar \left[A^\dagger(\omega)A(\omega) + \frac{1}{2}\right] + \sum_\omega \hbar \left[g(\omega)a^\dagger A(\omega) + h.c\right], \quad (2.22)$$

where a ($a^\dagger$) and $A(\omega)$ ($A^\dagger(\omega)$) is the annihilation (creation) operator for a system and bath oscillators, respectively, and $g(\omega)$ is the coupling coefficient of the system to the bath as shown in Fig 2.13(a). The Heisenberg-Langevin equation can provide the equation of motion for a (See the detailed derivation in [86, 87]).

$$\dot{a} = -i\omega_a a - \frac{\kappa}{2}a + F(t). \quad (2.23)$$

As illustrated in Fig. 2.13(b), $\kappa \equiv 2\pi\eta(\omega_a)|g(\omega_a)|^2$ is the loss rate and $F(t) \equiv -i\sum_\omega g(\omega)A(\omega,0)\exp(-i\omega t)$ is the Langevin force, where $\eta(\omega)$ is the density of states for the bath oscillator modes $A(\omega)$. Here the Langevin force $F(t)$ is a stochastic and ergodic[26] source excited by thermal and or quantum fluctuation. In the thesis, only thermal noises are considered, as our experiments have been performed at room temperature only.

[25] From this section, the hat notation for operators has been omitted.

[26] Note that an ergodic process is one of the sets of stationary processes. Here a stationary process does not change "statistically" properties over time, e.g. probability density functions, average, or so on. It is called ergodic if the random process, which is a function of a stationary random variable $g[X(t)]$, has the property where its time average is identical to the ensemble average:

$$\lim_{T\to\infty} \frac{1}{2T}\int_{-T}^{T} g[X(t)]dt = \langle g[X(t)]\rangle$$

.

For the purpose of convention, let us introduce the stochastic input $a_{\rm in}(t)$ represented in $F(t) = \sqrt{\kappa}a_{\rm in}(t)$, which corresponds to $\hbar\omega_a\langle a_{\rm in}^\dagger(t)a_{\rm in}(t)\rangle = P(t)$, where $P(t)$ is the input power. Equation (2.23) describes the noise $a_{\rm in}(t)$ is the source of the mode such that $a(t)$ must be also considered as an ergodic process. By the Wiener-Khlinchin theorem, the spectral density of $a(t)$ must be a Fourier pair of its auto-correlation function $\Gamma_a(\tau) = \langle a^*(t)a(t+\tau)\rangle = \langle a^*(t)a(t')\rangle$.

$$S_{aa}(\omega) \equiv \int_{-\infty}^{\infty} \Gamma_a(\tau)e^{i\omega\tau}d\tau \tag{2.24}$$

This spectral density $S_{aa}(\omega)$ can be easily obtained by given relations. Suppose the noise $a_{\rm in}$, which is considered as the bath oscillators, is a Markovian;

$$\langle a_{\rm in}^\dagger(t)a_{\rm in}(t')\rangle = N(\omega)\delta(t-t'), \tag{2.25a}$$

$$\langle a_{\rm in}(t)a_{\rm in}^\dagger(t')\rangle = [N(\omega)+1]\,,\delta(t-t') \tag{2.25b}$$

$$N(\omega) = \frac{1}{\exp(\hbar\omega/kT)-1}, \tag{2.25c}$$

Here, the autocorrelation function is the delta function, which means it is totally random process. Considering Eq. (2.23), one can thus obtain the spectral density.[27]

$$S_{aa}(\omega) = \frac{\kappa N(\omega_a)}{(\kappa/2)^2 + (\omega_a-\omega)^2} \tag{2.26}$$

Equation (2.26) can be applied to any system with consideration of bath interactions.

2.4 Loss mechanisms in optical systems

So far the spectrum of transmission has been studied by varying the coupling rate. The previous section describes that an external coupling from a waveguide is controlled by changing the gap of waveguide-resonator coupled systems. Here, we now discuss the intrinsic loss rates by considering Eq. (2.6), which can be rewritten in

[27]The spectral density $S_{aa}(\omega)$ of the optical field can be obtained by the relation [86]:

$$\langle \tilde{a}^\dagger(\omega)\tilde{a}(\omega')\rangle = 2\pi\delta(\omega-\omega')S_{aa}(\omega).$$

terms of the intrinsic loss rate:

$$\kappa_i = \kappa_{\mathrm{mat}} + \kappa_{\mathrm{rad}} + \kappa_{\mathrm{scat}} \tag{2.27}$$

where κ_{mat} is the material loss, κ_{rad}, is the radiative loss due to curvature, and κ_{scat} is the surface scattering loss by inhomogeneity.

2.4.1 Material loss

Fabelinskii classified major material losses in crystal, owing to Brillouin (Raman) and Rayleigh scattering [55]. From the phenomenological aspect, the light scattering is the consequence of fluctuation in the optical properties of medium, e.g. a refractive index or dielectric constant.

$$\Delta\epsilon = \underbrace{\left(\frac{\partial\epsilon}{\partial p}\right)_S \Delta p}_{\text{Brillouin}} + \underbrace{\left(\frac{\partial\epsilon}{\partial S}\right)_p \Delta S}_{\text{Rayleigh}}, \tag{2.28}$$

where ϵ is the dielectric constant of medium, p is the pressure, and S is the entropy. Let us focus on the case where only acoustic pressure waves perturb a dielectric constant of medium (isothermal process). Thus, this perturbed constant results in scattered light caused by a momentum-assisted process. Generally, Brillouin (or Raman) scattering through adiabatic fluctuation is a dominant loss mechanism in perfect crystals. On the other hand, thermal elastic waves can change a dielectric constant through the equipartition theorem $\sqrt{\langle u^2 \rangle} = \sqrt{3kT/m}$ [55], which is called Rayleigh wing scattering. However, such themorefractive noise is limited by thermodynamics, thereby it is relatively smaller than Brillouin (or Raman) scattering. Gorodetsky and Grudinin [88] experimentally demonstrated thermorefractive noise in a microsphere resonator.[28] Besides, electron-photon scattering, called absorption, cannot be negligible if a medium such as silicon is heavily doped. In such a case, interband and intersubband transitions contribute light absorption to create electron-hole pairs which lead to photon energy loss.

However, elastic collision represented by Rayleigh scattering (not Rayleigh wing scattering) can also induce energy loss in noncrystalline materials. Apetz and Bruggen analyzed the scattering at pores, grain boundaries, or dislocations in-

[28] Their system was not crystalline though.

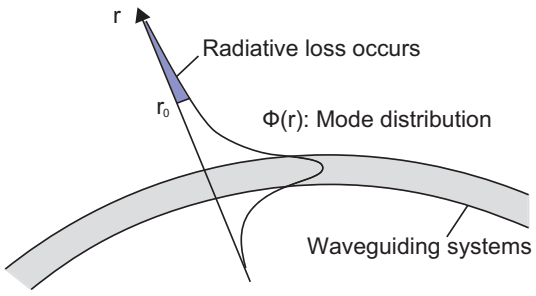

Figure 2.14: Curved waveguide systems give asymmetric spatial mode functions in the radial direction. The phase velocity after the critical radius r_o toward the radial direction (blue-shaded area) is higher than the speed within r_o. Hence, each phase becomes different, and light in the blue-shaped area is not guided but radiated.

ducing loss in alumina which is polycrystalline [89]. Their approach also enables characterizing material losses in amorphous materials, whose structures are more random compared to crystals. Such randomness induced during fabrication processes – most likely annealing – can be frozen inside amorphous materials, therefore light can be scattered by these frozen-in fluctuations. Pinnow et al. reported that Rayleigh scattering caused by frozen-in fluctuations contributes material losses in silica fibers [10].

2.4.2 Radiative loss

Suppose waveguiding systems are bending as shown in Fig. 2.14. Here, the shaded area indicates the waveguide and the skew Lorenzian shape illustrates the propagating spatial mode function $\phi(r)$. As discussed in Section 2.2, evanescent fields are observed outside systems with the extinction coefficient, so they decay exponentially outside the linear waveguide. The evanescent fields are non-radiative as they have same phases of their wave fronts inside the waveguide. That is because the evanescent fields share the"effective" refractive index with the guided wave inside the waveguide. However, energy can be distributed indefinitely in the transverse direction in the presence of bending (Fig. 2.14), thereby the spatial mode distribution is extended more than $r_0 \equiv R\left[(n_0/n_{\text{eff}}) - 1\right]$ [90, 91]. Here R is the radius of curvature, n_0 is the refractive index of air, and n_{eff} the effective index. The distribution at $r > r_0$ eventually has the phase which should be different from the phase of the wave inside the waveguide, as the refractive index at $r > r_0$ is purely n_0. As a result, light outside r_0 radiates. Such radiative loss also happens in the case of resonators [42].

The radiative loss becomes dominant when a radius of curvature is much larger than the wavelength, hence it is generally negligible in WGM resonators.

2.4.3 Scattering loss

Scattering loss induced by inhomogeneities can limit the performance of optical and mechanical devices at the microscale, resulting in the intrinsic loss increased. (See the detailed discussion for scattering loss induced by disorder in Section 1.1.1)

Chapter 3

Fabrication and Measurement of Brillouin optomechanics

Here, we investigate how to manufacture an optical WGM resonator, fabricate a tapered fiber, and experimentally couple the resonator to the tapered fiber. We also discuss the specific calibration methods for extracting the power spectral density of mechanical modes and the optical transmission.

3.1 Experimental setup for Brillouin optomechanics

3.1.1 Fabrication of tapered fiber

Figure 3.1(a) illustrates how to fabricate a tapered fiber similar to the method described in [92]. As mentioned in Chapter 2, the goal of fabricating a tapered fiber is to obtain a "single-mode" waveguide that enables evanescent coupling to resonators. The fiber jacket is stripped off to expose the cladding where the tapered fiber is fabricated. After cleaning the exposed region with ethanol, we place the fiber in two V-groove holders, with the stripped area centered between the holders. These holders are each placed on a linear stage (See Fig. 3.1(c)). A reprogrammable interface from a PC enables dynamic control of these motorized linear stages which pull the fiber uniformly until the fiber tapers down to $1 \sim 2\ \mu m$ diameter, as shown in Fig. 3.1(b). The program is set to pull each linear stage at a uniform speed for ~ 50 seconds. As a quality control measure, a camera and an oscilloscope are set to monitor the fiber fabrication process simultaneously. This camera is placed in the center of the fiber to observe its tapering. A torch tip installed on the bottom of the setup is connected to a hydrogen tank which is capable of generating temperature up to $\sim 1,700°\text{C}$, the melting point of the SMF-28. The flow of hydrogen can be controlled manually, and the flame is adjusted to $1 \sim 2$ cm height for each experiment. Typically this hydrogen flame is only visible in a dark room. Next, the

program for controlling the linear stages is run with uniform speed so as to pull the fiber appropriately. Initially, transmission measured at the oscilloscope is steady which indicates a single-mode operation for $\sim$ 10 seconds. Then, the transmission enters a multimode oscillation period and becomes flat in the end, where a single-mode taper is successfully built (See Figure 3.2).

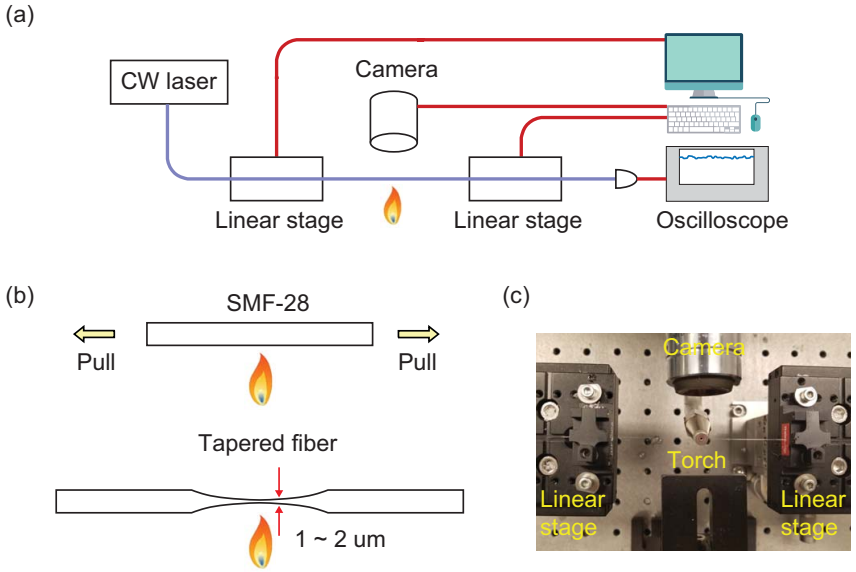

Figure 3.1: (a-b) Schematic of the taper pulling setup. Two linear stages on each side draw the SMF-28 connected from the continuous-wave (CW) laser. These programmable stages pull the fiber uniformly, while the hydrogen torch melts the fiber. The oscilloscope from the photodetector measures transmission change during the pulling process. The taper pulling is done until it becomes a single mode fiber. At the same time, one can observe the pulling process through the camera set in front of a taper. (c) Experimental setup for pulling tapers.

3.1.2 Fabrication of fused silica resonators

A piece of tapered fiber (Fig. 3.3(b)) is prepared to build a fused silica microsphere resonator and is placed on the V-groove of the fiber fusion splicer. In general, the fiber fusion splicer is used to weld two fibers by an electric arc from electrodes as shown in Fig. 3.3(a). Here, the splicer can liquefy the silica fiber tip to build spherical resonators. Figure 3.3(c) shows a fused silica microsphere resonator after the fabrication process.

Let us consider the actual resonator used in experiments. This resonator has

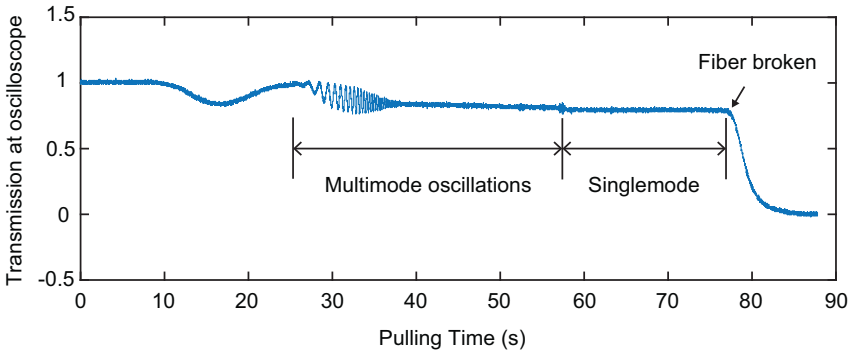

Figure 3.2: Transmission change in the taper pulling. The fiber becomes a multimode fiber under the pulling process after $\sim$ 20 seconds such that its transmission oscillates. These multimode oscillations eventually end, and the transmission becomes flat; only single mode is guided in the fiber whose diameter is less than $\sim 2\ \mu m$. If the pulling is going on further, the fiber is broken in the end as its diameter is too small to withstand applied tension.

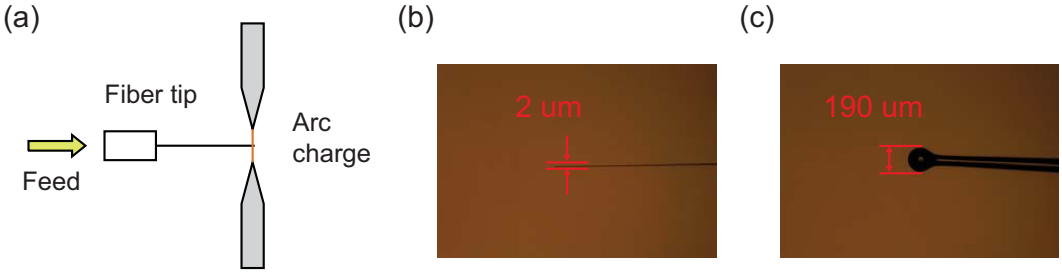

Figure 3.3: (a) Schematic of building sphere resonators. Arc charge generated from electrodes in a fusion splicer can melt a fiber tip which is drawn by hands. Specifically, one pulls the fiber tip with rotating the tip when the arc charge is on. (b-c) Measurement of a fiber tip whose diameter is $\sim 2\ \mu m$, and a fabricated sphere resonator.

an additional stem from a spherical resonator to hold it on the V-groove (See Figure 3.4(a)). Here, the attached stem can create additional mechanical losses, i.e. clamping losses.[1] The clamping losses in the silica sphere resonator can be easily simulated and characterized using the finite element method as illustrated in Fig. 3.4(b).[2] The clamping losses related Q-factor tends to increase with decreasing the stem radius. Hence, we must design a stem of resonators small enough to minimize the additional losses.

[1] An understanding of clamping losses is essential for designing WGM resonators in an appropriate way. In reality, waves confined to structures tend to propagate up to their substrate through tethers, thereby mechanical modes become dissipative, i.e. clamping losses. The clamping losses can be dominant in nano/microstructures, as they rely on a geometrical aspect ratio.

[2] The simulation is conducted with the 67.5 μm radius sphere with varying the stem radius. See Appendix B for the detailed method

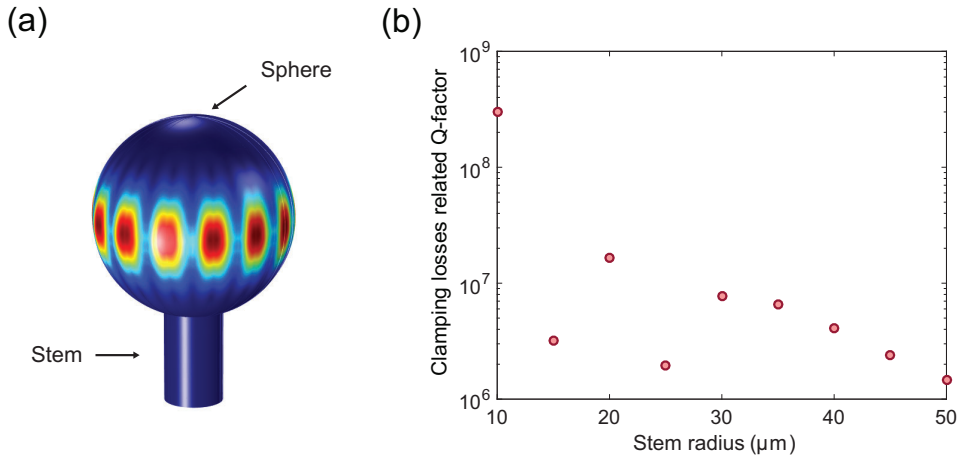

Figure 3.4: (a) Illustration of an acoustic WGM in the sphere resonator with the stem. (b) The Q-factor of clamping losses decreases with increasing the stem radius.

3.2 Experimental setup for Brillouin optomechanics

The experiment is performed in the configuration shown in Fig. 3.5. To measure Brillouin optomechanical interaction in a WGM resonator, we must ensure evanescent coupling of a resonator to a tapered fiber. We mount a sphere resonator in the V-groove holder which is place on the nanostage (See Fig. 3.5(a)). After fabricating a taper fiber, we place the fiber on a mobile holder. The taper holder is also mounted on a nanostage as illustrated in Fig. 3.5(a) and (b). Figure 3.5(c) illustrates the top and side view of the coupling captured from the camera that is set in front of the setup. Note that the position of the taper is adjusted not to be stuck to the resonator.

The measurement setup used for our experiments is presented in Fig. 3.6. We employ fused-silica microsphere resonators that are evanescently coupled to a taper fiber waveguide for probing. A 1520 nm to 1570 nm tunable external cavity diode laser was employed to drive optical pump into the waveguide. The laser source was split into the forward and backward pathways using a 90/10 splitter. An Erbium-doped fiber amplifier (EDFA) amplifies the pump power in the forward pathway only (i.e. for cw pumping of the resonator). Electro-optic modulators (EOMs) are used for regulating pump power in both directions by modifying their respective dc bias, and also for producing the optical probes. Fiber polarization controllers (FPC) are used to adjust the forward and backward probe polarizations to match

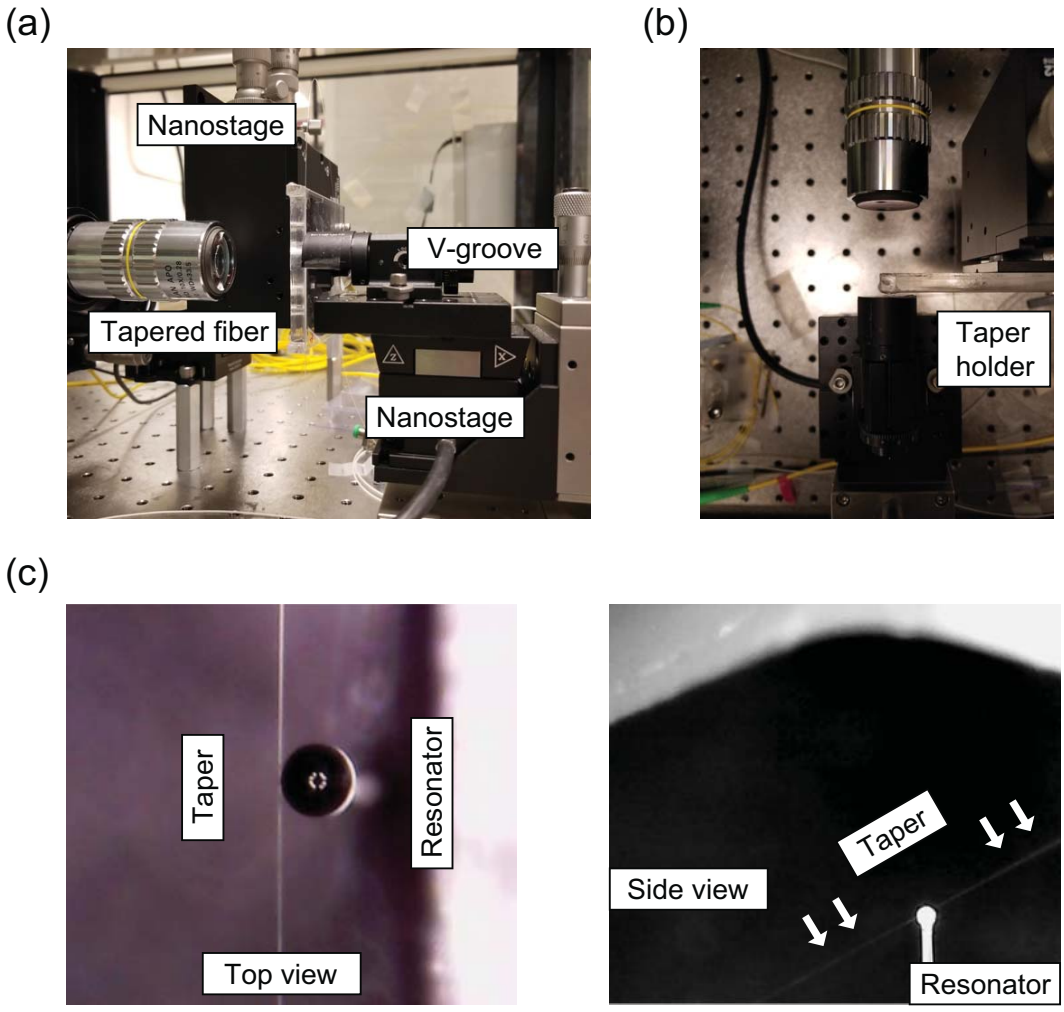

Figure 3.5: (a) A sphere resonator is mounted on the V-groove which is controlled by a nanostage. (b) A tapered fiber is placed on the mobile holder by an optical glue. This holder is also controlled by a XYZ stage. (c) Top and side view of a taper-resonator coupled system.

the resonator modes.

During experiments, the probe sidebands generated by the EOMs are swept through the $a_{\pm}$ mode. The input and output fields are measured at four photodetectors; the optical signals after coupling to the resonator are collected at PD1 and PD2. Alongside, PD3 and PD4 are placed just after the EOMs to obtain 1% of the optical signal for reference. We use two circulators for performing simultaneous measurement of the forward and backward probe transmissions and reflections.

As discussed above, we have utilized a pump-probe measurement that is a technique for investigating the optical mode response from Brillouin optomechanics. Here we rewrite Eq. 2.19 to acquire the expression of the pump-probe measurement in Brillouin interaction.

$$\begin{aligned}
\dot{a}_p &= -(\kappa_p/2 + i\Delta_p)a_p - igb^* a_s + \sqrt{\kappa_{ex}}a_{p,in}, \\
\dot{a}_s &= -(\kappa_s/2 + i\Delta_s)a_s - igba_p + \sqrt{\kappa_{ex}}a_{s,in}, \\
\dot{b} &= -(\Gamma/2 + i\Delta_b)b - iga_p^* a_s + \sqrt{\Gamma}b_{\mathrm{th}}(t).
\end{aligned} \tag{3.1}$$

Here the detunings are given by $\Delta_p = \omega_p - \omega_L$, $\Delta_s = \omega_s - \omega_{\mathrm{probe}}$ and $\Delta_b = \omega_m - (\omega_L - \omega_{\mathrm{probe}})$, where ω_L and ω_{probe} are the pump and probe laser frequencies. $a_{p,in}$ and $a_{s,in}$ are the dimensionless amplitudes that represent the pump and probe, respectively. Using the input-output formalism described in Eq. (2.13), we obtain

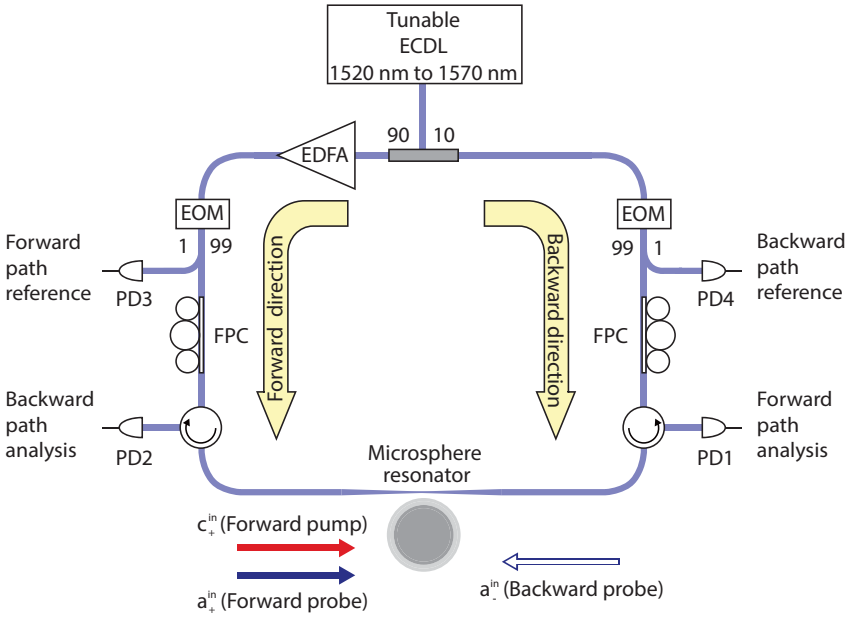

Figure 3.6: Experimental setup details. A fiber-coupled tunable external cavity diode laser (ECDL) is sent through a 90/10 fiber splitter to produce forward and backward propagating optical signals. An erbium doped fiber amplifier (EDFA) in the forward direction controls the pump laser power. Electro-optic modulators (EOMs) are additionally help produce the forward and backward probes laser, while fiber polarization controllers (FPCs) are used to match polarization with the resonator modes. Four photodetectors (PDs) help perform transmission and reflection measurements assisted by circulators. The measured signals from the PDs are analyzed using an oscilloscope, electrical spectrum analyzer, and an electrical network analyzer.

the probe transmission in the following equation:

$$\tilde{t}_p \;=\; \frac{a_{s,out}}{a_{s,in}} \;=\; 1 - \frac{\kappa_{\rm ex}}{(\kappa_s/2 + i\Delta_s) + G^2/\left(\Gamma/2 + i\Delta_b\right)}. \tag{3.2}$$

We note that $a_{s,out}$ results from the input-output formalism which is given by $a_{s,out} = a_{s,in} - \sqrt{\kappa_{\rm ex}} a_s$.

3.3 Calibration of optical transmission and reflection coefficients

3.3.1 Transmission coefficients

[3] Here we describe the procedure for determination of transmission coefficients using optical probe signals and a network analyzer.

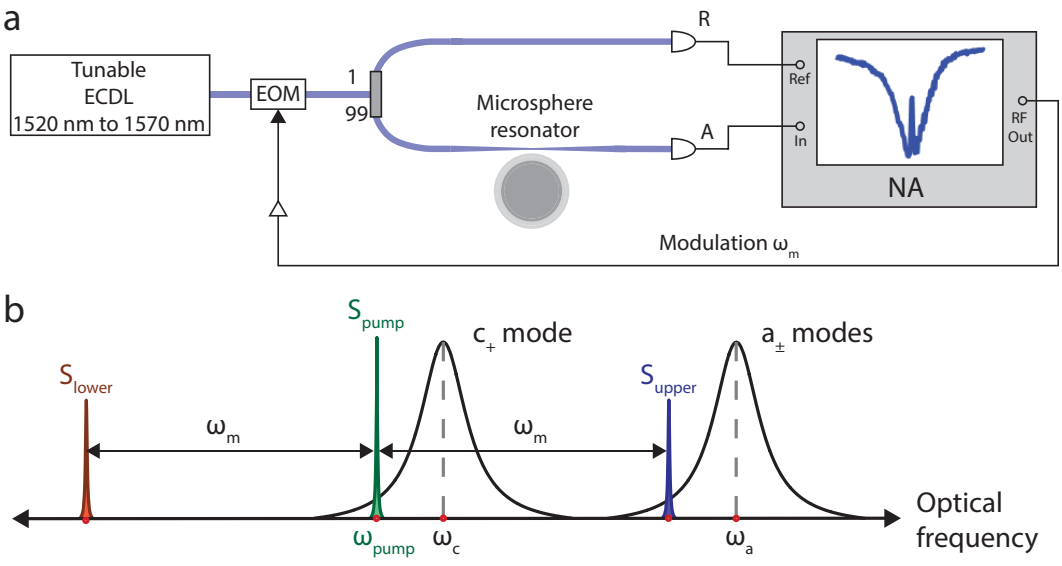

Figure 3.7: **(a)** Schematic for transmission measurements distilled from Fig. 3.6. **(b)** The EOM produces two optical sidebands to the pump or carrier laser field ($S_{\rm pump}$). While the pump is parked within the c_+ mode, the upper sideband is able to probe the $a_\pm$ modes. We detail the mathematics for the measurement in §3.3.1.

For illustration purposes, the schematic of a typical transmission measurement

[3] Portions of this chapter are available at arXiv:1803.02366(under review)

is presented in Fig. 3.7a. We use 1 % of the modulated signal after the EOM as a reference at photodetector R, while 99 % of the signal is coupled to the resonator via waveguide and its transmission is measured at photodetector A. Since we use an EOM to produce the probe signal (from the pump), there exist two sidebands $\omega_{\text{pump}} \pm \omega_m$ relative to the pump that propagate through the system, where ω_m is the modulation frequency received from the network analyzer. All optical signals and their positions in frequency space are illustrated in Fig. 3.7b. Only the upper sideband marked S_{upper} measures the $a_\pm$ mode of interest, while the lower sideband marked S_{lower} passes through the waveguide without interacting with the resonator. Therefore, the upper sideband is used as the optical probe.

The received optical intensities at the two photodetectors can then be expressed as:

$$\left| E_R\, e^{-i\omega_{\text{pump}}t} \left(1 + \frac{\mathcal{B}}{2} e^{-i\omega_m t} + \frac{\mathcal{B}}{2} e^{i\omega_m t}\right) + \text{ c.c} \right|^2 \tag{3.3a}$$

$$\left| E_A\, e^{-i\omega_{\text{pump}}t} \left(t_c + t_{us}\frac{\mathcal{B}}{2} e^{-i\omega_m t} + t_{ls}\frac{\mathcal{B}}{2} e^{i\omega_m t}\right) + \text{ c.c} \right|^2 \tag{3.3b}$$

where $\mathcal{B}$ is the EOM intensity modulation coefficient, while E_R and E_A are the amplitudes of electric fields in the reference and resonator paths respectively. Here we have defined t_c, t_{us} and t_{ls} as the transmission coefficients of the optical carrier (pump), upper sideband (probe), and lower sideband signals, respectively. The output photocurrent is proportional to the optical intensity expressed in Eqns (3.3). However, since the detectors have limited bandwidth in the RF domain, and the network analyzer only measures terms at frequency ω_m, the only terms of interest in the output photocurrents are :

$$R = 2|E_R|^2 \mathcal{B} \cos(\omega_m t) \tag{3.4a}$$

$$A = \frac{t_c |E_A|^2 \mathcal{B}}{2} \left(e^{i\omega_m t} + t_p e^{-i\omega_m (t+\phi')}\right) + \text{ c.c} \tag{3.4b}$$

Here, we have simplified $t_c = t_c^*$ to set it as a reference phase, $t_{ls} = e^{i\omega_m \phi'}$ since the lower sideband does not interact with the resonator, and $t_{us} = t_p e^{-i\omega_m \phi'}$ with the new subscript indicating that it is the optical probe. We can now rewrite Eqn. (3.4b)

as follows :

$$A = \frac{t_c|E_A|^2\mathcal{B}}{2}\left[\left\{(1+t_p')\cos(\omega_m\phi') + t_p''\sin(\omega_m\phi')\right\}\cos(\omega_m t) + \left\{t_p''\cos(\omega_m\phi') - (1+t_p')\sin(\omega_m\phi')\right\}\sin(\omega_m t)\right]$$

The network analyzer in the configuration of Fig. 3.7a provides a complex-valued ratio of A to R. This result can be separated into in-phase (X) and quadrature (Y) terms as follows:

$$X = \frac{t_c M}{2}\left[(1+t_p')\cos(\omega_m\phi') + t_p''\sin(\omega_m\phi')\right] \tag{3.5a}$$

$$Y = \frac{t_c M}{2}\left[t_p''\cos(\omega_m\phi') - (1+t_p')\sin(\omega_m\phi')\right] \tag{3.5b}$$

where M is a proportionality constant that includes the power split ratio (1:99), the slight difference in photodetectors' responsivities, and the difference in gain of the two optical paths. We can then write the calibrated probe transmission coefficient t_m as follows :

$$\begin{aligned} t_m &= X + iY \\ &= \frac{t_c M}{2}\left[(1+t_p'+t_p'')\cos(\omega_m\phi') - i(1+t_p'+t_p'')\sin(\omega_m\phi')\right] \\ &= \frac{t_c M}{2}(1+t_p)e^{-i\Phi} \ . \end{aligned} \tag{3.6}$$

Since the carrier (pump) transmission t_c, M, and the waveguide dispersion contribution $\Phi = \omega_m\phi'$ are experimentally measurable, we can extract the true transmission coefficient t_p after performing simple calibrations.

3.3.2 Reflection coefficients

We can now similarly calibrate the optical response to obtain the reflection coefficient using a backward photodetector (via circulator) on the 99 % branch. The measured optical intensity at this backward photodetector is given as :

$$\left| E_A e^{-i\omega_{\text{pump}}t}\left(r_c + r_{us}\frac{\mathcal{B}}{2}e^{-i\omega_m t} + r_{ls}\frac{\mathcal{B}}{2}e^{i\omega_m t}\right) + \text{ c.c}\right|^2 \tag{3.7}$$

where r_c, r_{us} and r_{ls} are the reflection coefficients of carrier, upper sideband and lower sideband modes, respectively. Once again, we set the carrier (pump) as the reference $r_c = r_c^*$, and since the lower sideband does not interact with the resonator we can say $r_{ls} = 0$. We can then rewrite the upper sideband reflection coefficient as $r_{us} = r_p e^{-i\omega_m \phi'}$ to indicate the probe reflection coefficient $r_p = (r_p' + i r_p'')$.

$$A = \frac{r_c |E_A|^2 \mathcal{B}}{2} \left[\left\{ r_p' \cos(\omega_m \phi') + r_p'' \sin(\omega_m \phi') \right\} \cos(\omega_m t) + \left\{ r_p'' \cos(\omega_m \phi') - r_p' \sin(\omega_m \phi') \right\} \sin(\omega_m t) \right]$$

As before, the in-phase (X) and quadrature (Y) terms from the network analyzer can be written.

$$X = \frac{r_c M}{2} \left[r_p' \cos(\omega_m \phi') + r_p'' \sin(\omega_m \phi') \right] \tag{3.8a}$$

$$Y = \frac{r_c M}{2} \left[r_p'' \cos(\omega_m \phi') - r_p' \sin(\omega_m \phi') \right] \tag{3.8b}$$

Once again, we can write $r_m = X + iY$ to produce a calibrated reflection coefficient, from which the true reflection coefficient r_p can be determined once t_c, M, and $\Phi = \omega_m \phi'$ are experimentally measured.

$$r_m = \frac{r_c M}{2} \left[(r_p' + r_p'') \cos(\omega_m \phi') - i (r_p' + r_p'') \sin(\omega_m \phi') \right] = \frac{t_c M}{2} r_p e^{-i\Phi} \tag{3.9}$$

3.4 Measuring phonon mode spectra using a photodetector

[4] As discussed in Section 3.2, the intensity of optical signal after coupling to a resonator is measured at photodetectors which provide photocurrent, and the spectrum of the photocurrent is analyzed at a real-time spectrum analyzer. Here, we have to understand the measurement of the output spectrum at the photodetector in detailed. Using the equations (2.19), we can rewrite the Heisenberg-Langevin equations for the b phonon mode in the Fourier domain with the rotating wave

[4] Portions of this chapter are reprinted with permission from Kim, S., et. al., (2017),"Dynamically induced robust phonon transport and chiral cooling in an optomechanical system," Nature Communications, 8, 205.

approximation.

$$-i\omega a_p = -\left(\frac{\kappa_p}{2} + i\Delta_p\right) a_p - iga_s b^\dagger + \sqrt{\kappa_{\rm ex}} a_{\rm in}(t), \tag{3.10a}$$

$$-i\omega a_s = -\left(\frac{\kappa_s}{2} + i\Delta_s\right) a_s - iga_p b + \sqrt{\kappa_i} a_{\rm vac}(t), \tag{3.10b}$$

$$-i\omega b = -\left(\frac{\Gamma}{2} + i\omega_m\right) b - iga_p^\dagger a_s + \sqrt{\Gamma} b_{\rm th}(t). \tag{3.10c}$$

Here the detunings are defined by $\Delta_p = \omega_p - \omega_L$ and $\Delta_p = \omega_s - \omega_L$, where ω_L is the pump laser frequency. And the pump laser $a_{\rm in}$ is considered the stationary ergodic noise force as follows. The quantum correlation functions of these noise forces are thus given by:

$$\begin{aligned}
\langle a_{\rm in}^\dagger(t) a_{\rm in}(t')\rangle &= n_L(t'-t),\\
\langle a_{\rm in}(t) a_{\rm in}^\dagger(t')\rangle &= (n_L+1)(t'-t),\\
\langle a_{\rm vac}^\dagger(t) a_{\rm vac}(t')\rangle &= 0,\\
\langle a_{\rm vac}(t) a_{\rm vac}^\dagger(t')\rangle &= \delta(t-t'),\\
\langle b_{\rm th}^\dagger(t) b_{\rm th}(t')\rangle &= \bar{n}\delta(t-t'),\\
\langle b_{\rm th}(t) b_{\rm th}^\dagger(t')\rangle &= (\bar{n}+1)\delta(t-t')
\end{aligned}$$

where n_L is the photon occupation number from the pump laser and $\bar{n}$ is the occupation number of phonons. We then obtain the noise spectrum of the b mode as follows:

$$b(\omega) = \frac{\sqrt{\Gamma} b_{\rm th}(\omega)}{\Gamma_{\rm e}/2 + i(\omega_{\rm m.e} - \omega)} - \frac{iG\sqrt{\kappa_{\rm ex}} c_-^{\rm in}}{\left[\Gamma_{\rm e}/2 + i(\omega_{\rm m.e} - \omega)\right]\left[\kappa/2 - i(\omega - \Delta_s)\right]} \tag{3.11}$$

where $\omega_{\rm m.e}$ is the effective mechanical frequency including the optical spring effect and $\Gamma_{\rm e} = \Gamma + \Gamma_{\rm opt}$ is the effective mechanical damping rate including the optomechanical damping rate $\Gamma_{\rm opt}$ in Eq. (2.21). We can then derive the output spectrum measured at the downstream photodetector after the resonator. Using the input-output theory [50], we obtain the expression for the output field in the optical waveguide.

$$
\begin{aligned}
a_{\mathrm{out}}(\omega) &= a_{\mathrm{in}}(\omega) - \sqrt{\kappa_{\mathrm{ex}}} a_s(\omega) \\
&= a_{\mathrm{in}}(\omega)\left[1 - \frac{2\kappa_{\mathrm{ex}}}{\kappa_{\mathrm{p}} - 2i(\omega - \Delta_p)}\right] \\
&\quad + a_{\mathrm{vac}}(\omega)\left[1 - \frac{2\kappa_{\mathrm{ex}}}{\kappa_s - 2i(\omega - \Delta_s)} + \frac{|G|^2\kappa_{\mathrm{ex}}}{\left[\Gamma_{\mathrm{e}}/2 + i(\omega_{\mathrm{m.e}} - \omega)\right]\left[\kappa_s/2 - i(\omega - \Delta_s)\right]^2}\right] \\
&\quad + b_{\mathrm{th}}(\omega)\frac{iG\sqrt{\Gamma}\sqrt{\kappa_{\mathrm{ex}}}}{\left[\Gamma_{\mathrm{e}}/2 + i(\omega_{\mathrm{m.e}} - \omega)\right]\left[\kappa_s/2 - i(\omega - \Delta_s)\right]} \\
&= s_1(\omega)a_{\mathrm{in}}(\omega) + s_2(\omega)c_-^{\mathrm{in}}(\omega) + s_b(\omega)a_-^{\mathrm{eff}}(\omega)
\end{aligned}
\tag{3.12}
$$

where we are introducing the scattering matrix elements $s_1(\omega)$, $s_2(\omega)$ and $s_b(\omega)$ defined in [93]. The output spectrum at the photodetector is related to the spectrum of the normalized photocurrent $S_{II}(\omega')\delta(\omega - \omega') = \langle I(\omega)^\dagger I(\omega')\rangle$ where $I(\omega) = S_{\mathrm{out}}(\omega) + S_{\mathrm{out}}^\dagger(\omega')$. Thus, $S_{II}(\omega)$ is:

$$
S_{II}(\omega) = \left(|s_1(\omega)|^2 + |s_2(\omega)|^2 + |s_b(\omega)|^2\right) + 2n_L|s_1(\omega)|^2 + 2\bar{n}|s_b(\omega)|^2 \tag{3.13}
$$

The phonon noise spectrum $S_{a_-}(\omega) = \frac{\bar{n}\,\Gamma}{(\Gamma_e/2)^2 + (\omega_{\mathrm{m.e}} - \omega)^2}$ is included in the above expression through the scattering element $2\bar{n}|s_b(\omega)|^2$, since the mechanical scattering matrix elements is $2\bar{n}|s_b(\omega)|^2 = \frac{2\Gamma_{\mathrm{opt}}\kappa_{\mathrm{ex}}}{\kappa}\frac{\bar{n}\,\Gamma}{(\Gamma_e/2)^2 + (\omega_{\mathrm{m.e}} - \omega)^2}$. The remainder of the equation constitutes the noise floor N, which is a function of n_L. The resulting photocurrent spectrum is given by:

$$
S_{II}(\omega) = N + \frac{2\Gamma_{\mathrm{opt}}\kappa_{\mathrm{ex}}}{\kappa} S_{a_-}(\omega) \tag{3.14}
$$

Thus, the measured RF output spectrum at the photodetector (ignoring noise floor N) is proportional to the spectrum of the mechanical mode b, scaled by the optomechanical damping rate $\Gamma_{\mathrm{opt}} = \frac{4|G|^2}{\kappa}$ when $\omega \approx \omega_{\mathrm{m.e}}$. Thus, the spectrum obtained in $S_{II}(\omega)$ is directly representative of the phonon population and temperature of the mode.

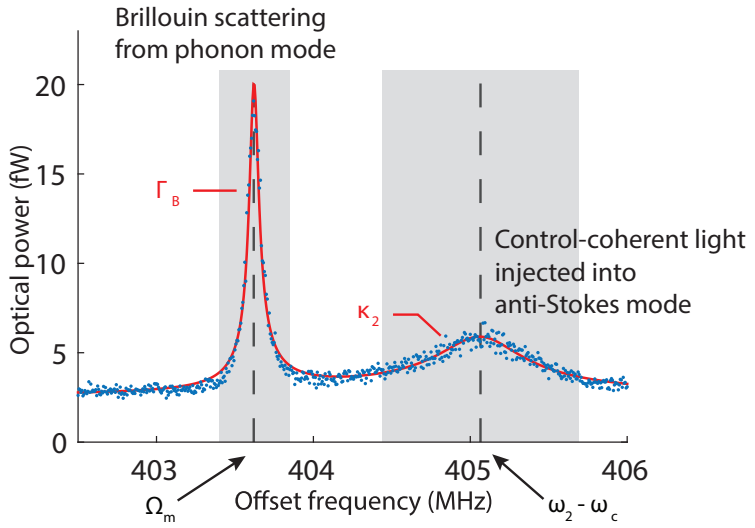

Figure 3.8: Measurement of Brillouin scattering at Ω_m and the control-coherent background light (from defect induced scattering and direct injection) shaped by the anti-Stokes optical mode at ω_2. Both sources are offset from the control laser by roughly 404 MHz. This measurement is derived from their beating with the control field on a photodetector and measured by an RF electronic spectrum analyzer. The additional background light is typically too small to be observed except when it is resonantly amplified by an ultra-high-Q resonator. The Brillouin scattering occurs at a fixed frequency defined by the phonon mode Ω_m while the background light is tunable by modifying the control laser frequency.

3.5 Background light in probe measurements

[5] In ultra-high-Q resonators, coherent spontaneous light scattering from the control laser by small intrinsic defects can populate the anti-Stokes optical mode. There may also be direct injection of the control laser into the anti-Stokes optical mode. While this extra light is generally small, it does result in competition with the small amount of anti-Stokes light scattering from the acoustic mode in the structure (the phenomenon of interest) and can contaminate measurements of $\tilde{t}_p$. An exemplary measurement of this spurious light is shown in Fig. 3.8. Since both light sources are being generated from the same pump/control laser, there can be interference that complicates the measurement of the probe transmission (Fig. 3.9).

We can easily observe the evidence of this additional light in the background using an electrical spectrum analyzer that monitors the RF power measurement

[5]Portion of this chapters are reprinted with permission from Kim, J., Kim, S., et. al., (2017), "Complete linear optical isolation at the microscale with ultralow loss," Scientific Reports, 7, 1647.

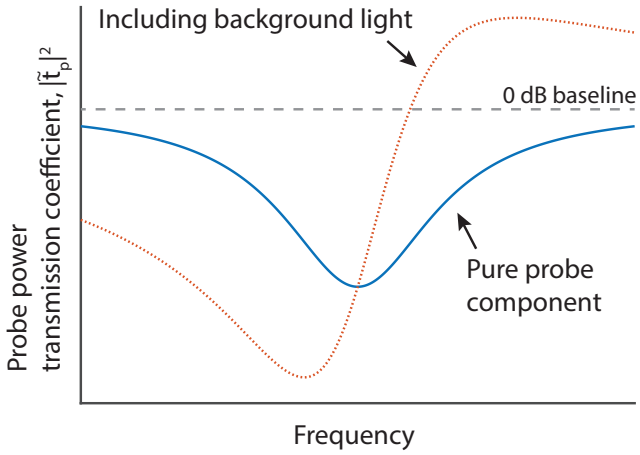

Figure 3.9: The network analyzer measurement shows an asymmetric probe power transmission coefficient $\left|\tilde{t}_p\right|^2$ (red-dotted line) in spite of the optical mode being symmetric. The distortion in the measurement originates from the background light injected to the anti-Stokes optical mode, creating difficulty in the estimation of the 0 dB transmission baseline (grey-dashed line) and optical mode center frequency. After correcting for the background light, the symmetric optical transmission is seen (blue-solid line).

from the photodetector. Fig. 3.8 shows the spectrum of beat notes generated from scattering by the acoustic phonon mode centered at $\Omega_m = 403.6$ MHz, and from background light within the anti-Stokes optical mode centered at $\omega_{as} = 405.1$ MHz offset from the control laser frequency. Since the resonant frequency of the phonon mode is fixed, the frequency of the beat note originating from Brillouin scattering does not change when the control laser frequency changes. However, the beat note generated from the control-coherent background light injected into the anti-Stokes optical mode can be moved in frequency space with the control laser.

Since the proposed sources of background light (defect scattering, direct injection) are proportional to the intracavity control field a_1, we can model them as a coherent source driving the anti-Stokes mode with coupling strength r relative to the control field. This extra source can be included in Eq. (3.1) describing our system as follows :

$$\begin{aligned}
\dot{a}_p &= -(\kappa_p/2 + i\Delta_1)a_p - igb^* a_s + \sqrt{k_{ex}}a_{p,in} \\
\dot{a}_s &= -(\kappa_s/2 + i\Delta_2)a_s - igba_p + \sqrt{k_{ex}}a_{s,in} + ira_p \\
\dot{b} &= -(\Gamma/2 + i\Delta_B)b - iga_p^* a_s + b_{\text{th}}(t) \\
a_{i,out} &= a_{i,in} - \sqrt{k_{ex}}\, a_i \mid \text{where } i{=}p,s
\end{aligned} \tag{3.15}$$

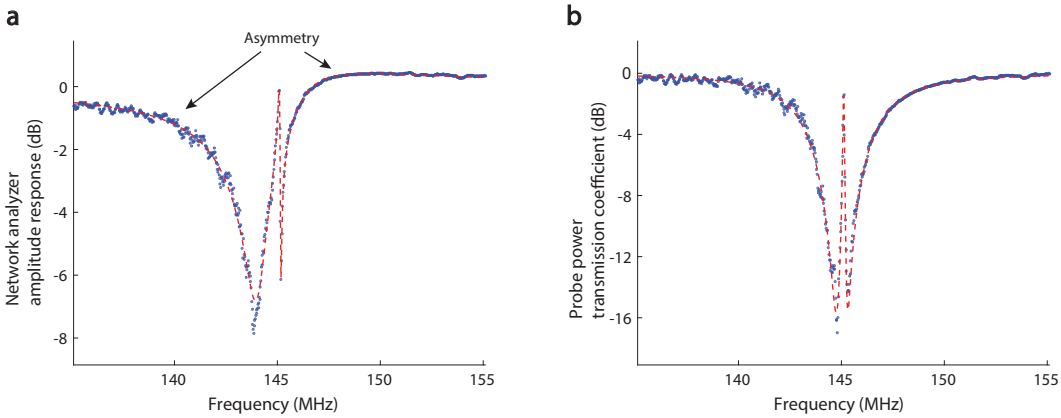

Figure 3.10: **a.** Raw amplitude response data from the network analyzer. The optical transmission measurement and the induced transparency are distorted by the additional light within the anti-Stokes optical mode. **b.** Probe optical power transmission is plotted using input-output relation after removal of the background light. Data shows transparency within the Lorentzian shaped optical mode. The red dashed line represents a fit using theoretical model for induced transparency.

As discussed in Chapter 2, the control field scattering $igb^* a_s$ and thermal fluctuation $b_{\text{th}}(t)$ can be negligible. We find the modified steady-state intracavity probe field a_s which is composed of the unperturbed probe response and an additional background light term:

$$\begin{aligned} a_s &= \frac{\sqrt{k_{ex}} a_{s,in}}{\gamma_s + G^2/\gamma_B} + \frac{ira_p}{\gamma_s + G^2/\gamma_B} \\ \gamma_i &= \kappa_i/2 + i\Delta_i \\ \gamma_B &= \Gamma/2 + i\Delta_B \end{aligned} \tag{3.16}$$

where $G = |ga_p|$ is the pump-enhanced Brillouin coupling rate. The probe field arriving at the photodetector is then expressed as

$$\begin{aligned} a_{s,out} &= \left(1 - \frac{k_{ex}}{\gamma_s + G^2/\gamma_B}\right) a_{s,in} - \left(\frac{ir\sqrt{k_{ex}}}{\gamma_s + G^2/\gamma_B}\right) a_p \\ &= \tilde{t}_{p,\text{actual}}\, a_{s,in} \; - \; \left(\frac{ir\sqrt{k_{ex}}}{\gamma_s + G^2/\gamma_B}\right) a_p \end{aligned} \tag{3.17}$$

implying that the measured probe transmission coefficient (by definition) will be

$$\begin{aligned} \tilde{t}_{p,\text{measured}} &= \frac{a_{s,out}}{a_{s,in}} \\ &= \tilde{t}_{p,\text{actual}} - \left(\frac{ir\sqrt{k_{ex}}}{\gamma_s + G^2/\gamma_B}\right)\frac{a_p}{a_{s,in}} \end{aligned} \tag{3.18}$$

From Eq. (3.18), we note that we can reduce the effect of the background light by increasing the probe laser power (larger $a_{s,in}$) during the experiment such that the first term dominates. The measured transmission coefficient $\tilde{t}_{p,\text{measured}}$ acquired from Eq. (3.6) will then approach the actual transmission coefficient $\tilde{t}_{p,\text{actual}}$. More generally, however, the second interfering term results in an asymmetry (irrespective of acousto-optical coupling) in the optical transmission through high-Q resonators measured by this pump-probe technique.

In Fig. 3.9 we plot Eq. (3.17) with acousto-optical coupling set to zero ($G = 0$). The extra light in the resonator modifies the transmission coefficient such that the high frequency side of the optical mode exceeds 0 dB baseline while the low frequency side is artificially dipped. When we exclude the background light, the plot now reveals a symmetric optical mode and a true resonance frequency. Thus, factoring out this asymmetry is critical in accurately determining the optical isolation performance. Unprocessed transmission measurement from the network analyzer (Fig. 3.10a) shows the asymmetric optical mode shape and different 0 dB baseline levels on either side of the resonance. Such a mismatch in baseline is used to estimate the degree of asymmetry and the coupling strength r. The background light can then be subtracted from the measurement to obtain $\tilde{t}_{p,actual}$ as shown in Fig. 3.10b. In the Fig. 3.10 example, a symmetric optical mode with transparency at the center of the optical mode is revealed.

Chapter 4

Time-reversal symmetry breaking via Brillouin scattering

4.1 Overview of time-reversal symmetry breaking

Time-reversal symmetry (TRS) is one of the fundamental symmetries in physical laws. Time-reversal symmetry is associated with the conservation of entropy[1] which does not hold in the real world, due to the second laws of thermodynamics. However, time-reversal symmetry is still valid in systems without dissipation such as electromagnetism, thereby time-reversal symmetry is practically important from microwave systems to integrated photonics. In this chapter, we focus on photonic systems that are symmetric to the time-reversal operator, defined by $T\psi(t) = \psi(-t)$.[2]

It is known that time-reversal symmetry can be broken in cases where a medium is affected by magnetic fields, called the Faraday effect. Unfortunately, the established magneto-optical techniques [94, 95] for achieving nonreciprocal optical transmission [12] have proven challenging to implement in chip-scale photonics due to fabrication complexity, difficulty in locally confining magnetic fields, and material losses [96, 97, 98, 99]. In light of this challenge, several non-magnetic alternatives for breaking time-reversal symmetry [12] have been explored both theoretically [100, 101, 102, 103, 104, 105] and experimentally [22, 106, 107, 108, 109, 110]. However, various limitations still persist with the proposals that are compatible with chip-scale fabrication. Nonlinearity-based nonreciprocal systems are fundamentally dependent on input field strength [107, 109] and hence do not generate linear response [111]. Dynamic modulation [100, 102] is a powerful approach that generates nonreciprocity, but current chip-scale demonstrations are still constrained by extremely large forward insertion loss and low contrast [106, 108].

[1] Every symmetry operator has each corresponding conservation law, owing to Noether's theorem.

[2] The mathematical definition of the time-reversal operator depends on the basis of systems. In spinless systems which is applicable in optics, the eigenvalue of T^2 is $+1$. Here, T can be defined by $T = UK$, where U is the unitary matrix, and K is complex conjugation.

4.2 Brillouin optomechanics can break time-reversal symmetry

[3] The use of Brillouin acousto-optic scattering to induce unidirectional optical loss [112, 101] is very promising, as it can generate a linear wide-band isolation response. Fundamentally, this nonreciprocal optical transport is obtainable by exploiting selection rules for intermodal Brillouin scattering (See Section 2.3.1). These nonreciprocal effects are based on the phase matching condition via unidirectional pumping as illustrated in Fig. 4.1. As mentioned in Chapter 2, Brillouin interaction can be achieved by an external pump with satisfying the phase matching condition in systems. Here, unidirectional pump is applied to the forward direction only in order to obtain direction-selective Brillouin scattering.[4] In practice, this technique requires

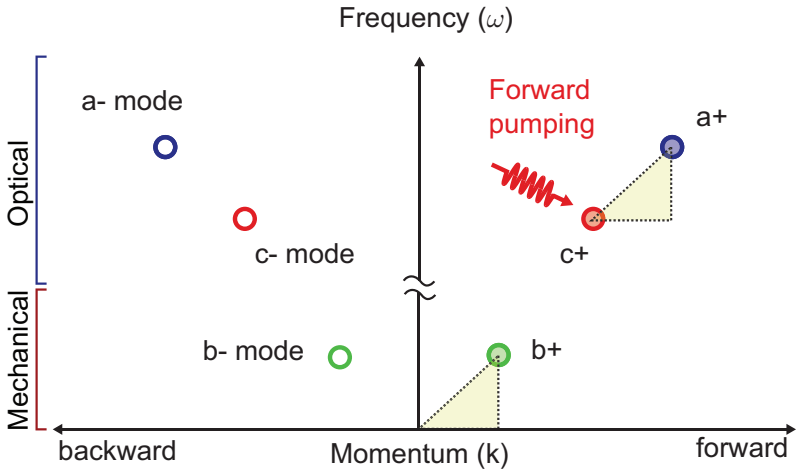

Figure 4.1: Illustration of the direction-selective interaction via Brillouin scattering with unidirectional pump. When the phase matching condition is satisfied, Brillouin interaction occurs only in the forward direction. This direction-selective Brillouin scattering is typically demonstrated via the intermodal transition.

a large product of scattering gain and waveguide length [22], which could soon be realized through advancements in on-chip Brillouin gain [113, 27]. To date, however, there have been no SBS microscale devices having strong nonreciprocity.

[3] Portions of this chapter are reprinted with permission from Kim, J., Kim, S., et. al., (2017), "Complete linear optical isolation at the microscale with ultralow loss," Scientific Reports, 7, 1647.

[4] In fact, the above technique breaks parity symmetry instead of time-reversal symmetry. However, these two symmetries are identical if systems propagate along the boundaries which are geometrically symmetric.

4.2.1 Overview of Brillouin scattering induced transparency

Recently, a fundamentally different path to obtain nonreciprocal optical transport has emerged, by exploiting opto-mechanically induced transparency [18, 19, 114]. These nonreciprocal effects are based on destructive optical interference via a non-radiative acoustic coherence within a resonator-waveguide system, and are acousto-optic analogues of electromagnetically induced transparency (EIT). In this section, we focus our study on the nonreciprocal Brillouin scattering induced transparency (BSIT) mechanism [18], in which momentum conservation requirement between photons and phonons helps break time-reversal symmetry for light propagation.

Let us first qualitatively discuss how nonreciprocity can be achieved by means of the BSIT light-sound interaction in dielectric resonators [18, 19]. We consider a whispering-gallery resonator having two optical modes (ω_1, k_1) and (ω_2, k_2) that are separated in (ω, k) space by the parameters of a high coherence traveling acoustic mode (Ω, q). This is the requisite phase matching relation for BSIT (Fig. 4.2a), indicating that phonons enable coupling of the photon modes through photoelastic scattering. We stress here that the two modes should belong to different mode families of the resonator in order to ensure that scattering to other optical modes from the same phonon population is suppressed. When this system is pumped with a strong 'control' field on the lower optical resonance (ω_1, k_1), an EIT-like optomechanically induced transparency [115, 116] appears within the higher optical resonance (ω_2, k_2), due to coherent interference originating from the acousto-optical interaction [18, 19].

A description of this interference can be presented both classically [18] or through by a quantum mechanical approach [19]. Briefly, one can consider signal or 'probe' photons arriving from the waveguide at frequency ω_2 that are on-resonance and being absorbed by the resonator mode (ω_2, k_2). When the control field is present in a BSIT phase-matching situation, these probe photons could scatter to (ω_1, k_1) causing a mechanical excitation of the system. However, anti-Stokes scattering of the strong control field from this mechanical excitation will generate a phase-coherent optical field that interferes destructively with the original excitation of the mode at (ω_2, k_2). The result is a pathway interference that is measured as an induced optical transparency in the waveguide, where no optical or mechanical excitation takes place, and the resonant optical absorption is inhibited (Fig. 4.2b top). The strength of this interference is set by the intensity of the control laser as presented

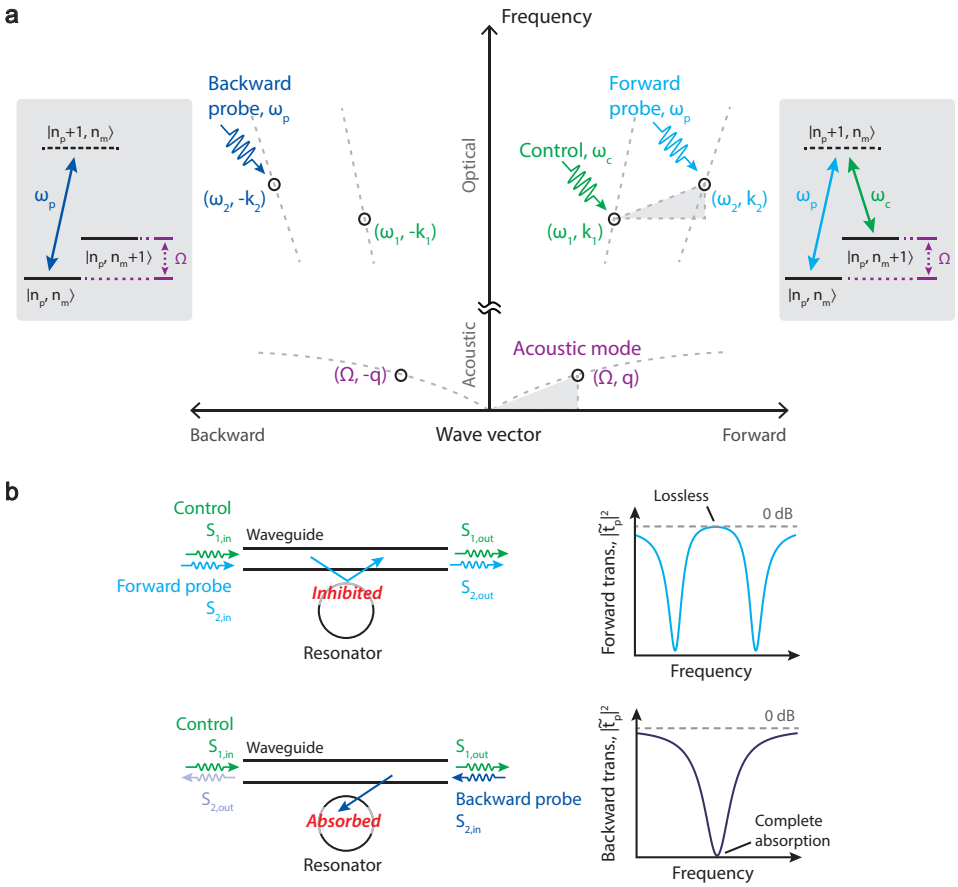

Figure 4.2: Achieving optical nonreciprocity through non-reciprocal Brillouin scattering induced transparency in a whispering-gallery resonator: **a.** The interference of excitation pathways in the BSIT system are described through an energy-level picture (grey boxes), using probe photon number n_p and phonon number n_m. Absorption of a probe photon into the (ω_2, k_2) optical resonance is modeled as an effective transition $|n_p, n_m\rangle \rightarrow |n_p + 1, n_m\rangle$. In presence of the control field, the probe photon could scatter to the lower resonance (ω_1, k_1) while adding a mechanical excitation in (Ω, q), which is an effective transition to state $|n_p, n_m + 1\rangle$. However, the coherent anti-Stokes scattering of the control field from this mechanical excitation would generate an interfering excitation pathway for the original state $|n_p + 1, n_m\rangle$. This process is analogous to EIT and results in a window of transparency for the forward optical probe, inhibiting the original $|n_p, n_m\rangle \rightarrow |n_p + 1, n_m\rangle$ absorption transition. The necessary momentum matching requirement, not visible in the energy diagram, is represented using the dispersion relation (middle) to elucidate the breaking of time-reversal symmetry for the probe signal. **b.** We implement this mechanism using a waveguide and a whispering gallery resonator, in which probe signals tuned to either of the (ω_2, $\pm k_2$) optical resonances are typically absorbed by the resonator under the critical coupling condition. The presence of a forward control field, however, creates the BSIT interference [18] only for forward probe signals and inhibits absorption. Under strong acousto-optical coupling, the waveguide-resonator system is rendered lossless at the original resonance.

in Fig. 2.12. It is crucial, however, to note that this transparency in BSIT only appears for probe signals co-propagating with the control laser. Probe light in the counter propagating i.e. time-reversed direction, on the other hand, occupies the high frequency optical mode with parameters (ω_2, -k_2). For BSIT to occur in this case, an acoustic mode having parameters (Ω, $-(k_1 + k_2)$) would be required for compensating the momentum mismatch between the forward control and backward probe optical modes. However, since such an acoustic mode is not available in the system, no interaction occurs for the counter-propagating probe and the signal is simply absorbed into the resonator (Fig. 4.2b - bottom).

To quantify the above explanation, we rewrite the transmission coefficient $\tilde{t}_p$ of the probe laser field which is presented in Eq. (3.2).

$$\tilde{t}_p \;=\; \frac{a_{s,out}}{a_{s,in}} \;=\; 1 - \frac{\kappa_{\mathrm{ex}}}{(\kappa_s/2 + i\Delta_s) + G^2/\left(\Gamma/2 + i\Delta_B\right)}, \tag{4.1}$$

where $s_{i,\mathrm{in}}$ and $s_{i,\mathrm{out}}$ are the optical driving and output fields in the waveguide (Fig. 4.2b) at the control (i=1) and probe (i=2) frequencies. G is the pump-enhanced Brillouin coupling rate manipulated by the control optical field $s_{1,\mathrm{in}}$ in the waveguide via the relation $G = ga_p$. This response matches the system of optomechanically induced transparency (OMIT) [115, 116], with the exception that the pump field is also resonant and the coupling rate g is dependent on momentum matching. As we explained in Fig. 2.12, the pump resonance in BSIT significantly enhances the maximum coupling rate G achievable in contrast to single-mode OMIT systems.

4.3 Demonstration of optical isolators by Brillouin optomechanics

We previously discussed that nonreciprocal devices by breaking TRS are important for various applications in photonics. The natural question to ask next is that whether we can obtain practical nonreciprocal devices. In fact, we experimentally demonstrate ultra-low loss optical isolation (Fig. 4.3) in the waveguide-resonator system by probing optical transmission through the waveguide in the forward and backward directions simultaneously. A resonator of diameter 170 μm is used to guarantee the natural existence of multiple triplets of acoustic and optical modes

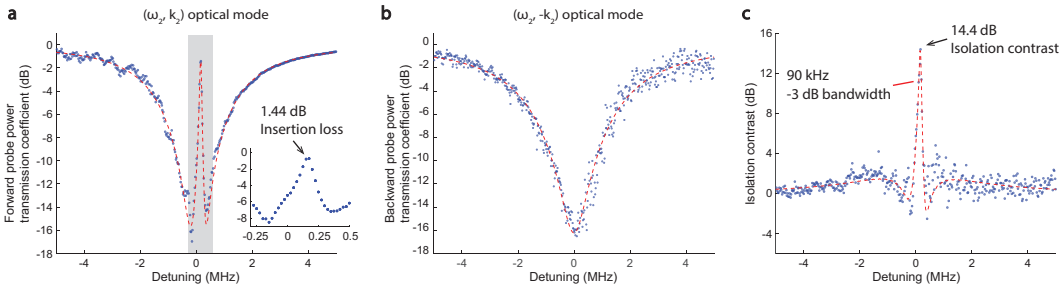

Figure 4.3: Experimental observation of extremely low insertion loss linear optical isolation. a. Probe power transmission coefficient $\left|\tilde{t}_p\right|^2$ is measured in the forward direction through the waveguide near the (ω_2, k_2) mode, with fixed 66 μW pump power dropped into the (ω_1, k_1) mode. The forward probe power transmission coefficient through the waveguide shows only 1.44 dB insertion loss within the transparency. The phonon mode frequency is 145 MHz. **b.** The (ω_2, -k_2) optical mode measured by the backward probe does not exhibit the induced transparency, resulting in conventional absorption of the probe signal by the resonator. **c.** The optical isolation contrast is evaluated as the difference between forward and backward power transmission coefficients. Here we calculate 14.4 dB peak contrast with a -3 dB bandwidth of 90 kHz. Isolation exists over 470 kHz.

that satisfy the phase-matching condition for BSIT.

The requisite BSIT phase-matching is first experimentally verified by strongly driving the (ω_2, k_2) optical mode and observing spontaneous and stimulated Stokes Brillouin scattering into the lower mode (ω_1, k_1) in the forward direction [21]. Subsequently, we drive the (ω_1, k_1) optical mode with a strong control laser (<1 mW) and use a weak co-propagating probe laser to measure the power transmission spectrum across the high frequency optical mode (ω_2, k_2) revealing the induced transparency window. The control laser detuning and power are adjusted in order to maximize the power transmission within the transparency peak. Experimental measurements of the probe power transmission $\left|\tilde{t}_p\right|^2$ in both forward and backward directions are presented in Fig. 4.3. To show optical isolation, the same measurement is taken in the forward and backward directions while the constant control driving field $s_{1,\mathrm{in}}$ is supplied in the forward direction only. In this experiment the two selected optical modes of the resonator have linewidth $\kappa_1 \approx \kappa_2 \approx 4.1$ MHz, and are spaced approximately 145 MHz apart. They are coupled by means of a 145 MHz acoustic mode of intrinsic linewidth $\Gamma_\mathrm{B} \approx 12$ kHz. Through finite element simulations, we estimate that the acoustic mode corresponds to a first order Rayleigh surface acoustic exicitation having an azimuthal order of M=24. At a diameter of 170 μm, this translates to an acoustic momentum of $q = 0.28\ \mu m^{-1}$ and ensures breaking of interaction

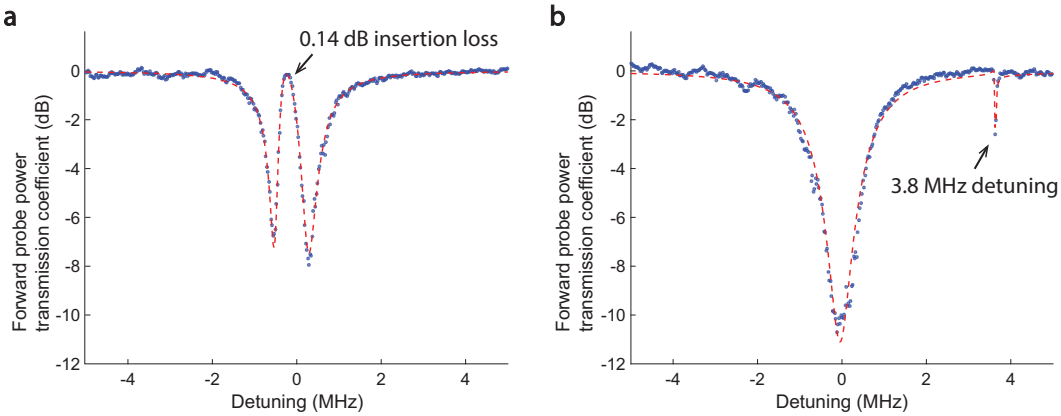

Figure 4.4: Demonstration of ultra-low forward insertion loss with stronger coupling G. a. Here, we use a triplet of optical and acoustic modes with an optical mode separation or acoustic frequency of 164.8 MHz. Pump-enhanced Brillouin coupling rate G is much higher due to better acousto-optic modal overlap and 235 μW power absorbed into the control mode. This results in $G \approx \kappa/3$ causing the forward insertion loss within the transparency to decrease to only 0.14 dB. The isolation bandwidth also increases to approximately 400 kHz. **b.** The transparency-free (ω_2, k_2) optical mode is observable by detuning the control laser from the (ω_1, k_1) optical mode, which also detunes the scattered light.

symmetry for co-propagating and counter-propagating probe fields (Fig. 4.2a).

As seen in Fig. 4.3a the system exhibits very low forward insertion loss (1.44 dB) at the peak of induced transparency region for 66 μW control laser power absorbed to the resonator (power launched in fiber is 680 μW). This corresponds to an experimentally calculated pump-enhanced Brillouin coupling of $G \approx \kappa_2/12$. At this point, the acoustic mode has an effective linewidth of 80.4 kHz due to Brillouin cooling [68]. Simultaneous measurement of backward probe power transmission (Fig. 4.3b) shows only the absorption spectrum of the unperturbed (ω_2, -k_2) optical mode, generating a power transmission loss of 15.8 dB in the waveguide. Subtraction of the forward and backward measurements provides a measure of the optical isolation contrast, which is 14.4 dB here with ~90 kHz full width at half maximum (Fig. 4.3c).

Since the forward insertion loss is very low (zero in the ideal theoretical case), the isolation contrast is primarily determined by the proximity of the waveguide-resonator coupling to the critical coupling condition, which if achieved would yield infinite isolation contrast. Achieving critical coupling $\kappa_{ex} = \kappa_{2,o}$ in non-integrated

waveguide-microsphere systems is very challenging due to multimode waveguiding in the taper, thermal drifts during the experiment, and vibrational or mechanical stability issues. Previously, up to 26 dB of signal extinction has been experimentally demonstrated in a fiber taper-microsphere system [54]. In the future, ideal isolation may be approached if the waveguide and resonator are integrated on-chip, since most mechanical issues can be eliminated and the interacting modes can be designed precisely. Alternatively, applications that require high contrast may employ multiple isolators in series with minimal penalty due to the extremely low insertion loss in this system. It is thus appropriate to compare performance of different isolators by referencing the achieved contrast to 1 dB forward loss. The data shown in Fig. 4.3 indicates this figure of merit of approximately 10 $\mathrm{dB_{isolation}/dB_{loss}}$ (units preserved for clarity, indicating 14.4 dB constrast vs 1.44 dB forward loss).

Theory indicates that much lower forward insertion loss can be obtained if much higher coupling rate G is arranged, either by lowering the loss rates of the optical modes, or by using higher control laser power. Fortunately, a special feature of two-mode systems such as BSIT [28] is the resonant enhancement of the intracavity pump photons in mode ω_1, which enables much easier access to the strong coupling regime. Nonreciprocity based on single-mode OMIT [114] does not possess this feature and it is thus impractical to expand the isolation bandwidth and reach the ultra-low loss regime. Making use of this resonant enhancement, in Fig. 4.4a we show a system nearly reaching the strong coupling regime with $G \approx \kappa/3$, exhibiting only 0.14 dB forward insertion loss (96.8% transmission) and isolation contrast estimated at 11 dB. Here, 235 μW control power is coupled to the resonator (700 μW launched in fiber). The unmodified optical mode absorption can be easily observed by detuning the control laser such that the interference is generated outside the optical mode (Fig. 4.4b). This result indicates that the strong coupling regime is also within the reach of this silica waveguide-resonator system [28]. The isolation figure of merit (referenced to 1 dB insertion loss) for the Fig. 4.4 result is quantified at 78.6 $\mathrm{dB_{isolation}/dB_{loss}}$. This compares extremely well to commercial fiber-optic Faraday isolators whose figures of merit typically range between 60 - 100 $\mathrm{dB_{isolation}/dB_{loss}}$, and far exceeds the capabilities demonstrated till date by any other non-magnetic microscale optical isolation approach.

Chapter 5

Suppression of disorder-induced scattering of phonons

The transport of sound and heat, in the form of phonons, can be limited by disorder-induced scattering. In electronic and optical settings the introduction of chiral transport, in which carrier propagation exhibits parity (or direction) asymmetry, can remove elastic backscattering and provides robustness against disorder. However, suppression of disorder-induced scattering has never been demonstrated in non-topological phononic systems. Specifically, disorder in a WGM resonator can induce coupling of forward (clockwise) and backward (counter-clockwise) propagating degenerate phonon modes. As a result, the two phonon modes loss their directionality and there no longer remains a distinguisable chirality in the mechanics. In other words, phonons that are launched in the clockwise direction can spontaneously invert their directionality to counterclockwise. In this chapter, I discuss a path for achieving robust phonon transport in the presence of material disorder, by explicitly inducing chirality through parity-selective optomechanical coupling.

We first discuss the parity-selective nature of Brillouin cooling [68]. As discussed in Chapter 4, Brillouin cooling process must also be selective to phonon directionality due to the phase-matching condition. In other words, forward optical pumping only acts to cool forward propagating phonons. I show that asymmetric optical pumping of a symmetric resonator enables a dramatic chiral optomechanical cooling of clockwise and counterclockwise phonons, while simultaneously suppressing the hidden action of disorder. Most importantly, this passive mechanism is also accompanied by a chiral reduction in heat load leading to optical cooling of the mechanics without added damping, an effect that has no optical analog. This technique can potentially improve upon the fundamental thermal limits of resonant mechanical sensors, which cannot be attained through sideband cooling.

5.1 Parity-selective Brillouin cooling by unidirectional pumping

5.1.1 Introduction

[1] The cooling of nanomechanical resonators is important for exploring the quantum behavior of mesoscale systems, high precision metrology [117, 118, 119], and quantum computing [120, 121]. Developments in laser cooling of mechanical modes by active feedback [122], bolometric effects [123], and ponderomotive forces [124, 125, 126, 127, 128] have enabled access to the mechanical ground state [129, 130] and the exploration of quantum mechanical effects [131]. The cooling rate achievable by such optomechanical mechanisms depends on the optical density of states (DoS) available for light-scattering and also increases with the intensity of the cooling laser. Resonant enhancement of the pump, for instance through two-mode optomechanics, can thus increase the cooling rate by enhancing the number of intracavity photons. 'Membrane in the middle devices' [132, 133, 134] are a key example of two-mode systems where this enhancement of cooling has been demonstrated. Another major example are Brillouin optomechanical devices in which two optical modes are coupled through a traveling acoustic wave mode. Experimental efforts on Brillouin systems have shown phonon lasing [135, 21], cooling [68], and induced transparency [18], but the role of the dual DoS has not been explored. In this study, we experimentally validate the role of the dual optical DoS in Brillouin cooling, and reveal the unique technical constraints that can arise from the enforced phase-matching relationship and the thermal locking effect in high-finesse resonators [136]. Using this, we demonstrate a room-temperature system showcasing cooling near the saturation regime using only a few hundred microwatts of input power.

Let us consider a general optomechanical system having two optical modes; the lower mode ω_1 hosts the resonantly enhanced pump laser, while the higher mode ω_2 hosts anti-Stokes scattered light. These two optical modes are coupled by a phonon mode of frequency Ω_B with the relation $\Omega_B \approx \omega_2 - \omega_1$. There are now two possibilities for the momentum associated with this phonon mode. In conventional optomechanical cooling the resonator supports standing-wave phonons, such as in a breathing mode, having zero momentum $q_B = 0$. Alternatively, a whispering

[1] Portions of this chapter are reprinted with permission from Kim, S., and Bahl, G. (2016), "Role of optical density of states in Brillouin optomechanical cooling," Optics Express, 25, 2, p.776 - 784.

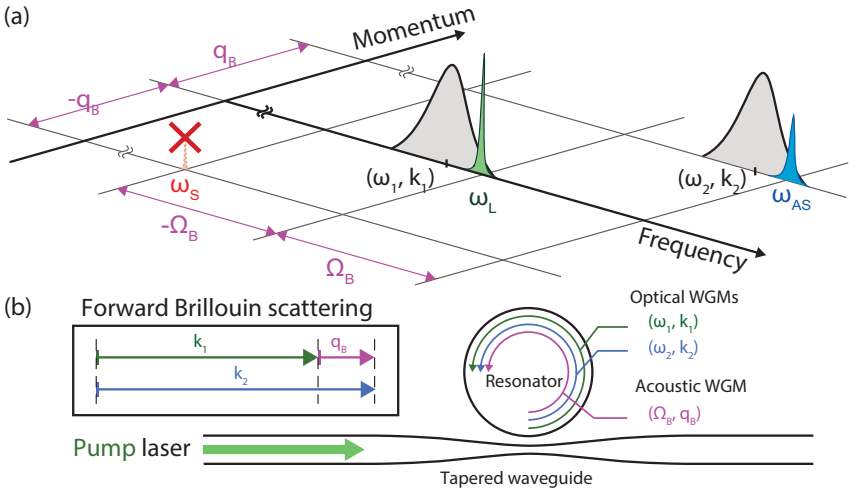

Figure 5.1: (a) Generalized modal arrangement required for dynamical back-action cooling of a (Ω_B, q_B) phonon mode in a resonator supporting two optical modes (ω_1, k_1) and (ω_2, k_2). Here ω_L and $\omega_{AS}(\omega_S)$ denote the frequencies of pump laser and the anti-Stokes (Stokes) scattered light. (b) Our experiments are performed in a whispering gallery microresonator that is optically coupled using a tapered fiber waveguide. Optomechanical cooling of an acoustic whispering gallery mode (WGM) having nonzero momentum $q_B \neq 0$ is achieved by means of forward Brillouin scattering.

gallery resonator may support a traveling wave phonon mode with non-zero momentum $q_B \neq 0$ as found in Brillouin scattering interactions. For phase matching either process, momentum conservation $k_1 + q_B = k_2$ is necessary, which we illustrate in general in Fig. 5.1. When the phase matching condition is satisfied, resonant pump light can scatter into the anti-Stokes optical mode (ω_2, k_2) while annihilating phonons from the system. Stokes scattering is simultaneously suppressed since no suitable optical mode is available. This leads to the insight that the resolved sideband regime could also be achieved in momentum space, even if the optical modes are not resolved in frequency space, enabling cooling with high fidelity selection of only anti-Stokes scattering.

The existence of two-mode systems with $q_B \neq 0$ phonon modes was experimentally verified recently [21]. Optomechanical cooling in these systems has been experimentally demonstrated [68] and also theoretically analyzed [137, 48]. However, the expected role of optical DoS in the cooling process has not been experimentally investigated. In this work, we study the dependence of cooling rate on both pump and anti-Stokes optical DoS using the Brillouin opto-acoustic cooling system [68] in a silica whispering gallery resonator. We analyze the role of thermal locking [136]

and also discuss through experiment the potential of reaching the strong coupling regime.

5.1.2 Experimental methods

Our experiments are performed in a whispering gallery resonator of optical Q $> 10^8$ with a diameter of about 150 μm as shown in schematics Fig. 5.1(b) and Fig. 5.2(a). This device hosts two optical modes (ω_1, k_1) and (ω_2, k_2) that are phase-matched by a traveling phonon mode (Ω_B, q_B). The configuration of the optical modes is shown in $\omega - k$ space in Fig. 5.1(a). The resonator modes in consideration have loss rates $\kappa_1/2\pi = 1.6$ MHz and $\kappa_2/2\pi = 1.5$ MHz, while the phonon mode is at $\Omega_B/2\pi = 260.9$ MHz with loss rate $\Gamma_B/2\pi = 31.3$ kHz, placing the system in the resolved sideband regime ($\Omega_B \gg \kappa_1, \kappa_2$). A tunable external cavity diode laser (ECDL) pumps the system near 1555 nm with 1.1 mW launched in the waveguide. Light is coupled to the resonator via tapered optical fiber with external coupling rate κ_{ex} to the resonator optical modes. The pump is tuned to the (ω_1, k_1) mode while spontaneous anti-Stokes scattering occurs to the (ω_2, k_2) mode. As shown in Fig. 5.1(a), Stokes scattering is suppressed since no suitable optical mode is available. Forward scattered optical power from the resonator couples out via the tapered fiber and can be measured on a forward photodetector; low-frequency transmission measurement shows the optical modes, while high-frequency measurement provides the frequency offset between pump and spontaneously scattered light. An electro-optic modulator (EOM) is used to generate a probe sideband, using which a network analyzer can monitor the detuning $\Delta_2 = (\omega_L + \Omega_B) - \omega_2$ between the scattered light and the (ω_2, k_2) mode by means of Brillouin scattering induced transparency (BSIT) [18]. This induced transparency is illustrated in the network analyzer inset of Fig. 5.2(a).

The spectrum of the photocurrent $S_{II}(\omega)$ generated by pump and scattered light that appears on the forward detector is related to the symmetrized spectral density of the phonon mode $\overline{S_{bb}}(\omega)$ [129, 138] via the relation

$$S_{II}(\omega) = N + \left(\frac{8\kappa_{\text{ex}} |g_0|^2 \bar{n}_{\text{cav}}}{\kappa_2^2 + 4\Delta_2^2} \right) \overline{S_{bb}}(\omega) \tag{5.1}$$

where the parameter g_0 is the optomechanical single-photon coupling strength, $\bar{n}_{\text{cav}}$ is intracavity pump photon number in the (ω_1, k_1) mode, and N is the background

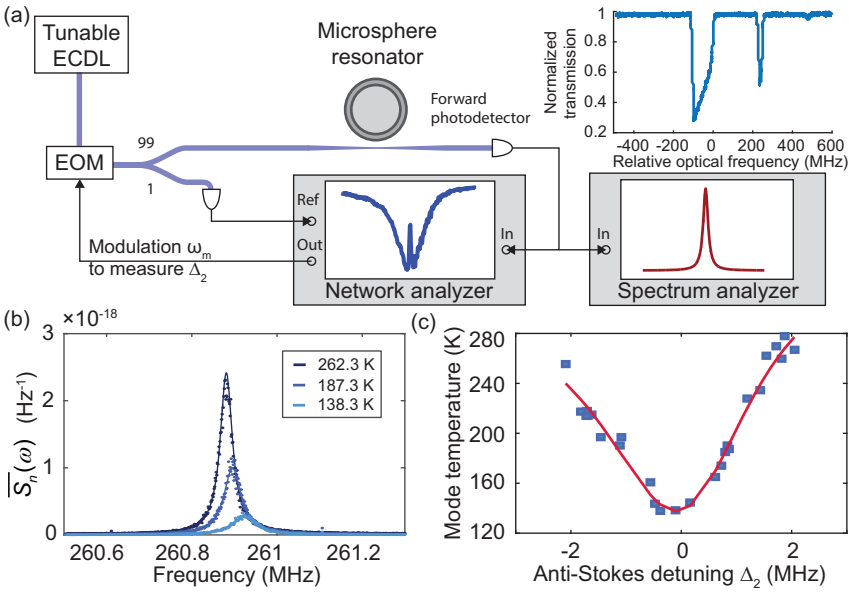

Figure 5.2: (a) Experimental setup used for investigating role of optical DoS in Brillouin cooling. Top-right inset shows fiber-transmission measurement of the two optical modes (ω_1, k_1) and (ω_2, k_2) during a laser sweep. (b) The normalized phonon spectrum $\overline{S_n}(\omega)$ exhibits a cooling trend with increasing the pump laser. The small shift in mechanical resonance frequency occurs due to the optical spring effect [126, 48]. Solid lines are Lorentzian fits to the data. (c) The mode temperature T_{eff} is presented as a function of Δ_2. It shows that the cooled mode temperature does not follow a symmetric Lorentzian-type curve, which is indicative that the pump optical density of states also affects the cooling.

noise floor (See the detailed discussion in Section 3.4). Thus, the measured RF spectrum S_{II} is a direct representation of the phonon mode spectrum $\overline{S_{bb}}(\omega)$ and is scaled according to the experimental parameters. To remove the dependence of this spectrum on the number of intracavity photons in the resonator $\bar{n}_{\text{cav}}$ and the anti-Stokes field detuning Δ_2, we perform a normalization to obtain $\overline{S_n}(\omega) = \frac{(\kappa_2^2+4\Delta_2^2)}{4\kappa_{\text{ex}}|g_0|^2\bar{n}_{\text{cav}}} S_{II}(\omega)$ [Fig. 5.2(b)]. This $\overline{S_n}(\omega)$ is then proportional to $\overline{S_{bb}}(\omega)$ but with an additional background noise floor. We can then quantify the effective temperature T_{eff} of the phonon mode by fitting its spectral linewidth Γ_e, and using the relation $T_{\text{eff}} = (\Gamma_B/\Gamma_e)\, T_b$, where T_b is the mechanical bath temperature (room temperature) and Γ_B is the intrinsic linewidth of the phonon mode [126]. We note that $\Gamma_e = \Gamma_B + \Gamma_{\text{opt}}$ where Γ_{opt} is the optomechanical damping rate. The linewidth-temperature relation is derived from the equipartition theorem $k_B T_{\text{eff}} = \int_{-\infty}^{\infty} m_e \omega_o^2 \overline{S_{bb}}(\omega) d\omega$ [123].

Since the pump and anti-Stokes optical fields have a well defined frequency offset Ω_B, the detuning of the anti-Stokes field from the cavity resonance Δ_2 can

be simply modified by tuning the frequency of the pump. Figure 5.2(c) shows the measured effective temperature of the phonon mode T_{eff} as a function of Δ_2. As we reduce Δ_2 from 2 MHz to 0 MHz, the mode reaches a final effective temperature of $T_{\text{eff}} \sim 138.3$ K starting from 290 K. As anticipated, the effective temperature rises again to 255 K as we continue detuning to -2 MHz since the anti-Stokes optical density of states (DoS) modifies the scattering efficiency. The defining cooling curve in Fig. 5.2(c) does not follow a symmetric Lorentzian shape, since the pump detuning Δ_1 is simultaneously modified in this experiment. This result shows a clear evidence of the dependence of the Brillouin cooling effect on the optical DoS of both the pump and the anti-Stokes optical modes. The measurable mechanical frequency $\Omega_B/2\pi$ simultaneously tunes from 260.87 MHz to 260.96 MHz through the associated optical spring effect, as a function of detuning [139].

5.1.3 Optomechanical damping with dual optical DoS

Let us now evaluate the characteristics of the phonon mode spectrum $\overline{S_{bb}}(\omega)$ under the influence of the cooling laser. The Hamiltonian formulation for such optomechanical systems with two optical modes has been presented previously [137, 48]. The resulting quantum Langevin equations enable derivation of the optomechanical damping rate Γ_{opt} as follows:

$$\Gamma_{\text{opt}} = \frac{4\kappa_2 |g_0|^2 \bar{n}_{\text{cav}}}{\kappa_2^2 + 4\Delta_2^2} \quad \text{where} \quad \bar{n}_{\text{cav}} = \frac{4\kappa_{\text{ex}} |\alpha_{\text{in}}|^2}{\kappa_1^2 + 4\Delta_1^2} \tag{5.2}$$

and where the pump detuning is $\Delta_1 = \omega_L - \omega_1$. Here $|\alpha_{\text{in}}|^2$ is the rate of pump photons arriving at the cavity from the waveguide. Clearly, both the pump and anti-Stokes detunings, Δ_1 and Δ_2 affect the optical damping. The optomechanical damping rate Γ_{opt} given in Eq. (5.2) leads us to envision a cooling scenario described in Fig. 5.3(c), where the cooling rate is dependent on detuning of the two optical signals to their respective modes ($\Delta_1,\ \Delta_2$). A Lorentzian cooling response is thus expected on both independent detuning axes. However, we know that the detuning parameters Δ_1 and Δ_2 are not independent, since the optical mode spacing and the phonon mode frequency are well determined. This is illustrated in Fig. 5.3(a) where the pump signal ω_L and anti-Stokes light ω_{AS} scan through the modes together since they must remain equidistant (the separation is defined by Ω_B).

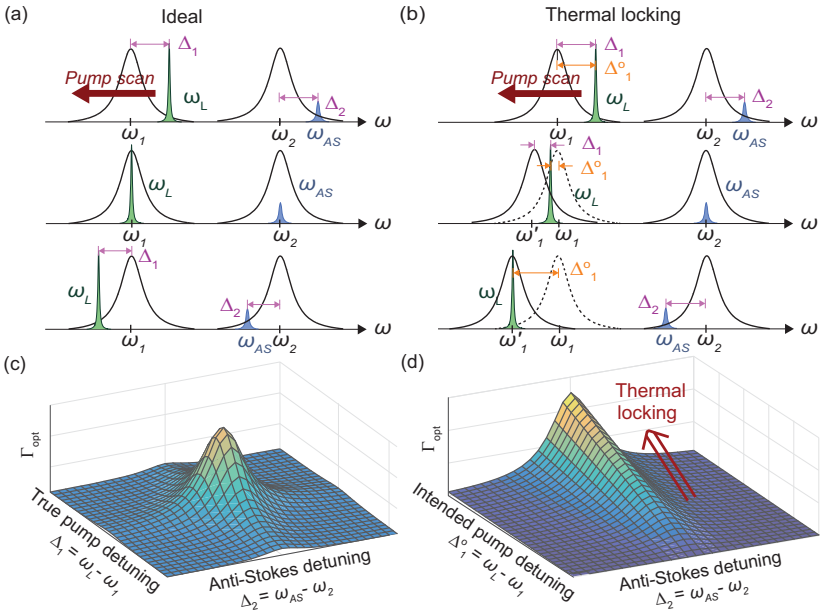

Figure 5.3: Role of two optical DoS on optomechanical damping rate Γ_{opt}. (a) Ideally, the pump (ω_L) and anti-Stokes (ω_{AS}) detuning track together due to the fixed acoustic mode frequency. (b) Practically, thermal locking of the pump to its host optical mode causes the true anti-Stokes detuning to vary faster than the true pump detuning. Δ_1^{o} is the intended detuning while Δ_1 is the true detuning. (c) Equation 5.2 predicts that Γ_{opt} is a Lorentzian function with respect to either of the true detunings Δ_1 and Δ_2. (d) Thermal locking of the pump to the ω_1 mode causes Δ_1 to no longer track the intended detuning Δ_1^{o}, resulting in a skewed cooling rate.

5.1.4 Effect of thermal locking

In reality, however, ultra-high-Q resonators do exhibit significant thermal tuning in response to pumping even in the sub-milliwatt regime. This primarily takes the form of locking of the resonator mode to the pump laser [136], and is illustrated in Fig. 5.3(b). The result is that the intended pump detuning $\Delta_1^{\text{o}} = \omega_L - \omega_1$, i.e. the detuning from the original pump resonance (ω_1, k_1), does not generate a Lorentzian shaped cooling rate but instead traces out a skewed response Fig. 5.3(d). Experiments where measurable Brillouin cooling is to be observed require pump power in the > 10 microwatt regime, and fall under this latter category. Figure 5.3(c) and 5.3(d) does oversimplify the situation to some degree, since the anti-Stokes mode also experiences thermal tuning due to heating of the resonator. However, this thermal red shift is generally smaller than the red shift experienced by the pump mode due to the distinct spatial mode profiles. As a result, the true pump

detuning $\Delta_1 = \omega_L - \omega_1'$ for the locked mode at ω_1' is always lower than the intended detuning $\Delta_1^o = \omega_L - \omega_1$. This technical challenge to optomechanical cooling has not been reported previously since it is not important in resolved sideband one-mode systems, but uniquely impacts two-mode systems having high finesse.

5.1.5 Verification of DoS dependence

Figure 5.4(a) shows the experimentally measured dependence of the optomechanical damping rate Γ_{opt} on the true pump detuning Δ_1 and the anti-Stokes detuning Δ_2. To relate the measurement to Eq. (5.2), several experimental parameters are required. The intracavity photon number $\bar{n}_{\text{cav}}$ and the true pump detuning Δ_1 can be inferred by measuring the power absorbed from the waveguide by the resonator. Specifically, $\Delta_1 = \sqrt{\frac{\kappa_1\kappa_{\text{ex}}}{4}\left(\frac{P_{\text{wg}}}{P_{\text{in}}} - \frac{\kappa_1}{\kappa_{\text{ex}}}\right)}$ where P_{wg} is the optical power in the waveguide and P_{in} is the optical power absorbed by the resonator. As mentioned above, the detuning Δ_2 can be directly measured using BSIT [18]. We can then predict the cooling rate Γ_{opt} based on Eq. (5.2) with all measurable parameters being known, except $g_0/2\pi = 2.6$ Hz which is extracted by fitting to the BSIT model. This prediction leads to the 3d surface shown in Fig. 5.4(a) and is in very good agreement with the experiment. Since both pump and anti-Stokes detuning change together [see Figs. 5.3(a) and 5.3(b)], the results are not dependent only on one optical DoS, but are affected by both simultaneously. As predicted, the true pump detuning varies far less than the anti-Stokes detuning due to thermal locking of the pump optical mode. Importantly, the highest optomechanical damping rate is much more strongly dependent on the detuning of the anti-Stokes mode than on the detuning of the pump mode. Attainment of the global optimum point where both pump and anti-Stokes detuning are zero is thus non-trivial and requires compensatory action to adjust the temperature of both modes in a synchronized manner. An example technique may be the use of a second thermal-tuning laser that adjusts the anti-Stokes mode family.

We can now attempt to independently characterize the role of the optical DoS of either optical mode. This can be achieved by describing a normalized cooling rate $\zeta_1 = \Gamma_{\text{opt}}/\bar{n}_{\text{cav}}$ which is independent of the intracavity photon number $\bar{n}_{\text{cav}}$ and Δ_1, and a normalized cooling rate $\zeta_2 = \Gamma_{\text{opt}}(\kappa_2^2 + 4\Delta_2^2)$ which is independent of the anti-Stokes detuning Δ_2. In addition, we define the dimensionless numbers $\eta_1 \triangleq \zeta_1/\zeta_{1.\text{max}}$ and $\eta_2 \triangleq \zeta_2/\zeta_{2.\text{max}}$ where $\zeta_{1.\text{max}}$ and $\zeta_{2.\text{max}}$ are the maximum value of ζ_1 and ζ_2 at

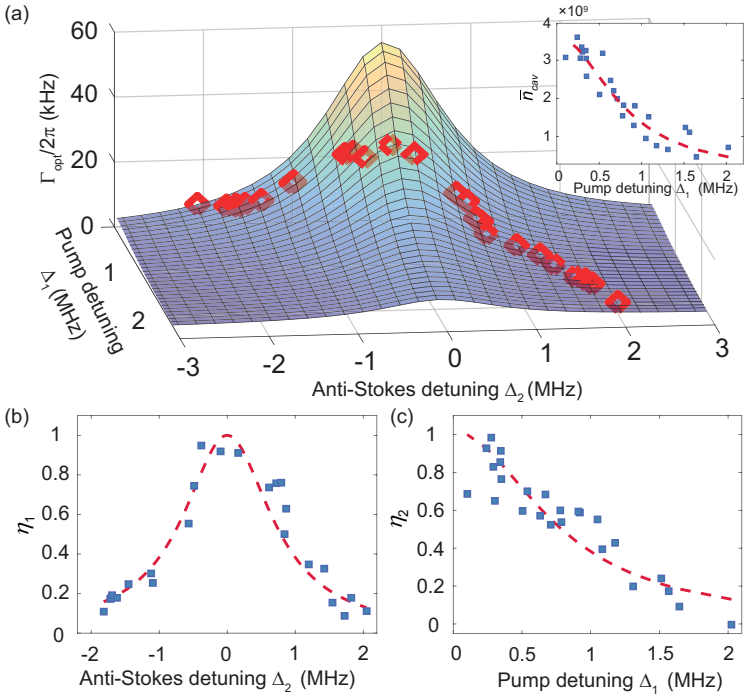

Figure 5.4: (a) Data points (diamonds) are the measured optomechanical damping rate $\Gamma_{\rm opt}$ a function of pump and anti-Stokes detuning Δ_1 and Δ_2. The 3d surface is the predicted result based on Eq. (5.2), using the optomechanical single-photon coupling strength $g_0/2\pi = 2.6$ Hz. The inset shows the intracavity photon number $\bar{n}_{\rm cav}$ with respect to Δ_1, as deduced from Eq. (5.2). (b) Dependence of η_1 and (c) η_2 (see text) on anti-Stokes detuning Δ_2 and pump detuning Δ_1, respectively. Red dashed lines are derived from Eq. (5.2).

resonances, i.e. at $\Delta_2 = 0$ and $\Delta_1 = 0$ respectively. In this particular experiment, the measurable values of $\zeta_{1.\rm max}$ and $\zeta_{2.\rm max}$ are 1.66×10^{-5} Hz and 1.55×10^{17} Hz^3, respectively. These values, along with the 2d data plots in Figs. 5.4(b) and 5.4(c) and previously mentioned parameters of the system, enable full reconstruction of the 3d data in Fig. 5.4(a). In Fig. 5.4(b) we see that the normalized measurement η_1 exhibits clear Lorentzian dependence on the anti-Stokes detuning Δ_2. This result is similar to what is expected from resolved-sideband optomechanical cooling [128]. Additionally, since we know the dependence of the intracavity photon number $\bar{n}_{\rm cav}$ on pump detuning Δ_1, we are able to plot [in Fig. 5.4(c)] the normalized measurement η_2 against the pump detuning Δ_1 directly, without being affected by the anti-Stokes mode detuning. There is thus a clear contribution of the DoS in both optical modes on the resulting phonon dissipation rate.

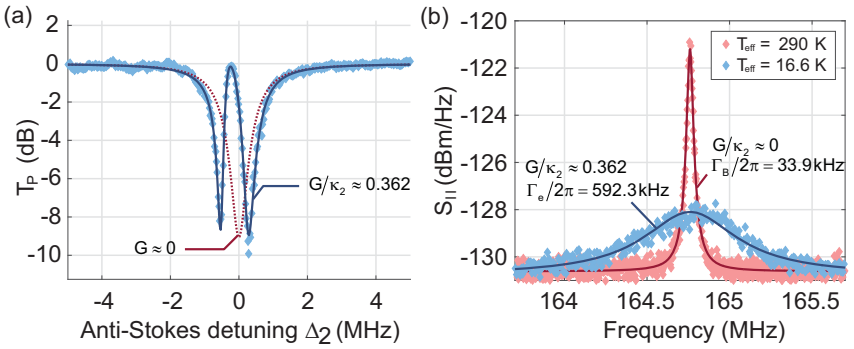

Figure 5.5: (a) Transmission of a probe laser tuned the anti-Stokes optical mode (ω_2, k_2) is measured through the optical waveguide, while a fixed pump laser is tuned on the lower (ω_1, k_1) optical mode. The red line shows optical absorption without optomechanical coupling ($G \approx 0$). For $G \neq 0$, induced transparency appears in the (ω_2, k_2) mode due to destructive interference mediated by phonons [18]. Blue markers show experimental data and blue-bold line is the fit to theory. (b) The mechanical noise spectrum is measured for $\Omega_B/2\pi = 164.8$ MHz, for $G/\kappa_2 \approx 0$ and $G/\kappa_2 \approx 0.362$.

5.1.6 Saturation and strong coupling regimes

A special feature of two-mode optomechanical cooling systems is that the pump laser is resonant in the optical mode (ω_1, k_1). These systems can thus support a very large amount of intracavity photons ($\bar{n}_{\text{cav}} > 10^9$) compared to what is achievable in single-mode optomechanics [128, 129, 127]. As a result, the ratio of the light-enhanced optomechanical coupling strength $G = g_0\sqrt{\bar{n}_{\text{cav}}}$ to the optical loss rate κ_2 can be increased significantly, implying that two-mode systems could potentially reach the strong coupling regime where the loaded optomechanical coupling exceeds the optical linewidth ($G \geq \{\kappa_2, \Gamma_B\}$), even at room temperature. Additionally, the saturation limit where optomechanical damping rate is constrained by the optical loss rate (i.e. $\Gamma_{\text{opt,max}} = \kappa_2$) can be reached when cooperativity exceeds κ_2/Γ_B [87, 140, 141]. To explore this possibility, we arrange a system that has optical loss rates $\kappa_1/2\pi \approx \kappa_2/2\pi = 1.1$ MHz and acoustic loss rate $\Gamma_B/2\pi = 33.9$ kHz with mechanical frequency $\Omega_B/2\pi = 164.8$ MHz. Due to the optomechanical coupling, we anticipate the appearance of induced transparency in the anti-Stokes mode (ω_2, k_2) [18], which evolves into a mode splitting effect under strong coupling. Figure 5.5(a) shows an experimental observation of this induced mode splitting that is generated due to the large circulating pump power ($\bar{n}_{\text{cav}} = 5 \times 10^9$) in the system. By fitting this observation to a mathematical model (Supplement of [18]) we can obtain $G/\kappa_2 \approx$

0.362, which is very close to the strong coupling regime. The observed linewidth of the phonon mode is shown in Fig. 5.5(b), both before and after cooling. We see that the effective linewidth broadens to $\Gamma_e/2\pi = 592.3$ kHz which is comparable to the optical loss rate of the anti-Stokes mode $\kappa_2/2\pi = 1.1$ MHz. This result corresponds to a final mode temperature of 16.6 K. The cooling rate is expected to saturate at the optical loss rate κ_2 when the system reaches the strong coupling regime. Here, the measured effective mode temperature is very close to the estimated saturation temperature of 8.9 K.

5.1.7 Conclusions

We have provided direct experimental verification that Brillouin cooling is dependent on two optical DoS, of both pump and anti-Stokes optical resonances. Additionally, we demonstrated that thermal locking of the pump laser causes the optomechanical damping rate Γ_{opt} to be asymmetric with respect to the laser detuning. This is a unique technical challenge that can arise in Brillouin optomechanical cooling systems having high optical finesse. In spite of thermal locking, we show the effects of the pump and anti-Stokes optical DoS can be individually de-convolved. Finally, we experimentally confirm that resonant enhancement of the pump in a Brillouin optomechanical cooling system enhances the cooling rate significantly. Our room temperature experimental results show that the strong coupling regime is well within reach, and may also pave the way to exploration of the saturation regime and beyond-saturation cooling techniques [142].

5.2 Dynamically induced robust phonon transport an chiral cooling in an optomechanical system

5.2.1 Introduction

[2] The modes of idealized whispering gallery resonators have two possible parities (also known as chiralities) corresponding to clockwise or counter-clockwise circulation. This is true for both phonons and photons. However, many other resonator

[2]Portions of this chapter are reprinted with permission from Kim, S., et. al., (2017), "Dynamically induced robust phonon transport and chiral cooling in an optomechanical system," Nature Communications, 8, 205.

types, e.g. Fabry-Perot resonators, do not have such distinguishable chiral modes. Efforts to harness the optical and mechanical properties of such achiral resonators are leading to new approaches for quantum noise limited sources [36, 143, 144], preparation of quantum states of matter [125, 124, 145, 146], and ultra-high precision metrology [147, 148, 149, 150]. Since all these efforts are aided by long coherence times for resonant excitations, they are fundamentally limited by structural disorder, even in systems with high symmetry, and by thermal noise in the mechanics. While optomechanical sideband cooling can lower the effective temperature of a mechanical oscillator, it does not modify the heat load, and thus does not fundamentally modify the contribution of thermal noise for, e.g., sensing or transduction [149, 150]. Surprisingly, the chiral edge states of topological insulators – in which different parity excitations travel in different directions – can provide improved transport properties, giving rise to unique physics ranging from nonreciprocal wave propagation to disorder-free transport in quantum Hall systems [151, 17, 152, 153, 154]. At the same time, inducing nonreciprocal behavior by breaking parity-symmetry in achiral non-topological devices forms the basis for circulators [155, 156] and recent proposals for optomechanical isolation [152, 18, 19, 154]. However, experiments to date on nonreciprocal optomechanical devices [18, 19, 114] have focused entirely on optical behavior, and there has been no direct exploration on the chiral nature of propagating phonons in such systems, nor on the disorder tolerance induced through chirality.

While the phonon modes of many systems are chiral in nature, achirality can be introduced in the presence of disorder. For instance, backscattering from small defects can couple the two possible mode parities thereby removing the chiral property. Here we show how to optically impart chirality to achiral mechanical modes of a whispering gallery resonator. Our approach results in disorder-less transport of sound, simultaneously improving the isolation of phonon modes from their bath and lowering their heat load without added damping [157]. We use a particularly simple class of systems for examining chiral behavior: passive devices with degenerate forward- and backward-propagating modes, such as ring cavities and whispering-gallery resonators (WGRs). The modes of these structures can alternatively be described as opposite parity pairs having clockwise (+ or cw) and counter-clockwise (− or ccw) pseudo-spin of circulation [152]. Chiral here indicates pseudo-spin-dependent behavior in the system. Disorder breaks parity conservation in WGRs, preventing chiral behavior and leading to the additional loss of energy in high-

Q modes via pseudo-spin flips and scattering into bulk modes, both optically [6] and mechanically [7, 8]. Recent work has shown that asymmetric optical pumping of one pseudo-spin direction in WGRs explicitly introduces chiral behavior for photons with the assistance of even weak optomechanical coupling [18]. In this work, we demonstrate that this induced symmetry breaking in fact imparts parity-dependent behavior throughout the system, the chiral echoes of which are observable across its mechanical properties as the system develops robustness to parity-breaking disorder.

We observe three significant phononic chiral effects. First, cw and ccw phonons experience dramatic chiral optomechanical cooling. While this may be anticipated from past experiments on Brillouin optomechanical coupling with traveling phonons [68, 18], such chiral phonon propagation has never been experimentally reported. Second, the optomechanical damping selectively provided to cw phonons results in mitigation of the disorder-induced loss for phonons having the opposite (ccw) pseudo-spin – effectively a phononic analogue of the quantum Zeno effect. Finally, while the cw phonon modes experience conventional optomechanical cooling [125, 124, 158, 159, 145, 68], an isolated high-Q ccw mode simultaneously experiences a reduction in damping and a reduction in temperature. This result reveals a surprising form of optomechanical cooling that occurs through chiral refrigeration of the thermal bath composed of the (cw) bulk mechanical modes of the system.

5.2.2 Modal relationships in a whispering-gallery resonator

The cylindrical symmetry of the system means that the whispering-gallery modes (WGMs) take the functional form $f(r,z)e^{i(M\phi-\omega t)}$, where ω is the eigenfrequency and signed integer M describes the propagation momentum or azimuthal order on the angular spatial variable ϕ. The transverse mode profile is given by $f(r,z)$. We now introduce the specific mechanical and optical WGMs that participate in the experiment, and the nature of their interaction. Our structure hosts frequency-adjacent optical modes belonging to different families that may be populated with photons of either pseudo-spin (Fig. 5.6a), for a total of four optical modes in the experiment. Scattering between these optical modes is only permitted through acousto-optic coupling (Brillouin scattering) via propagating phonons that match their frequency and momentum difference [21], which is termed the phase matching requirement. Thus, photon modes having cw (ccw) pseudo-spin can only be coupled through scattering from co-propagating phonons having cw (ccw) pseudo-spin. In

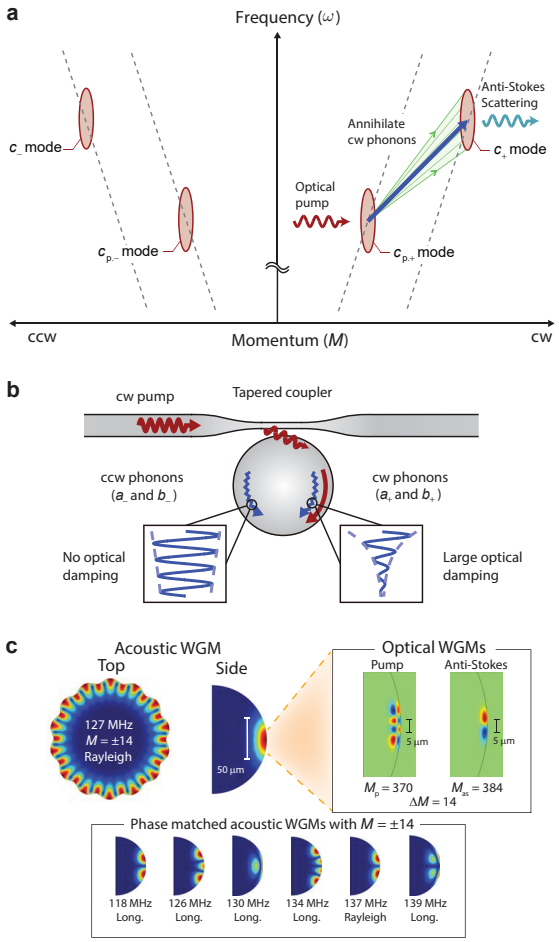

Figure 5.6: Chiral cooling and modal relationships in a whispering-gallery resonator. (a) Configuration of the two requisite optical whispering-gallery modes (WGMs) with cw (+) and ccw (−) degeneracy is illustrated in (ω, M) space. Integer M describes the azimuthal momentum of WGMs. Anti-Stokes Brillouin scattering from cw pumping of the lower mode annihilates only cw phonons of all phase-matched dispersion relations, while ccw phonons remain nominally unaffected, thus breaking parity symmetry in the system. The optical modes are illustrated elongated in ω-space due to the extremely large phase velocity of photons in comparison to phonons. **(b)** Directional optical interface to the resonator modes is achieved via tapered optical fiber. Unidirectional optical pumping results in dramatic chiral damping of the phonons. $a_\pm$ and $b_\pm$ phonon modes are described in Fig. 5.11. **(c)** Our experiment is performed using a high-Q $M = \pm 14$ acoustic WGM ($a_\pm$) using two optical WGMs having the same momentum separation. There also exist an extended group of acoustic bulk modes having the same M (representative members illustrated) that are also phase-matched but are not observable above the noise floor due to high mechanical damping and poorer frequency-matching. These are considered in our model collectively as a quasi-mode ($b_\pm$).

this situation when we pump the lower-energy optical mode, anti-Stokes scattering to the higher mode annihilates phonons [68] of matched parity, resulting in added optomechanical damping and cooling of the phonon mode. This system should thus exhibit significant optically-induced chirality in the transport of phonons that are phase matched for this interaction (Fig 5.6a,b). A large family of mechanical WGMs satisfy these phase matching requirements, of which a few representative members are illustrated in Fig. 5.6c. The lowest transverse-order Rayleigh phonon mode is most likely to be observable as it interacts least with the supporting stem of the microsphere, i.e. features the highest Q-factor, and thus generates the strongest scattering between the optical modes [21]. However, disorder induced scattering can couple this high-Q mode to the large population of lower-Q bulk modes of the resonator, as they have the same azimuthal order M but differ in extension into the bulk. Since the transverse optical mode profiles are much smaller than the transverse profiles of the mechanical modes (Fig 5.6c), the bare optical mode coupling to each of these many mechanical (physical) modes is of a similar order. Below, we collectively treat the remaining lower-Q bulk modes as a pair of phonon "quasi-modes" having large dissipation rate and fixed pseudo-spin. These quasi-modes act as a thermal bath for their parity-flipped high-Q mode, while also directly coupling to the light.

5.2.3 Experimental demonstration of chiral cooling

Our experiments are performed with a silica WGR of diameter $\sim 135\,\mu$m at room temperature and atmospheric pressure, using a tapered fiber coupler for optical interface at 1550 nm (Fig. 5.7a,b). The FWHM of both optical modes is approximately $\kappa = 5.1$ MHz, and the approximate simulated mode shapes are illustrated in Fig. 5.6c. Direct coupling between cw and ccw pseudo-spins, e.g. through optical Rayleigh scattering, is negligible for either optical mode in our experiment. The high-Q mechanical mode is also a whispering-gallery mode at 127 MHz with azimuthal order of $M = 14$ and mode shape illustrated in Fig. 5.6c. Verification of the Brillouin phase-matching between these modes can be performed by means of forward Brillouin lasing [21] and induced transparency measurements [18]. To examine the potential for modification of the high-Q phonon behavior, and the possibility of chiral transport of sound, we set up the experiment with two optical sources tuned to the lower optical mode in the clockwise (cw) and counter-clockwise

(ccw) directions. The role of the stronger cw "pump" is to induce cooling of the cw propagating phonons, while the role of the much weaker ccw "reverse probe" is to measure, via optical scattering, the counter-propagating phonon behavior. The RF beat spectrum generated between the scattered light and the corresponding source in either direction provides a direct measure of the phonon mode spectrum (Supplementary Note 4 in [23]), with sample measurements shown in Fig. 5.7c. In the experiment, the optical pump and probe sources are both derived from the same laser and are thus always at identical frequencies. Throughout the remainder of this work, no pump or probe field is delivered to the upper optical mode, in order to prevent coherent amplification of the phonons via Stokes Brillouin scattering.

Our first task is to measure the bare linewidth γ_m of the high-Q phonon mode without any optical pumping. We note that the bare linewidth (γ_m) of high-Q mechanical WGMs may be qualitatively distributed into two forms of loss: those that maintain parity, which we call intrinsic dissipation (γ), and those that break parity, leading primarily to radiative damping via low-Q bulk modes. Thus γ_m is traditionally the minimum measurable linewidth in any optomechanical sideband cooling experiment. We perform this measurement by detuning the source laser from the optical resonance such that little to no optomechanical cooling is induced by either the pump or the probe. For zero input power, the bare linewidth $\gamma_m = 12.5(\pm 1.0)$ kHz is estimated by fit-based extrapolation of measured cw and ccw phonon linewidths γ_{a+} and γ_{a-} using the theoretical model (Eqns. (5.7)). We also obtain the single phonon optomechanical coupling strength $h_0 \approx 14(\pm 2.5)$ Hz. All uncertainties in this manuscript correspond to 95 % confidence bounds of the fitted value.

The optomechanical cooling rate can be controlled by the detuning Δ_2 of the anti-Stokes scattered light from its optical mode, which we measure directly using the Brillouin Scattering Induced Transparency [18]. In Fig. 5.12a we plot measurements of both cw and ccw phonon linewidth as a function of this detuning. We immediately see a striking direction-dependence of the damping rates of the cw and ccw phonons, that has never previously been reported. This chiral damping of phonons is a direct result of the momentum conservation rules that underly the Brillouin scattering interaction, and will not generally be available in traditional single-mode optomechanical systems. We note also that the relative power of the cw pump and ccw probe lasers is $\sim 9:1$, so there is some sideband cooling of the

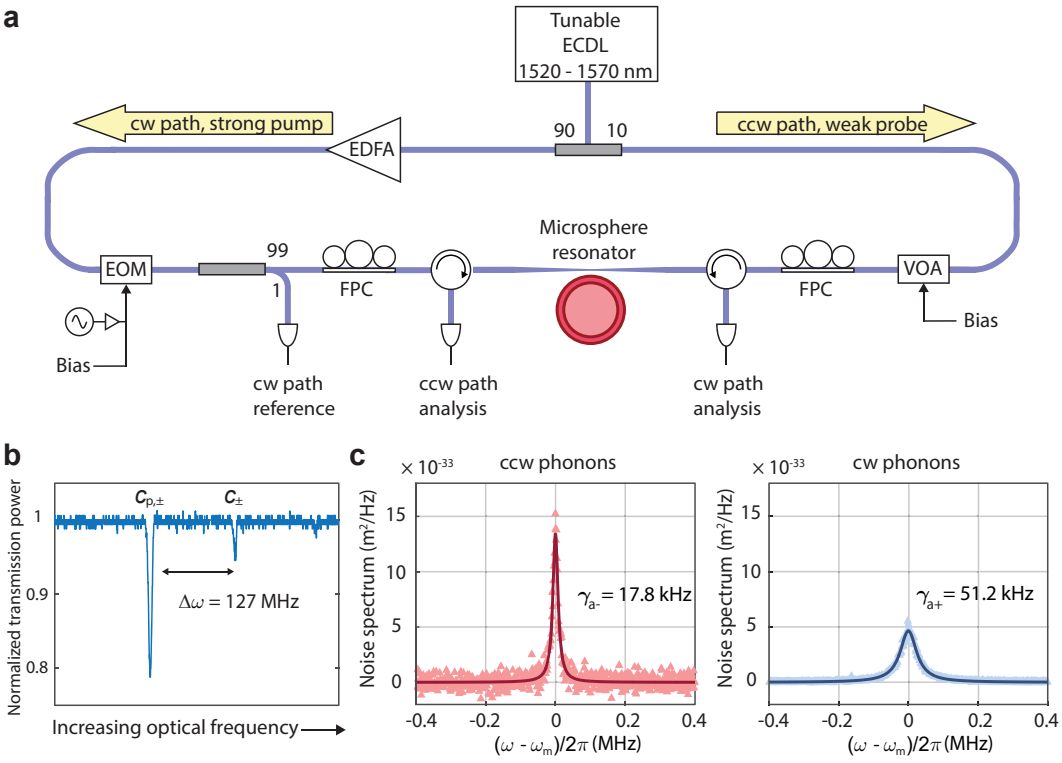

Figure 5.7: Measurement setup for chiral optomechanical refrigeration: (a) We perform the experiment using a silica whispering-gallery microsphere resonator that is interfaced via tapered optical fiber. A 1520 nm to 1570 nm tunable external cavity diode laser (ECDL) generates the asymmetric cw pump (strong) and ccw probe (weak) sources. An Erbium-doped fiber amplifier (EDFA) controls the cw pump power, for optomechanical cooling [68] and for monitoring the cw phonon spectrum. An electro optic modulator (EOM) is employed to measure detuning of anti-Stokes scattered light from its optical mode through via induced transparency [18]. A variable optical attenuator (VOA) is used to control the ccw probe. Fiber polarization controllers (FPC) are used to optimize coupling between the fiber and resonator in both directions. **(b)** The optical modes are mapped by measuring dropped power from the tapered fiber. **(c)** Dramatic chiral cooling of the high-Q ($\omega_m = 2\pi \times 127$ MHz) phonon populations is immediately observed with strong cw pumping (140.9 μW). ccw phonons are also cooled slightly due to the ccw probe. Solid lines are Lorentzian fits to the data.

a_- phonons as well.

5.2.4 System Model: Defining the Modes and Their Coupling

Before discussing the model for chiral cooling, we first elucidate physics behind in detail. Our system is composed of cw and ccw optical modes, high-Q phonon modes, as well as vibrational excitations inside the material, i.e. the phonon bath. As described in the main text, we focus on a scenario in which high-Q modes of clockwise and counterclockwise circulation with annihilation operators a_σ are coupled via disorder to a quasi-mode (broad mode representing many actual mechanical modes) circulating in the opposite direction with annihilation operators $b_{\bar{\sigma}}$. In the experiment, for each circulation we have a pair of optical modes $c_{p,\sigma}$ and c_σ. The optomechanical coupling allows for transfer of light from $c_{p,\sigma}$ to c_σ with a corresponding annihilation of a phonon that is phase matched. This process overlaps with both the high-Q modes and the quasi-modes.

With the above basic picture, we examine this model using the rotating wave approximation (RWA) as the experimental configuration is all narrowband. We can then use the input-operator language to describe the open system dynamics. After displacing the optical cavity fields by the pump amplitudes in the cavity, $c_\sigma \to \sqrt{n_\sigma} + c_\sigma$ with $\sqrt{n_+} = \alpha, \sqrt{n_-} = \beta$, the $c_{p,\sigma}$ fluctuations decouple from the rest of the system. Working in the frame rotating with the pump laser frequency, we write the linearized Heisenberg-Langevin equations for the mechanical and optical modes in the Fourier domain with Fourier frequency ω:

$$-i\omega c_\sigma = -i\Delta c_\sigma - \frac{\kappa}{2} c_\sigma + \sqrt{\kappa} c_\sigma^{\text{in}} - i\sqrt{n_\sigma}(g_0 b_\sigma + h_0 a_\sigma) \tag{5.3a}$$

$$-i\omega a_\sigma = -i\omega_m a_\sigma - \frac{\gamma}{2} a_\sigma + \sqrt{\gamma} a_\sigma^{\text{in}} - iV_0 b_{\bar{\sigma}} - ih_0\sqrt{n_\sigma} c_\sigma \tag{5.3b}$$

$$-i\omega b_\sigma = -i\omega_b b_\sigma - \frac{\Gamma}{2} b_\sigma + \sqrt{\Gamma} b_\sigma^{\text{in}} - i\alpha h_0 c_\sigma - iV_0 a_{\bar{\sigma}} \tag{5.3c}$$

where V_0 is the coupling strength of disorder-induced scattering between the cw(ccw) high-Q phonon modes a_σ to the ccw(cw) phonon quasi-modes $b_{\bar{\sigma}}$. In contrast to the usual quantum optics literature, we here define detuning to be the mode frequency minus the signal frequency. Thus a positive detuning is red detuned. This makes comparison to mechanical motion as transparent as possible. Meanwhile, the coupling of the quasi-modes b_σ to the c_σ modes is given by $g_0\sqrt{n_\sigma}$, while $h_0\sqrt{n_\sigma}$ captures the coupling between a_σ and c_σ. For any given ω, there is a self-consistent $\omega_b \approx \omega$ that describes the relevant portion of the bath modes. Thus we take $|\omega_b - \omega| \ll \Gamma$ in

what follows. Specifically, we have the following main assumptions for this simple model:

1. Phonon backscattering occurs between high-Q phonon modes and the phonon quasi-modes, i.e. between $a_+ \longleftrightarrow b_-$ and $a_- \longleftrightarrow b_+$, with strength V_0.

2. The cw(ccw) optical mode $c_{+(-)}$ couples to the high-Q phonon mode $a_{+(-)}$ and the cw(ccw) phonon quasi-mode $b_{+(-)}$ with different strengths. The cw optical mode c_+ couples to the cw high-Q mode a_+ via direct optomechanical interaction with strength αh_0 and couples to the quasi-mode with strength αg_0. Likewise, the ccw optical mode c_- couples to the ccw high-Q mode a_- with strength βh_0 and couples to the ccw quasi-mode b_- with strength βg_0.

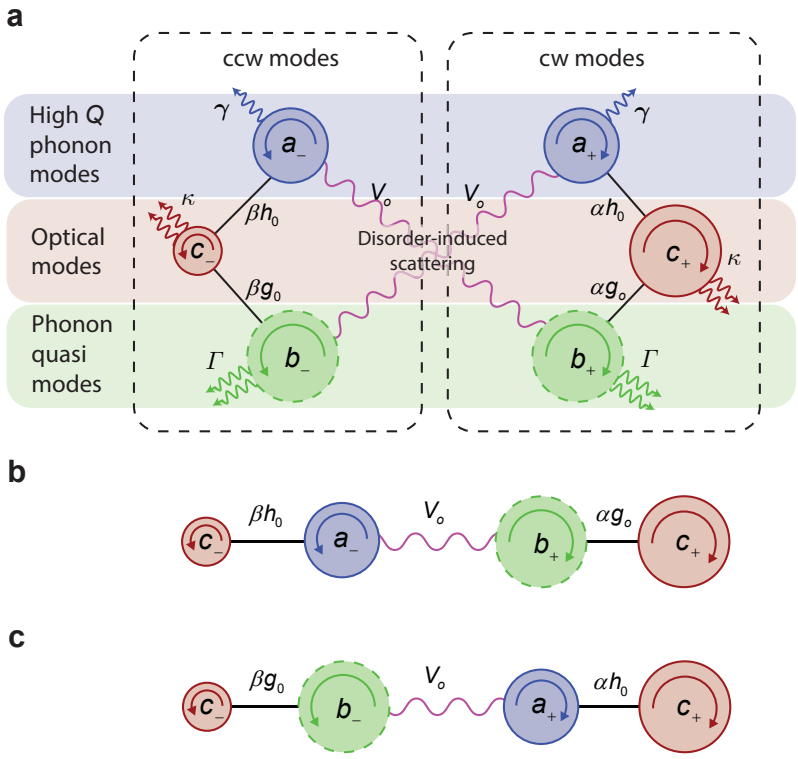

Figure 5.8: (a) Full description of the optomechanical coupling of the $c_\pm$ modes to $a_\pm$ modes and $b_\pm$ modes, and the disorder-induced scattering between the $a_\pm$ modes and $b_\mp$ modes. Separated optomechanical coupling descriptions by coupling directions (b)-(c). (b) The ccw-side coupling that the optical mode c_- is mainly coupled to the a_- mode with the disorder-induced scattering. (c) Likewise, the cw-side coupling that the cw mode c_- is coupled to the a_+ mode.

Here are n_+ and n_- are the number of intracavity photon in the cw optical mode c_+ and the ccw mode c_-, respectively.

3. The high-Q phonon modes $a_{+(-)}$ and the phonon quasi-modes $b_{+(-)}$ have the intrinsic damping rates γ and Γ, respectively ($\gamma \ll \Gamma$). The cw modes and ccw modes have symmetry with respect to the origin. We also assume that the damping rate Γ is in the same order as the optical loss rate κ.

We exclude a simpler model, of two degenerate mechanical modes and no additional quasi-modes, as it fails to produce two key features of the data. First, at low pump power, we would experimentally observe some mode splitting, representing a breaking of circular symmetry from disorder-induced scattering. Second, at high pump power, the lowest linewidth the backward mode could achieve would be equivalent to its initial linewidth, and its temperature would be equal to the bath temperature. Optical coupling to multiple mechanical modes is the next best alternative, and as we show here, describes these phenomena.

Based on these assumptions, we can obtain the simplified continuum model as shown in Fig 5.8.**a**. In principle, the dynamics of the system can be solved numerically. However the loop structure in this coupled six-mode system will complicate the result, rendering interpretation difficult. To better capture the main physics, we can make the following approximation: we assume the g_0 parameter is larger than h_0 so that the optical field couples more strongly to the bulk modes $b_\pm$. We note that this assumption is not actually that important for our main result, as the crucial point is that the dominant mechanical damping mechanism is coupling of the high Q modes to the quasi-modes – this is independent of g_0 and h_0. We can then break the loop into two pieces (see Fig 5.8.**a-c**).

5.2.5 Analysis of the Simplified Continuum Model

Susceptibilities of the High-Q Modes, $a_\pm$

We first focus on the ccw-side coupling direction (Figure 5.8.**b**) to calculate the linewidth of the ccw phonon a_-. Solving in the Fourier domain, we get

$$\begin{aligned}&\left[-i(\omega-\omega_m)+\gamma/2+\frac{\beta^2h_0^2}{-i(\omega-\Delta)+\kappa/2}+\frac{V_0^2}{\Gamma/2}\left(1-\frac{\alpha^2g_0^2}{\Gamma\tilde{\kappa}/2}\right)\right]a_-\\ =\;&\sqrt{\gamma}a_-^{\text{in}}-\frac{i\beta h_0\sqrt{\kappa}}{-i(\omega-\Delta)+\kappa/2}c_-^{\text{in}}-\frac{V_0\alpha g_0\sqrt{\kappa}}{\Gamma\tilde{\kappa}/2}c_+^{\text{in}}-\frac{iV_0}{\sqrt{\Gamma}/2}\left(1-\frac{\alpha^2g_0^2}{\Gamma\tilde{\kappa}/2}\right)b_+^{\text{in}}\end{aligned}\tag{5.4}$$

where $\tilde{\kappa}\triangleq -i(\omega-\Delta)+\kappa/2+2\alpha^2g_0^2/\Gamma$. Similarly, for the cw phonon mode a_+, we can find its equation of motion by interchanging α with β, a_+ with a_-, and c_+ with c_-:

$$\begin{aligned}&\left[-i(\omega-\omega_m)+\gamma/2+\frac{\alpha^2h_0^2}{-i(\omega-\Delta)+\kappa/2}+\frac{V_0^2}{\Gamma/2}\left(1-\frac{\beta^2g_0^2}{\Gamma\tilde{\kappa}'/2}\right)\right]a_+\\ =\;&\sqrt{\gamma}a_+^{\text{in}}-\frac{i\alpha h_0\sqrt{\kappa}}{-i(\omega-\Delta)+\kappa/2}c_+^{\text{in}}-\frac{V_0\beta g_0\sqrt{\kappa}}{\Gamma\tilde{\kappa}'/2}c_-^{\text{in}}-\frac{iV_0}{\sqrt{\Gamma}/2}\left(1-\frac{\beta^2g_0^2}{\Gamma\tilde{\kappa}'/2}\right)b_-^{\text{in}}\end{aligned}\tag{5.5}$$

with $\tilde{\kappa}'\triangleq -i(\omega-\Delta)+\kappa/2+2\beta^2g_0^2/\Gamma$. The susceptibilities of the $a_\pm$ modes are given by the left hand side of the equations of motion:

$$\chi_{a_+}^{-1}(\omega) = -i(\omega-\omega_m)+\gamma/2+\frac{\alpha^2h_0^2}{-i(\omega-\Delta)+\kappa/2}+\frac{V_0^2}{\Gamma/2}\left(1-\frac{\beta^2g_0^2}{\Gamma\tilde{\kappa}'/2}\right)\tag{5.6a}$$

$$\chi_{a_-}^{-1}(\omega) = -i(\omega-\omega_m)+\gamma/2+\frac{\beta^2h_0^2}{-i(\omega-\Delta)+\kappa/2}+\frac{V_0^2}{\Gamma/2}\left(1-\frac{\alpha^2g_0^2}{\Gamma\tilde{\kappa}/2}\right).\tag{5.6b}$$

Linewidths of the $a_\pm$ Modes

We can define the cooperativities as $\mathcal{C}_\alpha=4\alpha^2g_0^2/\Gamma\kappa$ and $\mathcal{C}_\beta=4\beta^2g_0^2/\Gamma\kappa$, which are both dimensionless parameters describing the strength of optomechanical coupling relative to cavity decay rate and mechanical damping rate. Under the phase matching condition that the pump laser and its scattered light are near the two frequency-adjacent optical modes, we can expect $\Delta\approx\omega_m$ (see Fig 5.9). To evaluate

the linewidth of the high-Q phonon modes, we set $\omega \approx \omega_m$. Then we have:

$$\gamma_{a_+} = \gamma + \frac{4\alpha^2 h_0^2}{\kappa} + \frac{4V_0^2}{\Gamma}\frac{\kappa}{\kappa + 4\beta^2 g_0^2/\Gamma} = \gamma + \frac{4\alpha^2 h_0^2}{\kappa} + \frac{4V_0^2}{\Gamma}\frac{1}{1+\mathcal{C}_\beta}, \quad (5.7a)$$

$$\gamma_{a_-} = \gamma + \frac{4\beta^2 h_0^2}{\kappa} + \frac{4V_0^2}{\Gamma}\frac{\kappa}{\kappa + 4\alpha^2 g_0^2/\Gamma} = \gamma + \frac{4\beta^2 h_0^2}{\kappa} + \frac{4V_0^2}{\Gamma}\frac{1}{1+\mathcal{C}_\alpha} \quad (5.7b)$$

where γ_{a_+} and γ_{a_-} are the linewidths of the high-Q phonon modes $a_\pm$. Note that the linewidths $\gamma_{a_\pm}$ are larger than their minimum measurable linewidth $\gamma_m = \gamma + \frac{4V_0^2}{\Gamma}$ (obtained when optical power is zero, i.e. $\alpha = 0$, $\beta = 0$) due to the disorder induced backscattering to the counter-propagating quasimode (see Eq. 2)

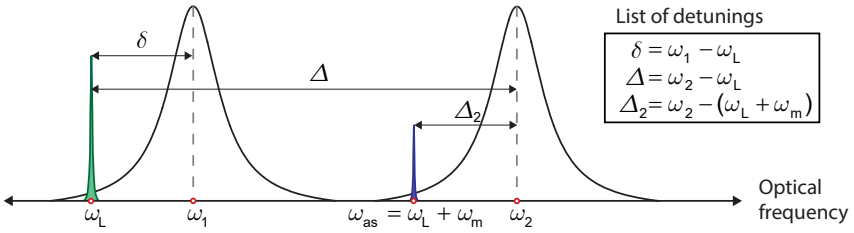

Figure 5.9: Optical frequency relationship of the triplet resonant system for the experiment. The pump laser is at frequency ω_L, and the anti-Stokes scattered light appears at frequency $\omega_{as} = \omega_L + \omega_m$ via Brillouin scattering. The two frequency-adjacent optical modes are at ω_1 and ω_2, and the corresponding signal detunings are defined as $\delta = \omega_1 - \omega_L$, $\Delta = \omega_2 - \omega_L$ and $\Delta_2 = \omega_2 - \omega_{as}$.

Effective Temperature of the Phonon Modes

Another important feature that comes from the continuum model is the reduction in the effective temperature of the a_- mode, because of coherent damping of the $\sigma = +$ mechanical modes. When the right-hand side of the equation (5.4) is considered with an assumption that the optical noise c_σ^{in} is negligible compared to the thermal noise source, we have the effective noise on a_- as:

$$\sqrt{\gamma} a_-^{\text{in}} - \frac{iV_0}{\sqrt{\Gamma}/2}\left(1 - \frac{\alpha^2 g_0^2}{\Gamma\tilde{\kappa}/2}\right) b_+^{\text{in}} \quad (5.8)$$

The effective temperature of mode a_- is then given by:

$$\begin{aligned} T_{a_-}^{\text{eff}} &= \frac{1}{\gamma_{a_-}}\left[\gamma + \frac{V_0^2}{\Gamma/4}\left|1 - \frac{\alpha^2 g_0^2}{\Gamma\tilde{\kappa}/2}\right|^2\right] T_{\text{bulk}} \\ &= \frac{1}{\gamma_{a_-}}\left[\gamma + \frac{4V_0^2}{\Gamma}\frac{(\omega-\Delta)^2 + \kappa^2/4}{(\omega-\Delta)^2 + (\kappa/2 + 2\alpha^2 g_0^2/\Gamma)^2}\right] T_{\text{bulk}} \end{aligned} \tag{5.9}$$

When near resonance, $\omega \approx \Delta$, we have:

$$\begin{aligned} T_{a_-}^{\text{eff}} &= \frac{1}{\gamma_{a_-}}\left[\gamma + \frac{4V_0^2}{\Gamma}\frac{\kappa^2/4}{(\kappa/2 + 2\alpha^2 g_0^2/\Gamma)^2}\right] T_{\text{bulk}} \\ &= \frac{1}{\gamma_{a_-}}\left[\gamma + \frac{4V_0^2}{\Gamma}\frac{1}{(1+\mathcal{C}_\alpha)^2}\right] T_{\text{bulk}} \end{aligned} \tag{5.10}$$

It reveals that the second term in equation (5.10) decreases with increasing $\mathcal{C}_\alpha$. This fact indicates the effective temperature of the ccw a_- mode reduces with increase of the cw pump laser ($\propto |\alpha|^2$). We can derive the effective temperature of the a_+ mode in the same manner.

$$T_{a_+}^{\text{eff}} = \frac{1}{\gamma_{a_+}}\left[\gamma + \frac{4V_0^2}{\Gamma}\frac{1}{(1+\mathcal{C}_\beta)^2}\right] T_{\text{bulk}}. \tag{5.11}$$

In the experiment shown in the main paper, the ccw probe β is much smaller compared to the cw pump α, thus this effective temperature $T_{a_+}^{\text{eff}}$ change is not significant for the a_+ mode.

Analysis of the Direct Coupling Model

For the direct coupling model, i.e. disorder only coupling a_- and a_+ via V_1 and no additional quasi-modes, we can find striking differences from the observations. After adiabatic elimination of $c_\pm$, we have Heisenberg-Langevin equations for $V_0 = 0$ of

$$\dot{a}_- = -[i\omega_m + (\gamma + \Gamma_\beta)/2]a_- + \sqrt{\gamma}a_{-,in} - iV_1 a_+ \tag{5.12}$$

$$\dot{a}_+ = -[i\omega_m + (\gamma + \Gamma_\alpha)/2]a_+ + \sqrt{\gamma}a_{+,in} - iV_1 a_- \tag{5.13}$$

with $\Gamma_\alpha \equiv 4h_0^2|\alpha|^2/\kappa$ the optically-induced damping. We see that the normal modes of these equations have resonance conditions corresponding to two poles:

$$\omega_\pm = \omega - i\Gamma_\Sigma/2 \pm \sqrt{V_1^2 - \delta\Gamma^2/4} \tag{5.14}$$

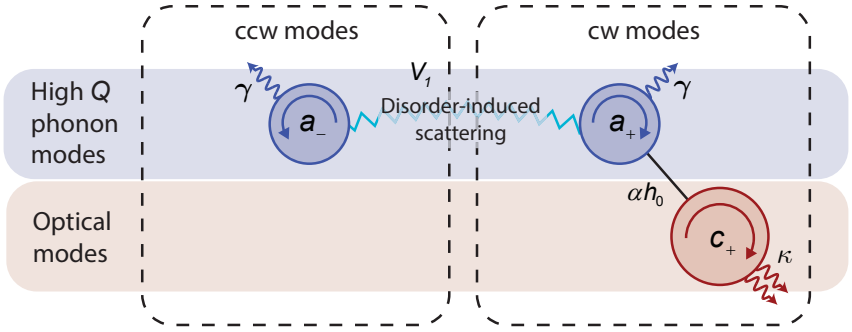

Figure 5.10: The 'direct coupling model' consists of the optomechanical coupling of the c_+ optical mode to the a_+ high-Q mode, and direct disorder-induced coupling between the $a_\pm$ modes. αh_0 is the light-enhanced optomechanical coupling strength and V_1 is the direct coupling rate.

where $\Gamma_\Sigma = \gamma + \frac{\Gamma_\beta + \Gamma_\alpha}{2}$ is the average damping and $\delta\Gamma = |\Gamma_\alpha - \Gamma_\beta|$ is the difference in damping. Thus at zero power the two poles are split on the real axis by $\pm V_1$, leading to mode splitting which is not observed in the experiment. Furthermore, as $\delta\Gamma$ increases to be larger than V_1, the damping rates start to differ, whereas in the experiment the damping is different for all optical powers. Finally, at high $\delta\Gamma$, the imaginary (damping) part of the pole is still always $\geq \gamma$, the value of the damping at zero optical power in this model, counter to the observed behavior in the experiment. Regarding the temperature of the a_- mode, working in the large $\delta\Gamma$ limit, we do see some cooling of a_- at intermediate powers, as predicted in Ref. [157].

5.2.6 Model for chiral cooling

We now propose a model, detailed in Ref. [85], that incorporates all the essential physics described above and illustrated in Fig. 5.11. Specifically, we define the higher frequency optical modes (anti-Stokes) through annihilation operators c_σ, with parity $\sigma = +$ for cw photons and $\sigma = -$ for ccw photons. These optical modes couple to the matched high-Q phonon mode a_σ, via direct optomechanical interaction with strength αh_0 (or βh_0), and also couple to the quasi-mode b_σ with strength αg_0 (or βg_0). In all cases these interactions conserve parity σ. h_0 and g_0 are the bare (single photon/phonon) optomechanical coupling strengths, while α and β are the square root of the intracavity photon number in cw and ccw direction respectively due to the pump and probe lasers. We note that the optomechanical coupling to the quasi-mode (itself comprised of many low-Q modes) can be large, due to the mode

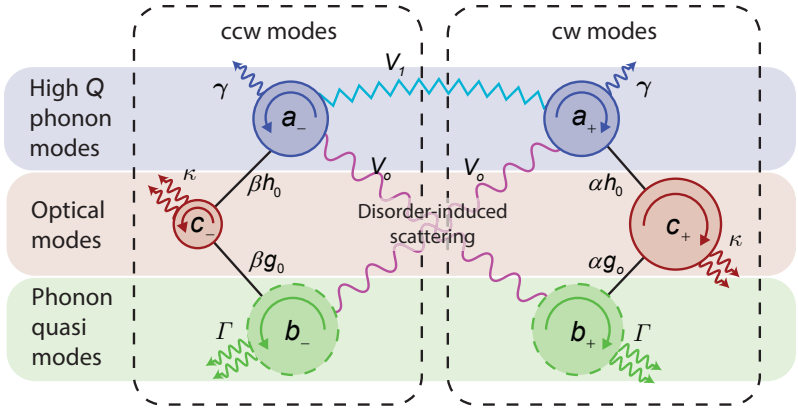

Figure 5.11: Model for coupling between the anti-Stokes (higher frequency) optical modes $c_\pm$, high-Q phonon modes $a_\pm$, and phonon quasi-modes $b_\pm$ in cw and ccw directions. Light couples to the $a_\pm$ and $b_\pm$ phonons with different optomechanical interaction strength. Disorder-induced scattering between $a_\pm$ phonons and the $b_\mp$ quasi-mode occurs with strength V_0, and between $a_\pm$ and $a_\mp$ high-Q phonons occurs with strength V_1. Our experimental case features $V_1 \ll V_0$. Details on individual parameters are provided in the text.

overlap highlighted in Fig. 5.6.

To see the role chirality plays, we now also include the existence of disorder-induced scattering between a_σ and $b_{\bar{\sigma}}$ modes having strength V_0 – a term that explicitly breaks the conservation of parity. We note that the definition of our modes already account for low-angle scattering that conserves parity but leads to damping. Thus we do not include a direct a_σ to b_σ term in our theory, as it is included in the definition of intrinsic linewidths γ (for a_σ) and Γ (for b_σ). We can thus represent this toy model system with the interaction Hamiltonian expression given by:

$$\begin{aligned} H_{\text{int}} = \alpha c_+^\dagger (h_0 a_+ + g_0 b_+) + \beta c_-^\dagger (h_0 a_- + g_0 b_-) \\ + V_0 (a_-^\dagger b_+ + b_+^\dagger a_-) + \text{h.c.} \end{aligned} \tag{5.15}$$

The full model including the dissipation and detuning terms is provided in sSection 5.2.4.

We can now derive the equations of motion for this system by means of the Heisenberg-Langevin equation (see Section 5.2.5). The key features of our data can be understood simply by a series of adiabatic elimination steps. First, we adiabatically eliminate the c_+ optical mode with linewidth $\kappa \gg \gamma_m$, which leads to sideband

cooling of both a_+ and b_+. In particular, the mode b_+ having bare linewidth Γ, is damped optically with a rate ΓC_α from this adiabatic elimination. The parameter $\mathcal{C}_\alpha$ is the quasi-mode optomechanical cooperativity defined as $4\alpha^2 g_0^2/\Gamma\kappa$.

Viewing the quasi-mode as a bath, we see that this cw bath is cooled to a temperature $T_{b+} \approx T_{\rm bulk}/(1+C_\alpha)$ via sideband cooling. This chiral refrigeration in turn modifies the damping and temperature of the a_- mode. Specifically, adiabatic elimination of the quasi-mode b_+ leads to an effective damping of the a_- mode. At zero optical power, we have bare linewidth $\gamma_m = \gamma + 4|V_0|^2/\Gamma$, where γ is the intrinsic linewidth of a_-. As we increase the optical power, we see that the disorder-induced damping term reduces due to the increased damping of the b_+ quasi-mode – this is an optically induced impedance mismatch. Consequently, if there were no probe light, we would see that the a_- damping rate reduces to

$$\gamma_{a-} = \gamma + \frac{4|V_0|^2}{\Gamma(1+C_\alpha)} \ . \tag{5.16}$$

We can also see that the temperature of the a_- mode should go to a weighted sum of these two terms (details in Section 5.2.5):

$$T_{a-} = \frac{\gamma T_{\rm bulk} + (\gamma_{a-} - \gamma) T_{b+}}{\gamma_{a-}} \tag{5.17}$$

As $T_{b+} < T_{\rm bulk}$, we see that for moderate C_α, the temperature T_{a-} goes down, even as $\gamma_{a-} < \gamma_m$! Conventional optomechanical cooling involves an increase of mechanical damping while the heat load remains constant, resulting in a lowering of the mode temperature. Here, we see that while the damping reduces, the heat load on the system also reduces. This leads to a lower effective temperature of the mechanical system even as the linewidth narrows. Important corrections due to the finite probe power lead to additional broadening and cooling of the a_- mode, while the a_+ mode's dynamics are dominated by the sideband cooling from the αh_0 coupling. But the key features are described by the above picture of chiral refrigeration.

We excluded a simpler model, of two degenerate mechanical modes $a_\pm$ coupled by disorder of strength V_1 and no additional quasi-modes, as it fails to produce two key features of the data below. First, at low pump power, we would see significant mode splitting (below we set an experimental bound for the direct coupling rate between $a_\pm$ modes at $V_1 < 1$ kHz), representing a breaking of parity conservation

due to disorder-induced scattering. Second, at high pump powers, explored below, the smallest linewidth that the backward mode could achieve would be equivalent to its initial linewidth and its temperature would be equal to the bath temperature. We present a more detailed analysis of this model in Section 5.2.5. Optical coupling to multiple (bulk) mechanical modes is the next best alternative, and as we show above, describes these phenomena.

5.2.7 Disorder suppression and optomechanical cooling without damping

We now return to the experimental results to demonstrate the key predictions of this model: (i) damping associated with disorder-induced scattering can be optically inhibited, (ii) the damping rate of ccw phonons can be brought below the bare linewidth γ_m, and (iii) the process leads to a reduction in heat load. Here, we employ an erbium doped fiber amplifier to control the cw pump power (P_{cw}) while keeping the ccw probe power constant at 12.5 μW. The anti-Stokes Brillouin scattered light in the resonator is kept close to zero detuning from its optical mode to maximize cooling efficiency, i.e. $|\Delta_2/\kappa|$ is always less than 10 %. Since the ccw probe adds some fixed optical damping to the ccw phonons, the initial measurement of γ_{a-} is at 17.8($\pm$1) kHz, which is greater than the bare linewidth γ_m.

As we increase cw pump power from 140.9 μW to 195.4 μW, the added optical damping broadens the cw phonon linewidth γ_{a+} (Fig. 5.12b). The striking feature of this experiment is that the ccw phonon linewidth γ_{a-} simultaneously reduces, i.e. the ccw phonons become more coherent! We verify that the increased coherence of the ccw phonons is not associated with any gain (Fig. 5.12c) by observing their spectrum through the measured photocurrent (See Section 3.4). In fact, quite the opposite occurs, and the total integrated area under the phonon spectrum also reduces, indicating a reduction in temperature of the a_- phonons. Since the ccw optical probe was not modified, the optically induced damping from the probe laser remains fixed. The reduction of the γ_{a-} linewidth thus indicates that a hidden contribution to dissipation is being eliminated when the cw pump power is increased. At the highest power, the smallest dressed linewidth $\gamma_{a-} = 10.5(\pm 1.7)$ kHz is below the bare linewidth $\gamma_m = 12.5(\pm 1)$ kHz measured at the start of the experiment, even including the extra sideband damping from probe β. Fitting of the power vs linewidth measurements to our model in Eqs. (5.7) reveals the ratio of coupling rates

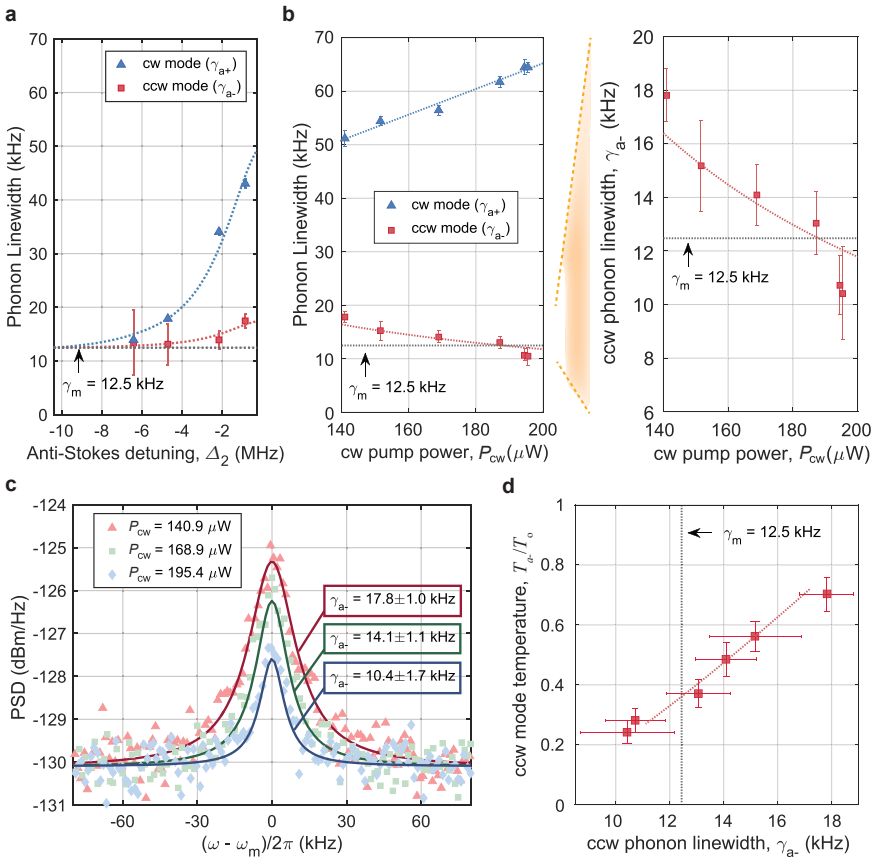

Figure 5.12: Chiral refrigeration in a silica whispering gallery resonator. **(a)** Experimental measurement of bare phonon linewidth γ_m and observation of chiral asymmetry in dissipation rates for cw and ccw phonons during the initial sideband cooling experiment. Blue and red dashed lines in subfigures a and b are fits to theory in Eqs. (5.7). **(b)** Observation of increasing ccw phonon coherence during sideband cooling of the cw propagating phonons (fixed ccw probe). The ccw phonon linewidth γ_{a-} drops below the bare linewidth γ_m, indicating reduction in the disorder induced dissipation. **(c)** Measured photocurrent PSD (proportional to ccw phonon PSD) during experiment of subfigure b. The ccw phonons experience gain-free spectral narrowing and cooling (reduction in spectrum area) when the cw laser $P_{\rm cw}$ is increased. Solid lines are Lorentzian fits to the data. **(d)** Measured ccw phonon mode temperature $T_{a-}^{\rm eff}$ vs linewidth γ_{a-} showing that, in contrast to sideband cooling, both the linewidth and temperature decrease during this experiment. Temperature is calculated using the integrated phonon power spectrum (examples in subfigure c), with vertical error bars generated from amplitude uncertainty. Red dashed line is a fit to the theory of Eqns. 5.16 and 5.17. The phonon mode starts pre-cooled due to the sideband cooling from the probe. All error bars correspond to 95 % confidence intervals for their respective parameters.

$V_0/g_0 = 1.15(\pm 0.05) \times 10^3$. Our model indicates that the observed reduction in the phonon linewidth γ_{a-} occurs due to reduction of the disorder-induced scattering. Specifically, the ccw propagating phonons achieve appreciable robustness against disorder due to chiral optomechanical damping of the cw phonon quasi-mode.

In Fig. 5.12d we present the temperature T_{a-} of the ccw phonon mode measured through phonon power spectral area, as a function of its measured linewidth. Fitting this temperature data to our model in Section 5.2.5 permits extraction of $V_0^2/\Gamma = 2.8(\pm 0.32)$ kHz. The parameters V_0, g_0, and Γ cannot presently be further separated since the phonon quasi-modes $b_\pm$ are not directly observable. However, we note that the minimum self-consistent quasi-mode linewidth is approximately the optical linewidth ($\Gamma \approx \kappa$) and we can obtain the values $V_0 = 121(\pm 13)$ kHz and $g_0 = 105(\pm 12)$ Hz at this minimum. These estimates are commensurate with our earlier assumption that the disorder induced scattering between the high-Q and quasi-modes dominates over direct scattering between the high-Q modes (i.e. $V_0 \gg V_1$). We additionally learn that the lower limit of g_0 is roughly 7.5 times h_0, implying that the optomechanical coupling to the quasi-mode is significant, and which agrees with the number of phonon modes that are likely to compose the quasi-mode. The anomalous cooling that we observe is thus well explained by significant coupling to, and chiral refrigeration of the cw quasi-mode bath.

5.2.8 Discussion

Sideband cooling has been to date the only mechanism available for suppressing the thermal motion of mechanical resonators using light – but is necessarily accompanied by linewidth broadening. In this work, we have demonstrated the existence of a fundamentally different mechanism for cooling mechanical oscillators, that occurs through sideband cooling of the bath modes. No previous experiment in optomechanics has provided either direct or indirect evidence of such bath cooling. More importantly, this mechanism has the potential to revolutionize the noise calculus that we employ, since the cooling is instead accompanied by linewidth narrowing! Additionally, we have demonstrated for the first time that not only can phonon chirality be induced optically, but also that it mitigates the influence of disorder on propagating phonons, a technique that potentially revolutionizes phonon-assisted measurements. To date such scattering immunity for phonons has only been demonstrated in topological insulators. Our results thus dramatically push forward the

known physics for both laser cooling and for monolithic chiral systems.

Our approach for inducing chiral behavior is, at present, confined to the narrowband response of a high-Q resonator system. However, such devices are already in use for metrological applications [147, 148, 149, 150] including atomic force microscopes [160] and quantum-regime transducers [161, 162]. In all these cases, increasing the quality factor while reducing the heat load of the mechanical element would lead to a direct improvement in performance. Furthermore, the modification of phonon transport by light may have substantial impact even beyond contemporary devices, as the ability to dynamically reconfigure the phononic behavior may change the realm of possibility as currently conceived. Still, robust demonstration of chiral asymmetry and non-reciprocal behavior remains close, and our work provides a foundation upon which to build such demonstrations.

Chapter 6

Suppression of disorder-induced scattering of photons

6.1 Introduction

[1] Rayleigh scattering is routinely encountered in nanostructured photonic devices as it limits microresonator quality (Q) factors [11, 6, 163], affects the stability of frequency combs [164, 165], causes Anderson localization [166], and limits the performance of metasurfaces [167]. It can be induced by inhomogeneities in the form of internal stresses, point defects, density variations, dislocations, and even surface roughness, which are unavoidable due to manufacturing limitations but may also occur thermodynamically. In particular, back-reflections arising from Rayleigh scatterers in nanostructured devices create prominent reflections in silicon photonics [168] and a well-known mode splitting or 'doublet' phenomenon in resonators [11, 6, 163, 169], both of which impose severe technological constraints.

An elegant proposal to counteract disorder-induced backscattering of electromagnetic waves is to break the time-reversal symmetry (TRS) of the medium [13, 14] – so that modes available for opposite, i.e., time-reversed, propagation are simply not symmetric in energy-momentum space. In other words, backscattering can be suppressed by establishing a large contrast in the optical density of states for propagation in the opposing directions. This effect has been experimentally confirmed in Faraday rotator (magneto-optic) materials biased with large magnetic fields [15] but cannot be extended to common dielectrics. A similar effect in which broken TRS suppresses electron backscattering is also seen in the chiral edge currents of two-dimensional electron systems exhibiting the quantum Hall effect (QHE) [151, 16]. More recently, there has been a flurry of activity on backscattering suppression via TRS-breaking in photonic topological insulator metamaterials after the analogy to the QHE was established [170], with successful demonstration in a magneto-optic

[1] Portions of this chapter are available at arXiv:1803.02366(under review)

photonic crystal [17] and through Floquet pumping [171]. Unfortunately, since common photonic materials do not have magneto-optical activity and are topologically trivial insulators in their band gaps, how these lessons may be mapped to any monolithic dielectric waveguide remains an open question.

Here, we demonstrate a simple optomechanical approach by which we can dynamically suppress electromagnetic backscattering in any dielectric. The approach relies on an induced transparency process supported by Brillouin light scattering, which is a high gain optical nonlinearity available in all phases of matter, and has been established as a highly effective tool for breaking TRS in dielectric waveguides and resonators [22, 18, 23]. Using this technique, we experimentally demonstrate near-complete suppression of Rayleigh backscattering within monolithic silica microresonators, with dynamic control provided by an external optical pump. The effect is confirmed both through elimination of back-reflected light as well as elimination of the normal mode splitting between cw and ccw modes of the symmetric resonators. Our experiments exhibit a restoration to the intrinsic material loss rate of an optical resonator in spite of the presence of scattering defects.

6.2 System description

The system under consideration (Fig. 6.1a) is a symmetric whispering gallery resonator (WGR) that supports two degenerate optical modes $a_{\pm}$ associated with clockwise (+ or cw) and counter-clockwise (- or ccw) photon propagation. Such degenerate modes, which are time-reversed partners, can be coupled through backscattering from inhomogeneities or defects, resulting in a doublet mode if the coupling rate is comparable to the optical loss rate [11, 6, 163]. For lower backscattering rates the mode only appears slightly broadened from its intrinsic linewidth. Fig. 6.1b exhibits this backscattering induced mode split measured in a silica microsphere WGR. The measurement is performed via evanescent probing through a tapered fiber waveguide (Fig. 6.1a) such that the optical resonances appear as a dip in transmission. Optical probing in both directions through the waveguide indicates that the $a_{\pm}$ modes are hybridized due to Rayleigh backscattering [11, 6, 163] and have lost their distinguishable directionality. It is this detrimental mode splitting and broadening effect that we wish to mitigate.

In order to experimentally shut down the effect of the backscattering chan-

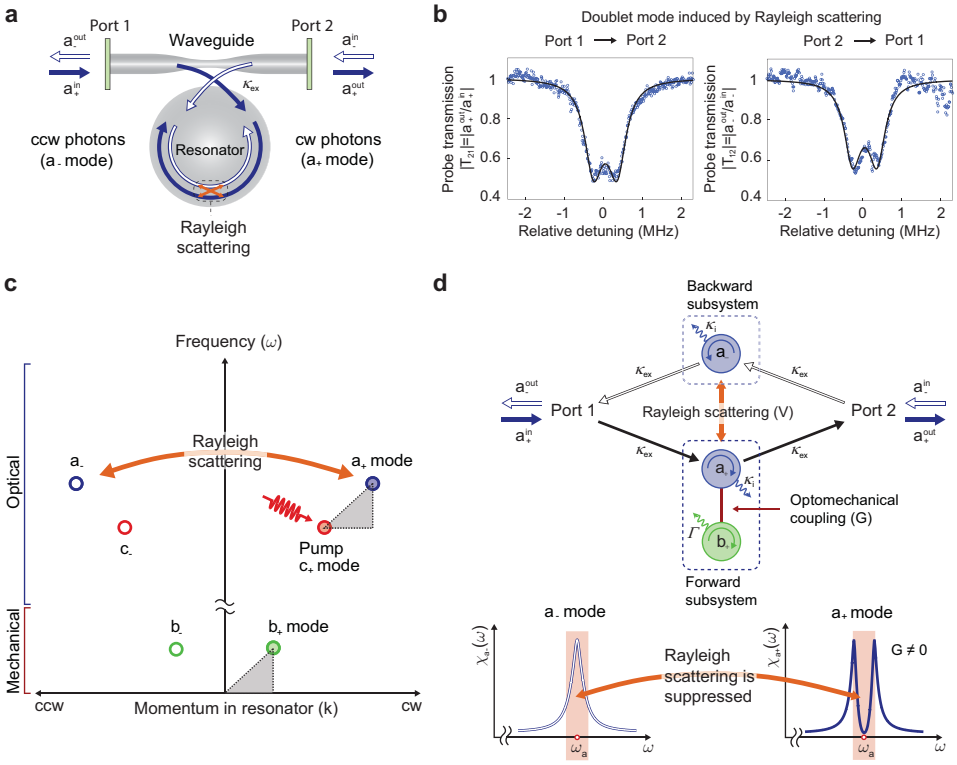

Figure 6.1: Rayleigh backscattering in a whispering gallery resonator (WGR) and concept for optomechanical suppression. (a) Optical WGRs support degenerate modes ($a_\pm$) that are time-reversed partners (cw/ccw) and can be individually accessed via directional probing. However, Rayleigh backscattering from disorder intrinsic to the WGR can couple these modes, leading to loss of their distinguisable directionality. **(b)** Experimentally, this can result in normal mode splitting or 'doublet' (measured here in a silica WGR) when the disorder induced backscattering rate is comparable to the intrinsic optical loss rate. Such doublets are routinely observed in high-Q resonator systems and impose a technological constraint. **(c)** We can suppress Rayleigh backscattering by breaking time-reversal symmetry within the bandwidth of the $a_\pm$ optical modes. This is achieved through a Brillouin optomechanical induced transparency process [18, 20], in which a high-coherence cw mechanical mode b_+ is coupled to the cw a_+ mode by a cw directional pump c_+. The interaction is subject to the phase matching constraint illustrated by the grey triangle. The momentum matching requirement implies that the cw pump does not directly induce any effect for the ccw optical mode a_-. **(d)** Toy model for the WGR and waveguide system in which we distinguish the two directional subsystems and indicate both Rayleigh (V) and optomechanical (G) couplings. All variables are defined in the main text. The directional Brillouin optomechanical coupling significantly reduces the susceptibility of the a_+ mode only and 'open-circuits' the backscattering channel, thereby suppressing Rayleigh scattering.

nel between a_+ and a_- we break time-reversal symmetry within the bandwidth of these modes. Specifically we employ Brillouin scattering induced transparency (BSIT) [18], which is a non-reciprocal process that allows us to only modify the susceptibility $\chi_{a+}(\omega)$ of the a_+ mode while leaving the a_- mode nominally unaffected (Fig. 6.1d-bottom). As with other optomechanically-induced transparencies [116, 115], the BSIT arises due to coherent coupling [172] between an optical mode with long-lived mechanical state, that is enabled through radiation forces and photoelastic scattering. When the coupling rate between light and the mechanics is sufficiently large, the optical mode exhibits normal mode splitting – hybridization of the mechanical and optical modes – which inhibits on-resonance absorption from the waveguide. Production of BSIT requires a Stokes-detuned pump optical field (on a different optical mode c_+) that co-propagates with the mode of interest a_+, and a high-Q mechanical whispering gallery mode b_+ within the WGR. These three modes must together be subject to the Brillouin phase matching condition on both frequency $\omega_a = \omega_c + \omega_b$ and momentum $k_a = k_c + k_b$ as illustrated in Fig. 6.1c. In the experiment we use c_+ pumping only, although a c_- pump could also be invoked to independently control the susceptibility for the a_- mode [20]. It is the unique, momentum-selective feature of BSIT that allows us to break TRS for light propagation within the resonator.

6.3 System model including Rayleigh scattering and optomechanical coupling

Our whispering gallery resonator (WGR) system supports two frequency-adjacent optical modes, the mode of interest $a_\pm$ and Stokes shifted pump mode $c_\pm$, and a mechanical mode $b_\pm$. All three modes are of whispering gallery mode (WGM) type and exist as degenerate pairs in the cw (+) and ccw (-) direction. As described in the main text (Fig. 1), the cw optical modes a_+ and c_+ couple through the cw mechanical mode b_+ via optomechanical interaction:

$$H_{\text{int}}^{\text{OM}} = \hbar(g_o c_+ a_+^\dagger b_+ + g_o^* c_+^\dagger a_+ b_+^\dagger)$$

We define the single photon Brillouin optomechanical coupling rate $g_o \propto \delta(\Delta k) \int \phi_1 \phi_2 \psi \, d^2r$, where ϕ_1, ϕ_2 and ψ are the transverse mode shapes of the optical and mechanical modes, respectively. The delta function $\delta(\Delta k)$ represents the momentum selection

condition for Brillouin scattering, i.e. the momentum difference between the optical modes a_+ and c_+ must match the momentum of the mechanical mode b_+. We also consider the interaction of the cw optical modes (a_+, c_+) with their time-reversed counterparts (a_-, c_-) via elastic Rayleigh backscattering. This coupling can be induced by surface or internal inhomogeneities [11, 6, 173, 174] in WGRs. Under the dipole approximation, we can write the interaction Hamiltonian due to Rayleigh scattering for the optical mode pairs as follows [163]:

$$H_{\rm int}^{\rm R} = \hbar V_o(a_+^\dagger a_- + a_-^\dagger a_+) + \hbar V_1(c_+^\dagger c_- + c_-^\dagger c_+)$$

Here, we have defined V_o and V_1 as the backscattering rates for the $a_\pm$ and $c_\pm$ modes, respectively. These coupling rates are given by $2V_{i=0,1} = -\alpha f_i^2(r)\omega_i/\mathcal{V}_{\rm m}^i$ where α is the polarizability of the scatterer, $f_i(r)$ accounts for the overlap of the optical field with the scatterer dipole, ω_i is the resonant frequency of the optical mode and $\mathcal{V}_{\rm m}^i$ is its modal volume [163]. The normal-mode splitting induced by Rayleigh backscattering is easily experimentally observable if $V_i > \kappa/2$.

Considering the two interaction Hamiltonians, we can now represent the linearized Heisenberg-Langevin equations of our system. Under the non-depleted pump approximation we are able to omit the equations for $c_\pm$, which leads to the equations of motion:

$$\frac{da_+}{dt} = -\left(\frac{\kappa}{2} + i\Delta_a\right)a_+ - iGb_+ - iV_o a_- + \sqrt{\kappa_{\rm ex}}a_+^{\rm in}(t) + \sqrt{\kappa_i}a_{\rm vac}(t), \tag{6.1a}$$

$$\frac{db_+}{dt} = -\left(\frac{\Gamma}{2} + i\Delta_b\right)b_+ - iG^* a_+ + \sqrt{\Gamma}b_{\rm th}(t), \tag{6.1b}$$

$$\frac{da_-}{dt} = -\left(\frac{\kappa}{2} + i\Delta_a\right)a_- - \eta Gb_- - iV_o a_+ + \sqrt{\kappa_{\rm ex}}a_-^{\rm in}(t) + \sqrt{\kappa_i}a_{\rm vac}(t), \tag{6.1c}$$

$$\frac{db_-}{dt} = -\left(\frac{\Gamma}{2} + i\Delta_b\right)b_- + \eta G^* a_- + \sqrt{\Gamma}b_{\rm th}(t). \tag{6.1d}$$

Here $a_\pm^{\rm in}$ are the normalized probe laser amplitudes within the waveguide, in forward (+) and backward (-) directions. They are defined as $|a_\pm^{\rm in}|^2 = P_{\rm probe\pm}^{\rm in}/\hbar\omega_{\rm probe}$, where $P_{\rm probe\pm}^{\rm in}$ is the corresponding input probe laser power into the waveguide and $\omega_{\rm probe}$ is the probe laser frequency. $\sqrt{\kappa_{\rm ex}}$ appears due to the external coupling to a side-coupled waveguide. $a_{\rm vac}(t)$ and $b_{\rm th}(t)$ are the vacuum and thermal noise in the optical and mechanical modes, respectively. κ and Γ are the total loss rates of the

$a_\pm$ and $b_\pm$ modes respectively. The detuning terms are defined as $\Delta_a = \omega_a - \omega_{\text{probe}}$ and $\Delta_b = \omega_b - (\omega_{\text{probe}} - \omega_{\text{pump}})$, where ω_a and ω_b are resonant frequencies of $a_\pm$ and $b_\pm$ modes respectively, and ω_{pump} is the pump laser frequency. $G \triangleq g_o\sqrt{n_p}$ is the pump-enhanced optomechanical coupling due to the c_+ pump. Since we also wish to take into account Rayleigh scattering for the $c_\pm$ modes, there may be some backscattered pump power from the cw pump mode c_+ into the ccw pump mode c_-, which creates non-zero optomechanical interaction in the ccw direction. In the above equations we have incorporated this ccw optomechanical interaction by introducing $\eta = 2V_1/\kappa_c$, where κ_c is the optical loss rate of the $c_\pm$ modes. After this accounting we are no longer interested in the pump equations of motion, so we can dispense with the $V_{0,1}$ distinctions and instead replace a single backscattering rate $V = V_0$ between the $a_\pm$ modes.

Fig. 6.2 presents the toy model of our system, in which the forward and backward subsystems of the resonator are deliberately identified separately. As explained in the main text, the transmission coefficients must be different (Fig. 6.2b and 6.2c). On the other hand, the two reflection coefficients must be identical since the light experiences both forward and backward optical susceptibilities in series (Fig. 6.2d and 6.2e), i.e. the reflection system is identical in either direction ($R = R_{11} = R_{22}$).

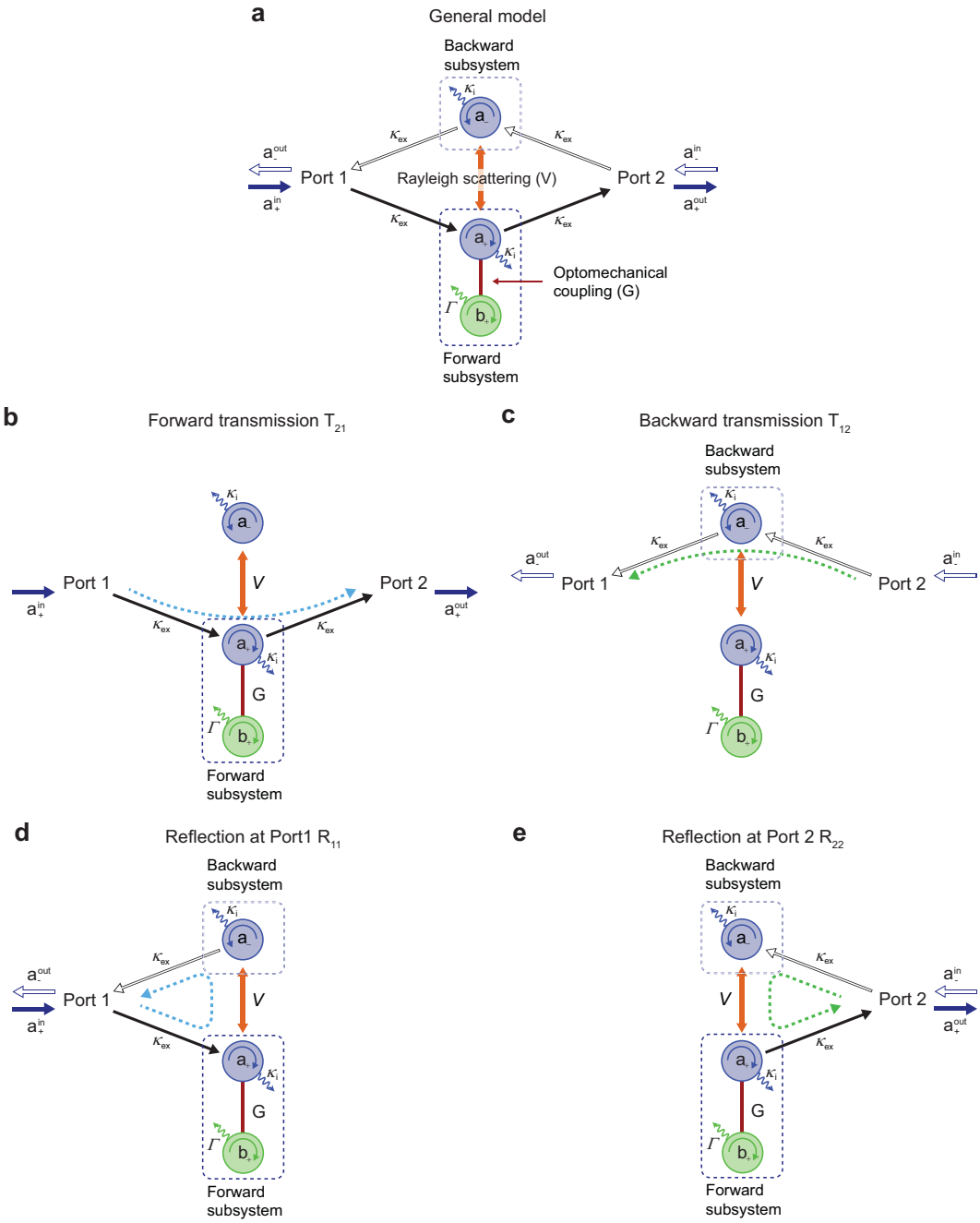

Figure 6.2: Toy model for transmission and reflection coefficients. **(a)** Our system can be described through a two-port system picture, as described in the main manuscript, where each port indicates the left or right ends of the waveguide. Using this, we can describe **(b)** the forward transmission coefficient (T_{21}), **(c)** the backward transmission coefficient (T_{12}), **(d)** the reflection coefficient at Port 1 (R_{11}), and **(e)** the reflection coefficient at Port 2 (R_{22}). The two reflection coefficients R_{11} and R_{22} must be always identical since the interaction takes place through both forward and backward subsystems.

6.3.1 Waveguide transmission and reflection coefficients

To experimentally investigate the optomechanical modification of Rayleigh backscattering within the resonator, we can perform measurements of the transmission and reflection coefficients through the side-coupled waveguide. Since we are interested in the stationary solutions of Eqns. 6.1, we can neglect the vacuum and thermal noise in our calculation. The steady state intracavity field solutions $\bar{a}_+$ and $\bar{a}_-$ excited by both forward and backward probe fields are obtained as follows :

$$\bar{a}_+ = \frac{\sqrt{k_{\rm ex}}a_+^{\rm in} - \dfrac{iV(\Gamma/2+i\Delta_b)\sqrt{\kappa_{\rm ex}}a_-^{\rm in}}{(\kappa/2+i\Delta_a)(\Gamma/2+i\Delta_b)+\eta^2G^2}}{\dfrac{\kappa}{2}+i\Delta_a+\dfrac{G^2}{\Gamma/2+i\Delta_b}+\dfrac{V^2(\Gamma/2+i\Delta_b)}{(\kappa/2+i\Delta_a)(\Gamma/2+i\Delta_b)+\eta^2G^2}}, \tag{6.2a}$$

$$\bar{a}_- = \frac{\sqrt{k_{\rm ex}}a_-^{\rm in} - \dfrac{iV(\Gamma/2+i\Delta_b)\sqrt{\kappa_{\rm ex}}a_+^{\rm in}}{(\kappa/2+i\Delta_a)(\Gamma/2+i\Delta_b)+G^2}}{\dfrac{\kappa}{2}+i\Delta_a+\dfrac{\eta^2G^2}{\Gamma/2+i\Delta_b}+\dfrac{V^2(\Gamma/2+i\Delta_b)}{(\kappa/2+i\Delta_a)(\Gamma/2+i\Delta_b)+G^2}}. \tag{6.2b}$$

The above expressions show that the cavity modes can be populated by both forward and backward optical probes, due to the Rayleigh backscattering. Using the resonator input-output formalism, we now can obtain expressions for the output fields in the waveguide (Fig. 6.3).

1. for cw transmission $a_+^{\rm out}\big|_{a_-^{\rm in}=0} = a_+^{\rm in} - \sqrt{\kappa_{\rm ex}}\,\bar{a}_+\big|_{a_-^{\rm in}=0}$
2. for ccw transmission $a_-^{\rm out}\big|_{a_+^{\rm in}=0} = a_-^{\rm in} - \sqrt{\kappa_{\rm ex}}\,\bar{a}_-\big|_{a_+^{\rm in}=0}$
3. for cw $\rightarrow$ ccw reflection $a_-^{\rm out}\big|_{a_-^{\rm in}=0} = -\sqrt{\kappa_{\rm ex}}\,\bar{a}_-\big|_{a_-^{\rm in}=0}$
4. for ccw $\rightarrow$ cw reflection $a_+^{\rm out}\big|_{a_+^{\rm in}=0} = -\sqrt{\kappa_{\rm ex}}\,\bar{a}_+\big|_{a_+^{\rm in}=0}$

The above expressions allow us to derive the waveguide transmission and re-

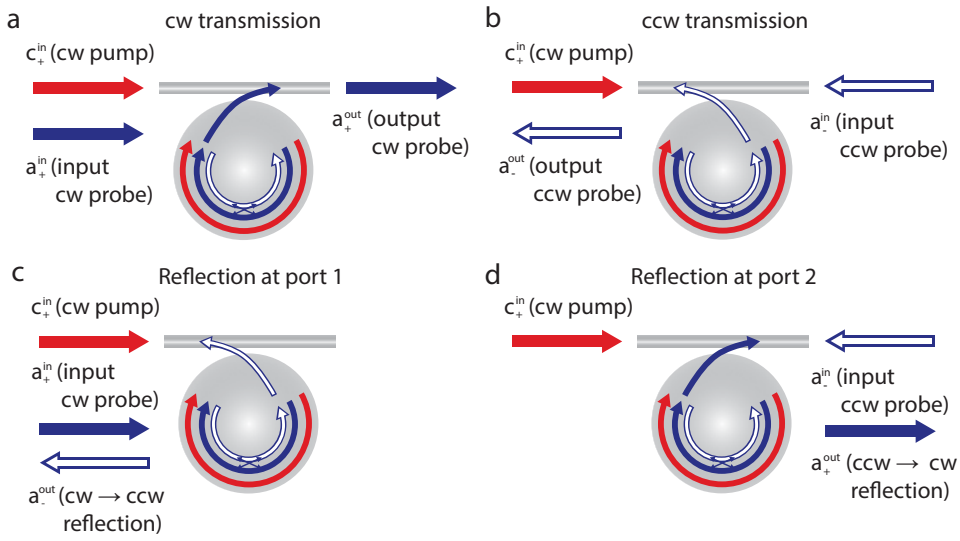

Figure 6.3: Variable descriptions for transmission and reflection measurement. For cw optical pumping into the c_+ mode, we can define **(a)** forward transmission, **(b)** backward transmission, **(c)** reflection of the input cw probe a_+^{in} within the probe optical modes $a_\pm$, and **(d)** reflection of the input ccw probe a_-^{in} within the probe optical modes $a_\pm$. As explained in Fig. 6.2d and 6.2e the reflections identified in (c) and (d) must be identical.

flection coefficients as follows :

$$T_{21} = \left.\frac{a_+^{\text{out}}}{a_+^{\text{in}}}\right|_{a_-^{\text{in}}=0} = 1 - \frac{\kappa_{\text{ex}}}{\frac{\kappa}{2} + i\Delta_a + \frac{G^2}{\Gamma/2 + i\Delta_b} + \frac{V^2(\Gamma/2 + i\Delta_b)}{(\kappa/2 + i\Delta_a)(\Gamma/2 + i\Delta_b) + \eta^2 G^2}}, \tag{6.3a}$$

$$T_{12} = \left.\frac{a_-^{\text{out}}}{a_-^{\text{in}}}\right|_{a_+^{\text{in}}=0} = 1 - \frac{\kappa_{\text{ex}}}{\frac{\kappa}{2} + i\Delta_a + \frac{V^2}{\kappa/2 + i\Delta_a + G^2/(\Gamma/2 + i\Delta_b)} + \frac{\eta^2 G^2}{\Gamma/2 + i\Delta_b}}, \tag{6.3b}$$

$$R = \left.\frac{a_-^{\text{out}}}{a_+^{\text{in}}}\right|_{a_-^{\text{in}}=0} = \left.\frac{a_+^{\text{out}}}{a_-^{\text{in}}}\right|_{a_+^{\text{in}}=0} = \frac{\frac{iV\kappa_{\text{ex}}}{\kappa/2 + i\Delta_a + G^2/(\Gamma/2 + i\Delta_b)}}{\frac{\kappa}{2} + i\Delta_a + \frac{V^2}{\kappa/2 + i\Delta_a + G^2/(\Gamma/2 + i\Delta_b)} + \frac{\eta^2 G^2}{\Gamma/2 + i\Delta_b}}. \tag{6.3c}$$

We can also consider the case where there is no backscattering of the pump,

i.e. $\eta = 0$, which results in the simplified equations :

$$T_{21} = \left.\frac{a_+^{\text{out}}}{a_+^{\text{in}}}\right|_{a_-^{\text{in}}=0} = 1 - \frac{\kappa_{\text{ex}}}{\dfrac{\kappa}{2} + i\Delta_a + \dfrac{G^2}{\Gamma/2 + i\Delta_b} + \dfrac{V^2}{\kappa/2 + i\Delta_a}} \tag{6.4a}$$

$$T_{12} = \left.\frac{a_-^{\text{out}}}{a_-^{\text{in}}}\right|_{a_+^{\text{in}}=0} = 1 - \frac{\kappa_{\text{ex}}}{\dfrac{\kappa}{2} + i\Delta_a + \dfrac{V^2}{\kappa/2 + i\Delta_a + G^2/(\Gamma/2 + i\Delta_b)}} \tag{6.4b}$$

$$R = \left.\frac{a_-^{\text{out}}}{a_+^{\text{in}}}\right|_{a_-^{\text{in}}=0} = \left.\frac{a_+^{\text{out}}}{a_-^{\text{in}}}\right|_{a_+^{\text{in}}=0} = \frac{\dfrac{iV\kappa_{\text{ex}}}{\kappa/2 + i\Delta_a + G^2/(\Gamma/2 + i\Delta_b)}}{\dfrac{\kappa}{2} + i\Delta_a + \dfrac{V^2}{\kappa/2 + i\Delta_a + G^2/(\Gamma/2 + i\Delta_b)}} \tag{6.4c}$$

Finally, we can also produce a scattering matrix formalism for the the optical probe transmission and reflection coefficients, that incorporates simultaneous inputs from both directions in the waveguide:

$$\begin{pmatrix} a_-^{\text{out}} \\ a_+^{\text{out}} \end{pmatrix} = \begin{pmatrix} R_{11} & T_{12} \\ T_{21} & R_{22} \end{pmatrix} \begin{pmatrix} a_+^{\text{in}} \\ a_-^{\text{in}} \end{pmatrix} \tag{6.5}$$

Here we see that the scattering matrix is generally non-symmetric, i.e. $T_{12} \neq T_{21}$, when the optomechanical coupling is non-zero. This non-reciprocity of transmission coefficients induced through Brillouin scattering has been already reported [18, 19].

6.3.2 Effective optical loss rate

Optical loss due to Rayleigh backscattering is typically included as a part of the intrinsic loss in whispering gallery resonators, since it cannot be distinguished from absorption losses at low scattering rates. In this work, however, we must explicitly distinguish the optical loss due to Rayleigh backscattering from other intrinsic optical losses. To quantify the optical loss, we first focus on the susceptibilities for the

$a_\pm$ modes using Eqs. 6.1. Solving in the Fourier domain, we obtain

$$\begin{aligned}\chi_{a_+}^{-1}(\omega) &= -i(\omega-\Delta_a)+\kappa/2 \\ &+ \frac{G^2}{-i(\omega-\Delta_b)+\Gamma/2} \\ &+ \frac{V^2(-i(\omega-\Delta_b)+\Gamma/2)}{(-i(\omega-\Delta_a)+\kappa/2)(-i(\omega-\Delta_b)+\Gamma/2)+\eta^2G^2}, \text{ and} \end{aligned} \tag{6.6a}$$

$$\begin{aligned}\chi_{a_-}^{-1}(\omega) &= -i(\omega-\Delta_a)+\kappa/2 \\ &+ \frac{\eta^2G^2}{-i(\omega-\Delta_a)+\Gamma/2} \\ &+ \frac{V^2\left(-i(\omega-\Delta_b)+\Gamma/2\right)}{\left(-i(\omega-\Delta_a)+\kappa/2\right)\left(-i(\omega-\Delta_b)+\Gamma/2\right)+G^2}. \end{aligned} \tag{6.6b}$$

The effective optical loss, including the loss due to Rayleigh scattering and optomechanical coupling, can be extracted from real part of the optical susceptibilities. At zero detuning i.e $\Delta_a = 0$ and $\Delta_b = 0$, the total effective optical loss rates of the $a_\pm$ modes (including waveguide loading) are given by:

$$\kappa_{\text{eff}}^{+} = \kappa\left(1+\mathcal{C}\right) + \frac{4V^2}{\kappa(1+\eta^2\mathcal{C})}, \tag{6.7a}$$

$$\kappa_{\text{eff}}^{-} = \kappa(1+\eta^2\mathcal{C}) + \frac{4V^2}{\kappa(1+\mathcal{C})}. \tag{6.7b}$$

where we define optomechanical cooperativity as $\mathcal{C} = 4G^2/\kappa\Gamma$. If the pump reflection (η) is small, we see that the effective loss rate of the a_+ mode increases with increasing $\mathcal{C}$ in Eq. (6.7a), which corresponds to the results of the optomechanically induced transparency [116, 115, 18]. Meanwhile the second term in Eq. (6.7b) decreases with increasing $\mathcal{C}$. This analysis reveals that the Rayleigh backscattering contribution is effectively shut down in the limit of large $\mathcal{C}$.

6.3.3 Redefining the condition for critical coupling

For conventional resonator-waveguide systems, the transmission through the waveguide in either direction is given by

$$T = \frac{(\kappa - 2\kappa_{\text{ex}})/2 + i\Delta}{\kappa/2 + i\Delta}$$

which can be derived by setting $G =$ and $V = 0$ in Eqn. 6.3a. Critical coupling, the point where on-resonance ($\Delta = 0$) transmission dips to zero in conventional resonator systems is achieved when $\kappa_{\rm ex} = \kappa/2$. However this condition for achieving critical coupling must be modified in our system. For probing of the ccw optical mode (backward direction), we can rewrite the transmission coefficient at zero detuning ($\Delta_a = 0$ and $\Delta_b = 0$) as described in Eqn. 6.3b:

$$T_{12} = \frac{\kappa_{\rm eff}^{-} - 2\kappa_{\rm ex}}{\kappa_{\rm eff}^{-}} = \frac{\kappa(1+\eta^2\mathcal{C}) + 4V^2/\kappa(1+\mathcal{C}) - 2\kappa_{\rm ex}}{\kappa(1+\eta^2\mathcal{C}) + 4V^2/\kappa(1+\mathcal{C})} \tag{6.8}$$

In other words, the external coupling rate needed to reach critical coupling of the ccw a_- mode with the waveguide should be modified to the following :

$$\kappa_{\rm ex} = \frac{\kappa_{\rm eff}^{-}}{2} = \frac{\kappa(1+\eta^2\mathcal{C})}{2} + \frac{2V^2}{\kappa(1+\mathcal{C})} \tag{6.9}$$

6.3.4 Evolution of transmission and reflection coefficients

In Figure 6.4 we invoke the model of Eqns. 6.4 to predict the evolution of transmission and reflection coefficients as a function of optomechanical coupling rate and the optical probe detuning. We have modeled an undercoupled situation, i.e. where the effective intrinsic loss rate of the optical modes is greater than the extrinsic loss under zero optomechanical coupling [47, 175], to correspond with the experiments presented in the main text.

For $G = 0$ the model simply predicts the Rayleigh-scattering induced doublet of the hybridized optical modes. When we engage the unidirectional cw pump (i.e. $G \neq 0$), the forward transmission model T_{21} reveals that a_+ undergoes normal mode splitting caused by optomechanical coupling with the b_+ mechanical mode. Here, the forward transmission T_{21} becomes the optomechanical normal mode splitting, as the optomechanical coupling G is increased(See Fig. 6.4) [176]. That is because the eigenmodes of the forward optomechanical system are hybrids of the a_+ and b_+ modes. Intuitively, we anticipate that the reflection coefficient for the photons in the resonator should be reduced since the lowered photonic susceptibility of the forward subsystem 'open circuits' the reflection pathway mediated by Rayleigh scattering. The reflection coefficient produced by the model agrees with this intuitive

assertion. More importantly, the backward transmission coefficient T_{12} shows that the linewidth of the time-reversed mode a_- narrows when G increases, indicating that the intrinsic optical loss rate for that mode is reduced (see §6.3.2). A better confirmation of this reduction of intrinsic loss comes from the fact that the a_- mode approaches critical coupling (zero on-resonance transmission, see §6.3.3) as

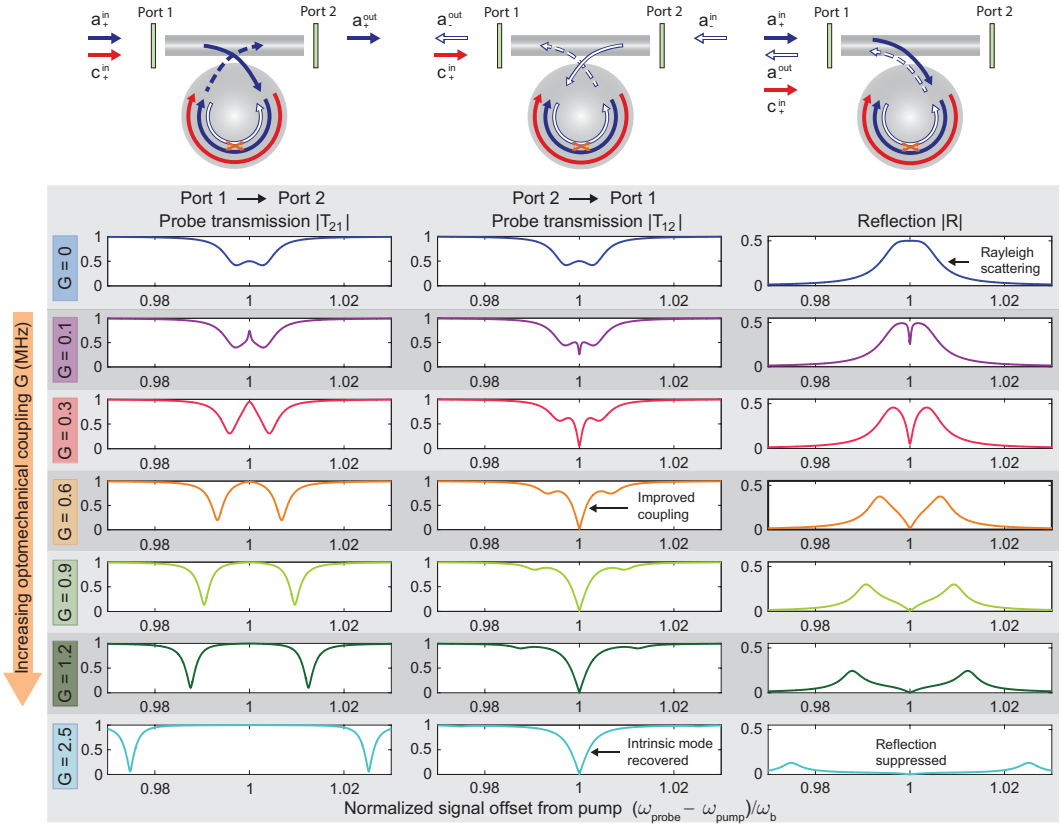

Figure 6.4: Theoretical prediction of backscattering suppression. We model the waveguide transmission and reflection coefficients (Eqns. 6.4) for varying optomechanical coupling rate G. The model parameters are $\kappa = 0.7$ MHz, $\kappa_{ex} = 0.35$ MHz, $\Gamma = 30$ kHz, and $V = 0.35$ MHz to correspond closely with experiments below. Without any optomechanical coupling ($G = 0$), as is typical, the $a_\pm$ modes exhibit the Rayleigh scattering induced doublet and produce identical waveguide transmission coefficients in both directions. Additionally, the resonant Rayleigh backscattering produces a large back-reflection coefficient. Since the effective optical loss for $G = 0$ is $\kappa_{eff}^{\pm} = \kappa + 4V^2/\kappa = 1.4$ MHz (see Eqns. 6.7) the system is initially overcoupled at its resonance. However, as G is increased, the time-reversal symmetry of the cw/ccw modes is broken, which can be observed through the strong distinction of transmission coefficients. The resulting suppression of Rayleigh backscattering can be seen in both the reduced reflection coefficient, as well as the improved coupling of the ccw resonator mode in the backward direction (reduced intrinsic loss).

the intrinsic loss approaches the extrinsic loss κ_{ex}.

6.3.5 Condition for reaching a quantum point

It is also interesting to calculate the effective temperature of the a_- optical mode due to Rayleigh backscattering. We assume $\eta = 0$ for simplifying the equations of motion, and obtain the equations in the Fourier domain:

$$-i\omega\tilde{a}_+ = -\frac{\kappa}{2}\tilde{a}_+ - iG\tilde{b}_+ - iV\tilde{a}_- + \sqrt{\kappa_i}\tilde{a}_{\mathrm{vac}}(\omega) \tag{6.10a}$$

$$-i\omega\tilde{b}_+ = -\frac{\Gamma}{2}\tilde{b}_+ - iG^*\tilde{a}_+ + \sqrt{\Gamma}\tilde{b}_{\mathrm{th}}(\omega) \tag{6.10b}$$

$$-i\omega\tilde{a}_- = -\frac{\kappa}{2}\tilde{a}_- - iV\tilde{a}_+ + \sqrt{\kappa_i}\tilde{a}_{\mathrm{vac}}(\omega) \tag{6.10c}$$

We note that optical noise for the $a_\pm$ modes is negligible due to the negligible thermal excitation of photons. In our system, the additional thermal load on the a_+ mode is $-iG\sqrt{\Gamma}\tilde{b}_{\mathrm{th}}/(\Gamma/2 - i\omega)$ due to the optomechanical interaction. This thermal noise on the a_+ mode excited by the pump is in turn loaded to its degenerate mode a_- through the Rayleigh backscattering channel. Therefore the effective photon occupation of the a_- mode due to the pump in the cw direction becomes:

$$N_{th} = \frac{4\mathcal{C}V^2}{\kappa^2(1+\mathcal{C})^2} n_{th} \tag{6.11}$$

where n_{th} is the phonon occupation number at operation temperature, in this case at room temperature. Consequently, quantum optical effects should be observable for very large optomechanical cooperativity, in the regime $\mathcal{C} > 2n_{th}V^2/\kappa^2$.

6.3.6 Normal modes without pump backscattering (two-mode split)

The optomechanical hybridization of the optical mode a_+ and mechanical mode b_+ can be seen in either the mechanical or optical spectra. Optical frequency measurement of the normal modes in the strong coupling regime was presented in the main text Fig. 4. These normal modes are also observable through the mechan-

ical spectrum, which is presented through pump scattering measurements [21] in Fig. 6.5a. To model this system, we chose a frame rotating with the pump laser frequency ω_{pump}, i.e. we re-write $a_+ = a_+ e^{-i\omega_{\text{pump}} t}$, to obtain the mechanical frequency normal modes. As we will show later, the pump backscattering factor η in this experiment is small enough so as to be negligible. We can thus rewrite the equations of motion for the cw modes Eqns. 6.1 in matrix form as follows:

$$\frac{d}{dt}\begin{bmatrix} a_+ \\ b_+ \end{bmatrix} = -i\begin{bmatrix} -i\dfrac{\kappa + 4V^2/\kappa}{2} + (\omega_a - \omega_{\text{pump}}) & G \\ G^* & -i\dfrac{\Gamma}{2} + \omega_b \end{bmatrix}\begin{bmatrix} a_+ \\ b_+ \end{bmatrix} \tag{6.12}$$

where $\kappa + 4V^2/\kappa$ is the combined optical loss rate including the loss contribution from Rayleigh backscattering into mode a_-. The eigenvalues for the matrix in

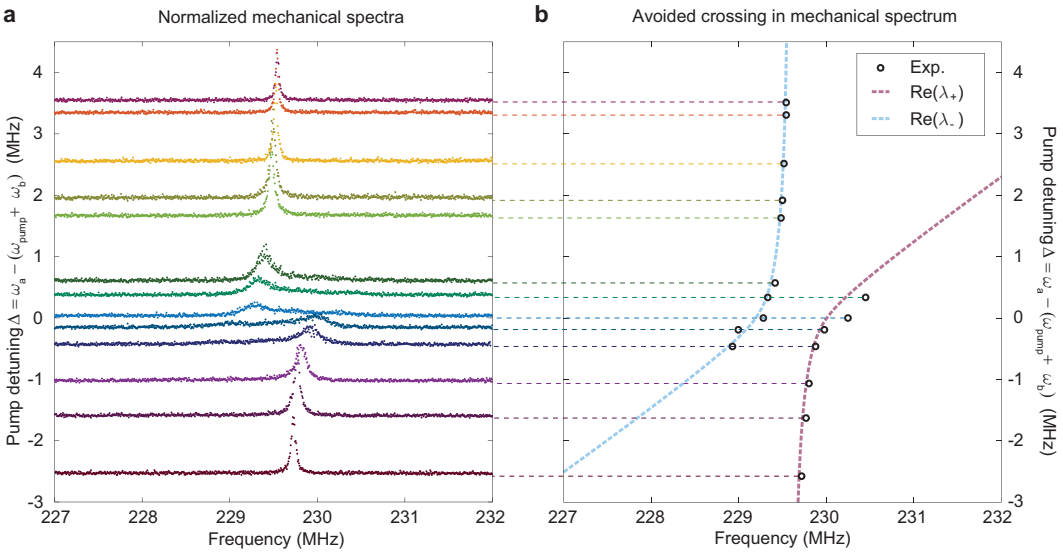

Figure 6.5: Normal mode splitting with negligible pump backscattering. (a) We measure the mechanical spectrum through homodyne detection of the beating of the pump and scattered light. The two normal modes resulting from coupling of the a_+ optical and b_+ mechanical modes can be readily seen. This experimental measurement of mechanical spectra corresponds to Fig. 4 in the main text. **(b)** The experimentally measured normal mode frequencies are compared against he theoretical curves of Eqn. 6.13. Additional details are provided in the text.

Eqn. 6.12 are evaluated as :

$$\lambda_{\pm} = -i\frac{\kappa + 4V^2/\kappa + \Gamma}{4} + \frac{\omega_a + \omega_b - \omega_{\text{pump}}}{2} \pm \frac{1}{2}\sqrt{4G^2 + \left[\Delta^2 + i\left(\frac{\Gamma}{2} - \frac{\kappa + 4V^2/\kappa}{2}\right)\right]^2} \tag{6.13}$$

Here $\Delta = (\omega_a - \omega_b) - \omega_{\text{pump}}$ is the pump laser detuning that we also define in the main text. We can now obtain the normal mode frequencies by taking the real parts of the eigenvalues in Eqn. 6.13. Figure 6.5b compares the experimental data to the theoretical prediction from this analysis. The dots represent the measured peak frequencies for each normal mode in Fig. 6.5a. The blue and red curves show the theoretical prediction based on Eqn. 6.13 for the given parameters $G = 0.5$ MHz, $\kappa = 0.59$ MHz, $V = 0.3$ MHz, $\omega_b = 229.6$ MHz and $\Gamma = 39.1$ kHz, which are extracted from Fig. 4 in the main text.

The experimental results presented in Fig. 6.5 show only two normal-modes in the mechanical domain, corresponding to coupling of the cw a_+ optical mode with the cw b_+ mechanical mode. As we show next, this assures us that there is negligible ccw optomechanical interaction due to backscattering of the pump.

6.3.7 Normal modes including pump backscattering (four-mode split)

We can now also examine the corrections to the normal mode splitting that arise if pump backscattering is not negligible. Once again, we use the pump frequency ω_{pump} as reference, and rewrite the more general equations of motion (Eqn. 6.1) in matrix form.

$$\frac{d}{dt}\begin{bmatrix} a_+ \\ b_+ \\ a_- \\ b_- \end{bmatrix} = -i\begin{bmatrix} -i\frac{\kappa}{2} + \Delta_a & G & V & 0 \\ G^* & -i\frac{\Gamma}{2} + \omega_b & 0 & 0 \\ V & 0 & -i\frac{\kappa}{2} + \Delta_a & -i\eta G \\ 0 & 0 & i\eta G^* & -i\frac{\Gamma}{2} + \omega_b \end{bmatrix}\begin{bmatrix} a_+ \\ b_+ \\ a_- \\ b_- \end{bmatrix} \tag{6.14}$$

The coupling terms of the matrix in Eqn. 6.14 imply that this system will have four normal modes. The spectra of these normal modes can be observed using the mechanical spectrum Fig. 6.6a. In Fig. 6.6b we present the analytical eigenvalue curves for the four normal modes based on Eqn. 6.14, using the parameters

$(\kappa, G, V, \omega_b, \eta, \Gamma) = (0.6$ MHz, 0.4 MHz, 0.85 MHz, 115.03 MHz, 0.7, 10 kHz) that correspond to this experiment. We have specifically avoided such cases in the experiment that we present in the main text, so as to have a clean determination of how cw pump induced time-reversal symmetry breaking affects only the $a_\pm$ modes.

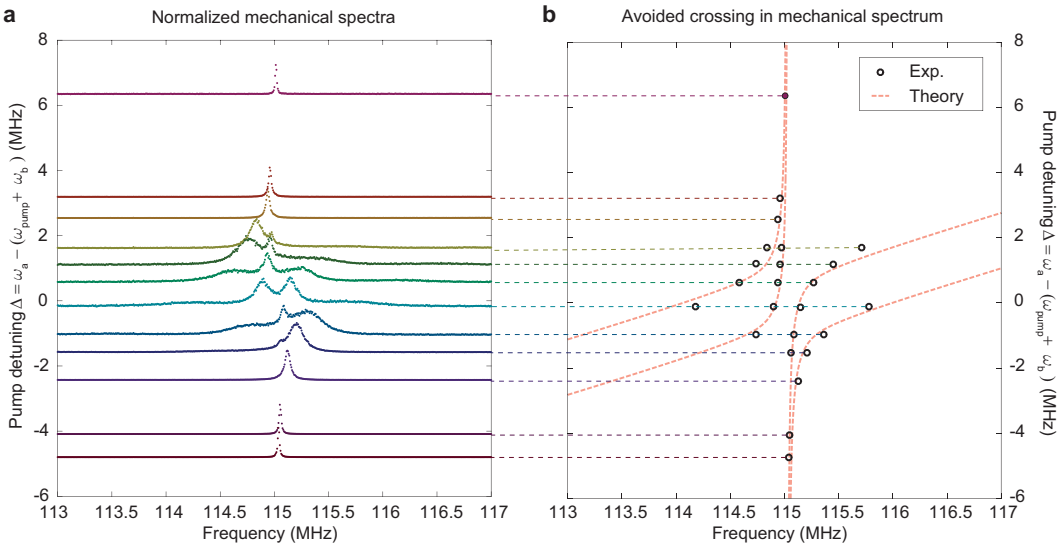

Figure 6.6: Normal mode splitting with appreciable pump backscattering. **(a)** In this case, the mechanical spectra show four normal modes, produced by the optomechanical coupling of $a_\pm$ with their corresponding $b_\pm$, and through the Rayleigh scattering induced coupling of $a_\pm$. **(b)** The experimentally measured normal mode frequencies are compared against the theoretical curves of Eqn. 6.14. Additional details are provided in the text.

6.4 Simplified model for suppression of Rayleigh scattering

The simplified model Hamiltonian for this system includes both Rayleigh backscattering and the optomechanical interaction as follows:

$$H_{\rm int} = \hbar(G a_+^\dagger b_+ + G^* a_+ b_+^\dagger) + \hbar V(a_+^\dagger a_- + a_-^\dagger a_+) \ . \tag{6.15}$$

Here, V is the Rayleigh backscattering induced coupling rate between the $a_\pm$ modes, while $G = g_o\sqrt{n_{c+}}$ is the pump-enhanced clockwise-only optomechanical coupling rate between the a_+ optical mode and the b_+ mechanical mode. g_o represents the single photon optomechanical coupling rate, and n_{c+} represents the average number

of intracavity photons in the c_+ mode. Since no ccw pump is applied to the system, an optomechanical interaction between a_- and b_- need not be considered. A detailed analysis presented in Section 6.3 additionally incorporates the effects of disorder-induced backscattering within the pump modes $c_\pm$, which can be distinct from the Rayleigh coupling between $a_\pm$ due to differences of modeshape and polarization. However as we show in Section 6.3.6 - 6.3.7, there is no evidence for this additional scattering effect within the pump modes, in the experiments that we discuss in this paper.

Fig. 6.1d presents a toy model of the system, in which we explicitly distinguish between forward and backward subsystems. The degenerate optical modes $a_\pm$ are modeled with intrinsic loss rate κ_i, which includes all absorption and scattering mechanisms that leak light out of the mode, but excludes the influence of the backscattering channel V. These modes $a_\pm$ couple to the waveguide with an extrinsic coupling rate defined by κ_{ex} that is symmetric in both forward and backward directions. For light propagating in the waveguide from Port 1 $\rightarrow$ Port 2 (forward direction), the interaction with the resonator occurs through the forward subsystem described as the optomechanically coupled a_+ optical and b_+ mechanical modes. Conversely, for light propagating from Port 2 $\rightarrow$ Port 1 (backward direction), light primarily interacts with the a_- optical mode. Due to the different optical susceptibility of the forward and backward subsystems for any non-zero optomechanical coupling, the system exhibits broken time-reversal symmetry for transmission measurements. For reflections to take place in this system, i.e., Port 1 $\rightarrow$ Port 1, or Port 2 $\rightarrow$ Port 2, light must interact in series with both the forward and backward subsystems while passing through the Rayleigh backscattering channel (see illustration in Fig. 6.2). Thus, the reflection coefficients measured at each port are necessarily identical.

We can analytically obtain the waveguide transmission coefficients (T_{21} in the forward direction, T_{12} in the backward direction) and reflection coefficients at each port ($R_{11} = R_{22} = R$) using the Heisenberg-Langevin equations for motion for this system in the rotating wave approximation (Section 6.3). In any side coupled resonator-waveguide system, the total optical loss rate κ is defined by both the extrinsic losses (from waveguide loading) and intrinsic losses through the expression $\kappa = \kappa_i + \kappa_{\text{ex}}$. The condition for 'critical coupling' – defined as the point where on-resonance transmission reaches zero – can be derived as $\kappa = 2\kappa_{\text{ex}}$. Typically, this situation occurs when the intrinsic coupling rate κ_{ex} and the intrinsic loss rate

κ_i are matched. However in the case where both Rayleigh backscattering V and the optomechanical coupling G are acting on the modes (Fig. 6.1d), the optical loss rates for the $a_\pm$ modes are no longer identical and the critical coupling conditions must also change. In the simplest case in which all fields are on-resonance, the total effective loss rates for the $a_\pm$ modes can be evaluated as (details in Section 6.3.2) :

$$\kappa_{\text{eff}}^{+} = \kappa\,(1+\mathcal{C}) + \frac{4V^2}{\kappa} \tag{6.16a}$$

$$\kappa_{\text{eff}}^{-} = \kappa + \frac{4V^2}{\kappa(1+\mathcal{C})}\ . \tag{6.16b}$$

Here we have introduced $\mathcal{C} = 4G^2/\kappa\Gamma$ as the optomechanical cooperativity. These expressions show that even if $\mathcal{C} = 0$ the Rayleigh backscattering introduces additional intrinsic optical loss of $4V^2/\kappa$ to each mode, a loss channel formed through the counterpropagating mode. Moreover, we can see that as the optomechanical coupling rate is increased in the cw direction, light on-resonance in the *ccw* mode experiences a reduction in optical loss (κ_{eff}^{-} reduces) as an indirect effect. In the limit of large optomechanical coupling $\mathcal{C} \to \infty$ the optical loss in the ccw mode approaches κ, i.e., the effective intrinsic loss $\kappa_{\text{eff}}^{-} - \kappa_{\text{ex}}$ approaches the purely intrinsic loss rate κ_i. In this case the reflection should also approach zero since no backscattering occurs.

6.5 Results

In order to test the predictions of the theoretical model, we perform a series of experiments using silica microsphere WGRs. In our first experiment with a 90 μm radius resonator, the BSIT interaction is mediated by a mechanical whispering gallery mode of frequency $\omega_b = 116.3$ MHz, having azimuthal order M = 17 around the resonator equator (corresponding to phonon wavenumber $0.030\,\mu m^{-1}$) and mechanical damping rate $\Gamma = (14.4 \pm 0.2)$ kHz. Experimental measurements of the optical doublet (normal mode splitting) resulting from Rayleigh backscattering in this device, without any optomechanical influence, were previously shown in Fig. 6.1b. The pump (for controlling G) and probe (to observe $a_\pm$) are produced using a 1550 nm tunable external cavity diode laser and are evanescently coupled to the optical modes using a tapered fiber waveguide as illustrated in Fig. 6.1a. Further details on the

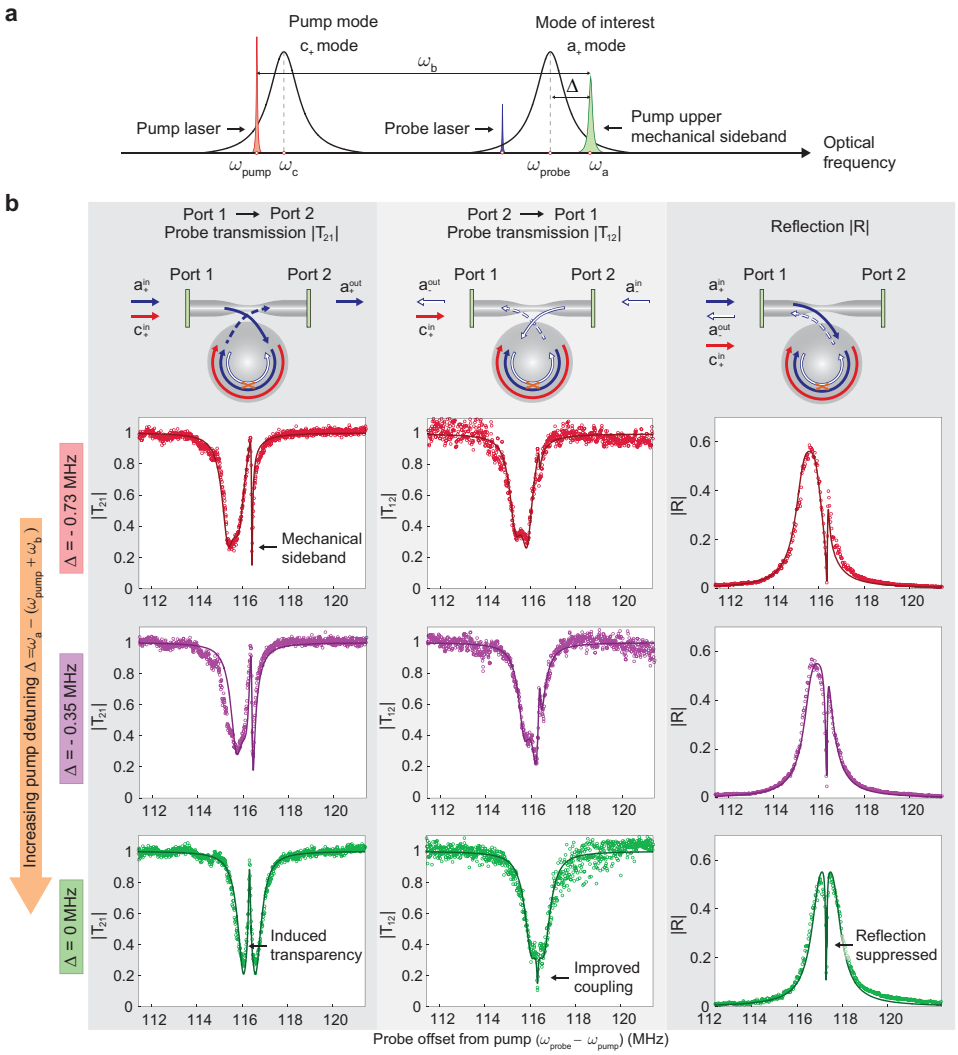

Figure 6.7: Demonstration of dynamic optomechanical suppression of Rayleigh backscattering. **(a)** General configuration of optical pump, probe, and mechanical sidebands with respect to the c_+ and a_+ optical modes in the cw direction – used throughout this work. **(b)** This experiment uses a 116 MHz mechanical mode in a 90 μm radius silica WGR. The Rayleigh scattering induced doublet is readily observed in probing of the $a_\pm$ optical modes for an off-resonance pump. As the pump is brought on resonance, the Brillouin scattering induced transparency is generated for the cw mode only (its on-resonance susceptibility is reduced), which breaks time-reversal symmetry within the bandwidth of the $a_\pm$ modes. Observations confirm two key predictions of the model – reduced optical reflection and improved coupling of the a_- mode to the waveguide – both confirming the suppression of Rayleigh backscattering within the WGR. Solid lines are simultaneous fits to the theoretical model. The reflection is very large due to resonant enhancement.

experimental setup and calibration of the transmission and reflection coefficients are provided in Section 3.3. In Fig. 6.7 we present the measured transmission and reflection coefficients vs relative detuning $\Delta = \omega_a - (\omega_{\text{pump}} + \omega_b)$ between the a_+ optical mode and the pump laser anti-Stokes mechanical sideband. The BSIT transparency window in the forward subsystem can be clearly observed as the relative detuning Δ approaches zero. Simultaneous measurements of the backward subsystem – a direction in which no pumping is performed – show that the a_- mode moves closer to critical coupling within the bandwidth of the non-reciprocal effect. Measurements of the reflection coefficient $|R|$ independently confirm the suppression of Rayleigh backscattering within the WGR. The detailed model presented in Section 6.3.2 allows extraction of the intrinsic optical loss rate $\kappa_i = (0.35 \pm 0.03)$ MHz, the extrinsic optical loss rate $\kappa_{\text{ex}} = (0.54 \pm 0.01)$ MHz (the optical mode is over-coupled), the Rayleigh backscattering rate $V = (0.34 \pm 0.01)$ MHz, for this experiment by means of simultaneous fitting of all the measured traces. At resonance ($\Delta = 0$ MHz) we estimate $G = (0.17 \pm 0.01)$ MHz with an intracavity (pump) occupation number of $n_{c+} \simeq 1 \times 10^{10}$ and single photon optomechanical coupling rate $g_o = (1.6 \pm 0.09)$ Hz. All uncertainties in this manuscript correspond to 95 % confidence intervals of the fitted value.

To explore near-complete suppression of Rayleigh backscattering, we performed a second experiment on a 101 μm radius resonator (Fig. 6.8), mediated by a 229.5 MHz mechanical mode having azimuthal order M = 39 (corresponding to phonon wavenumber $0.062\,\mu m^{-1}$) and damping rate $\Gamma = (39.1 \pm 1.3)$ kHz. Here, we used higher pump power to bring the system into the normal-mode coupling regime [20, 172], where the optomechanical coupling exceeds the total optical loss rate ($G \geq \kappa/2$). We first detune the pump sufficiently so that the optomechanical coupling is negligible (Fig. 6.8a). The $a_\pm$ modes are seen to hybridize and exhibit the doublet characteristic as expected from Rayleigh backscattering within the resonator. Fitting to the theoretical model allows us to discern the backscattering strength at $V = (0.3 \pm 0.01)$ MHz, intrinsic loss $\kappa_i = (0.45 \pm 0.02)$ MHz, and extrinsic coupling for the experiment at $\kappa_{\text{ex}} = (0.17 \pm 0.003)$ MHz, all of which contribute to the measured lineshape. We now bring the cw pump laser on resonance ($\Delta = 0$ MHz) such that 272 μW optical power is absorbed into the resonator, leading to an estimated optomechanical coupling rate $G = (0.5 \pm 0.02)$ MHz. The resulting optomechanically induced normal mode splitting in the a_+ mode can be observed through forward

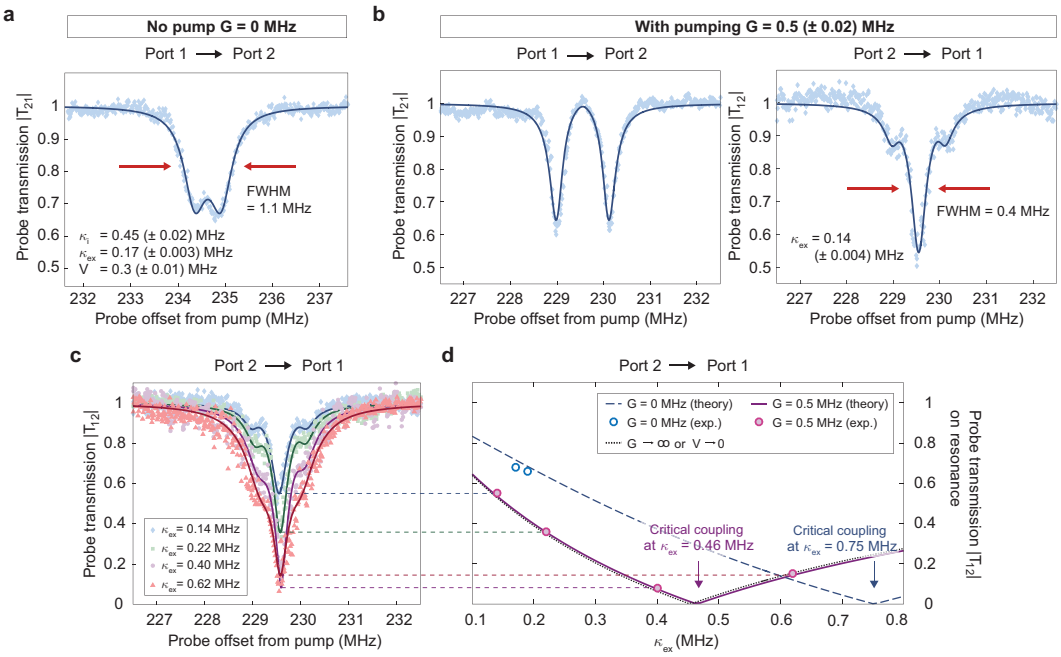

Figure 6.8: Near-complete suppression of Rayleigh backscattering. (a) This experiment was performed with a 229.5 MHz mechanical mode of a 101 μm radius silica WGR. By initially detuning the pump laser we are able to observe the Rayleigh backscattering induced optical doublet without optomechanical pumping. Fitting to the theoretical model (solid line) indicates intrinsic loss κ_i, extrinsic loss $\kappa_{\rm ex}$, and backscattering rate V. **(b)** We now tune the pump to obtain strong cw optomechanical coupling (with $G = 0.5$ MHz), resulting in prominent change of susceptibility for the cw (a_+) mode only. The time-reversed (a_-) mode, which we did not modify, simultaneously exhibits much narrower linewidth, and the scattering induced doublet is eliminated. **(c)** By adjusting the extrinsic coupling to the waveguide $\kappa_{\rm ex}$, we are able to explore the point of critical coupling for the ccw mode a_-. **(d)** The measured on-resonance transmission from experimental measurements in (c) are well matched to the theoretical predictions from the model (Eq. (6.8)). With zero optomechanical coupling the critical coupling point indicates intrinsic optical loss rate of 0.75 MHz. However, with optomechanical coupling of $G = 0.5$ MHz we estimate a ccw effective intrinsic loss rate of 0.46 MHz, a very close match to the purely intrinsic loss rate of 0.45 MHz.

transmission measurement (Fig. 6.8b-left). Since the TRS broken bandwidth now encompasses nearly the whole of the counter-propagating a_- mode, the backscattering is almost completely eliminated. Simultaneous measurement of backward transmission reveals that the Rayleigh backscattering induced doublet disappears in the a_- mode, and there is a significant improvement in its linewidth. Further, the on-resonance transmission dips lower indicating that coupling with the waveguide is closer to critical (Fig. 6.8b-right).

As discussed above (Eqn. 6.16b), in the limit of large optomechanical coupling the Rayleigh backscattering can be mitigated completely and the effective intrinsic loss of the ccw a_- mode must converge to its purely intrinsic loss rate $\kappa_i = 0.45$ MHz. In such a case, we would expect to see critical coupling in the waveguide-resonator system when extrinsic coupling $\kappa_{\text{ex}} = 0.45$ MHz. In fact, measurement of this critical coupling point is the only directly accessible measurement of the on-resonance intrinsic optical loss since the optical modeshape is non-Lorentzian. We test this complete suppression scenario by subsequently increasing the extrinsic waveguide-resonator coupling from 0.14 MHz to 0.62 MHz. Experimental measurements of the ccw mode in Fig. 6.8c and 6.8d show the evolution of the ccw resonance, as it proceeds from undercoupling to overcoupling while passing through the critical coupling point. Data for zero optomechanical coupling are well matched to the theoretical predictions, showing that critical coupling occurs at $\kappa_{\text{ex}} = 0.75$ MHz due to the increased intrinsic loss ($+4V^2/\kappa$) from the Rayleigh backscattering channel. On the other hand, $G = 0.5$ MHz data and theoretical prediction show that critical coupling must occur at $\kappa_{\text{ex}} \approx 0.46$ MHz. This is extremely close to the estimated intrinsic loss rate of $\kappa_i = 0.45$ MHz indicating that the TRS broken system achieves nearly complete suppression of the undesirable Rayleigh backscattering. As predicted by the theoretical model (Section 6.3.4) an even higher optomechanical coupling rate could push the 'optomechanical wings' further out, permitting recovery of the Lorentzian lineshape of the ccw optical mode.

6.6 Discussion

The approach that we demonstrate here for dynamic suppression of Rayleigh backscattering employs a local time-reversal symmetry breaking interaction, i.e., Brillouin scattering, that is available in all phases of matter. Due to the ubiquity of this effect, our system can in principle be unwrapped for linear waveguide systems as well, where immunity against unforeseen defects is highly desirable. For example, an optical waveguide could be made robust against backscattering from a damaged segment by suppressing the time-reversed photonic density of states through the optomechanical influence. More broadly, this principle of suppressing backscattering via TRS breaking may also be readily achieved through other local nonreciprocal techniques, encompassing nonlinear optics [22, 114], chirally pumped atoms [110], parity-time symmetry breaking [177, 109], and spatiotemporal modulation [106].

6.7 Summary

Disorder-induced Rayleigh scattering causes coupling between degenerate counter-propagating eigenmodes, limiting photon or phonon transport in systems having such modes. I have proposed approaches to mitigate Rayleigh scattering of both photons and phonons in these systems. I demonstrated that disorder-induced scattering can be suppressed if the susceptibility of degenerate modes is modified in a manner that breaks time-reversal symmetry. These approaches have been experimentally validated in photonic and phononic resonant devices using optomechanical interactions to break time-reversal symmetry.

Chapter 7

Alternative approaches to break time-reversal symmetry leading to suppression of backscattering

7.1 Introduction

In the previous chapters, I have discussed novel approaches to suppress disorder-induced scattering through a specific form of time-reversal symmetry breaking via Brillouin interaction in fused silica microsphere resonators. In this chapter, I would like to expand these techniques to various platforms such as on-chip waveguides and resonators through various time-reversal breaking methods.

7.2 Breaking time-reversal symmetry in linear waveguide systems

7.2.1 Motivation

[1]We theoretically propose Brillouin cooling in linear waveguides based on current designs through analysis of the conditions under which Brillouin cooling of phonons of both low and high group velocities. If the Brillouin gain in such a waveguide reaches the order of 10^5 $m^{-1}W^{-1}$, appreciable cooling of phonon modes may be observed with a modest pump power of a few mW. Fortunately, Otterstrom et al. have recently reported continuous-mode phonon cooling by leveraging a guided-wave optomechanical process [82] similar to our proposal below. This is clear evidence for achieving the reduction of disorder-induced backscattering in a linear waveguide through Brillouin interaction. Here, we first illustrate how Brillouin cooling would occur under two cases as follows by solving the three-coupled equations.

[1]Portions of this chapter are reprinted with permission from Chen, Y-C., Kim, S et al., (2016), "Brillouin cooling in a linear waveguide," New Journal of Physics, 18, 115004.

7.2.2 Coupled wave equations for anti-Stokes Brillouin scattering

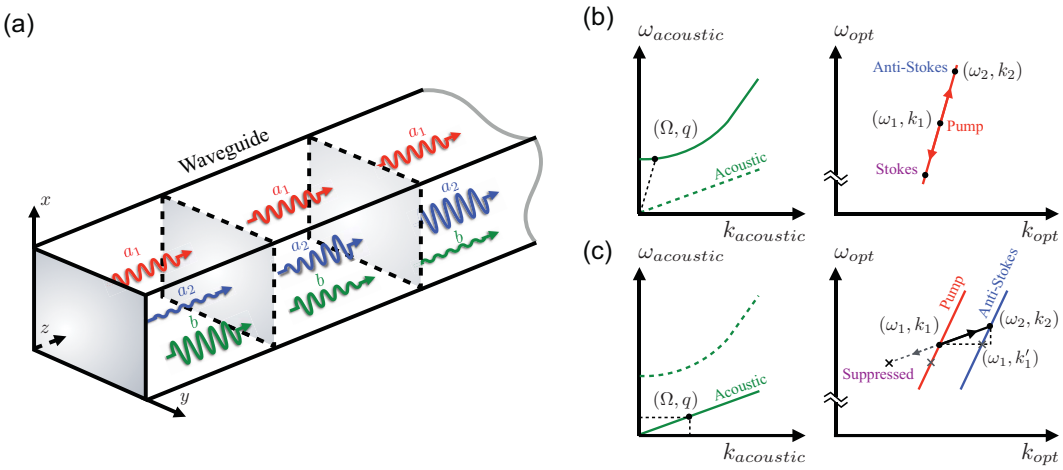

Figure 7.1: (a)Three wave mixing interaction in a linear waveguide. The waveguide is assumed to be infinitely extended in the z-direction. The pump field (ω_1, k_1), anti-Stokes field (ω_2, k_2), and the acoustic field (Ω, q) are described by their corresponding slowly varying field operators $a_1(z,t)$, $a_2(z,t)$, and $b(z,t)$, respectively. (b) Intra-modal scattering. In this case, the phonon in the process belongs to low group velocity guided-acoustic mode. Since there exists at least one phonon mode with frequency and momentum (ω, q) that matches the slope of the optical band, the Stokes process cannot be suppressed. (c) Inter-modal scattering. The phonon in the scattering process belongs to a mode family having large group velocity and appreciable momentum. If we excite the pump light only at the mode with momentum k_1, Stokes scattering is suppressed which potentially enables cooling if other required conditions are met. At the same time, we must avoid exciting the mode at k_1' which will lead to Stokes scattering with the same phonon mode.

Once process selection conditions are met, we can now consider the three-wave mixing process between a pump wave (ω_1, k_1), an anti-Stokes wave (ω_2, k_2), and an acoustic wave (Ω, q) in a linear waveguide. As shown in Fig. 7.1, the three waves are assumed to co-propagate in a waveguide infinitely extended in the z-direction for the forward scattering case. We consider here only the forward scattering case since the acoustic modes participating in backward scattering generally have greater frequency and thus lower Q-factor, which as we show later, are impractical to cool. The coupling equations for the fields inside a waveguide can be derived classically as demonstrated in [178] or quantum mechanically as in [179, 180]. Here we use the quantum description as it is more natural to introduce the Langevin noise operator that drives the acoustic field. Under the assumption that the process is perfectly

phase matched, the equations of motion for the field operators are given by [179, 180]

$$\frac{\partial a_1}{\partial t} + v_1 \frac{\partial a_1}{\partial z} = -\frac{\kappa_1}{2} a_1 - i\beta^* a_2 b^\dagger, \tag{7.1a}$$

$$\frac{\partial a_2}{\partial t} + v_2 \frac{\partial a_2}{\partial z} = -\frac{\kappa_2}{2} a_2 - i\beta a_1 b, \tag{7.1b}$$

$$\frac{\partial b}{\partial t} + v_b \frac{\partial b}{\partial z} = -\Gamma b - i\beta^* a_1^\dagger a_2 + \xi, \tag{7.1c}$$

where the operators $a_1(z,t)$, $a_2(z,t)$, and $b(z,t)$ are the envelope operators of the pump, anti-Stokes, and acoustic field at their respective carrier frequencies ω_1, ω_2, and Ω. Here v_1, v_2, and v_b are the group velocities of the fields. It is important to note that with the definition of the field operators here, the expectation value of the form $\langle a^\dagger(z,t)a(z,t)\rangle$ should be understood as photon (phonon) linear density (occupation number per unit length) [179]. The average power is therefore $P_1 = \hbar\omega_1 v_1 \langle a_1^\dagger a_1\rangle$, $P_2 = \hbar\omega_2 v_2 \langle a_2^\dagger a_2\rangle$, and $P_b = \hbar\Omega v_b \langle b^\dagger b\rangle$ for the pump, anti-Stokes, and acoustic field respectively. We have also introduced the temporal loss rates κ_1, κ_2, and Γ of the fields and the Langevin noise [181, 48, 179] operator ξ into the coupled wave equations. Let us first discuss the behavior of the acoustic field with noise source when no coupling to the optical fields exists.

7.2.3 Result: solution of three-coupled equations for achieving cooling

Low group velocity acoustic modes at thermal equilibrium

The properties of the acoustic noise source $\xi(z,t)$ in a waveguide have been derived previously in [181, 179] for low group velocity phonons. Here we briefly reproduce the derivation of [179] as it will be important in our later discussion. To obtain the correlation relation of the noise operator, we first turn off the coupling term in the acoustic field equation. For a low group velocity phonon, the spatial variation of the acoustic field is negligible as it is small compared with the temporal variation term. We now divide the waveguide into small segments labeled by index i, each with length Δz and uncorrelated noise source ξ_i. The equation satisfied by each $b_i(t)$ is

$$\frac{\partial b_i}{\partial t} = -\Gamma b_i + \xi_i. \tag{7.2}$$

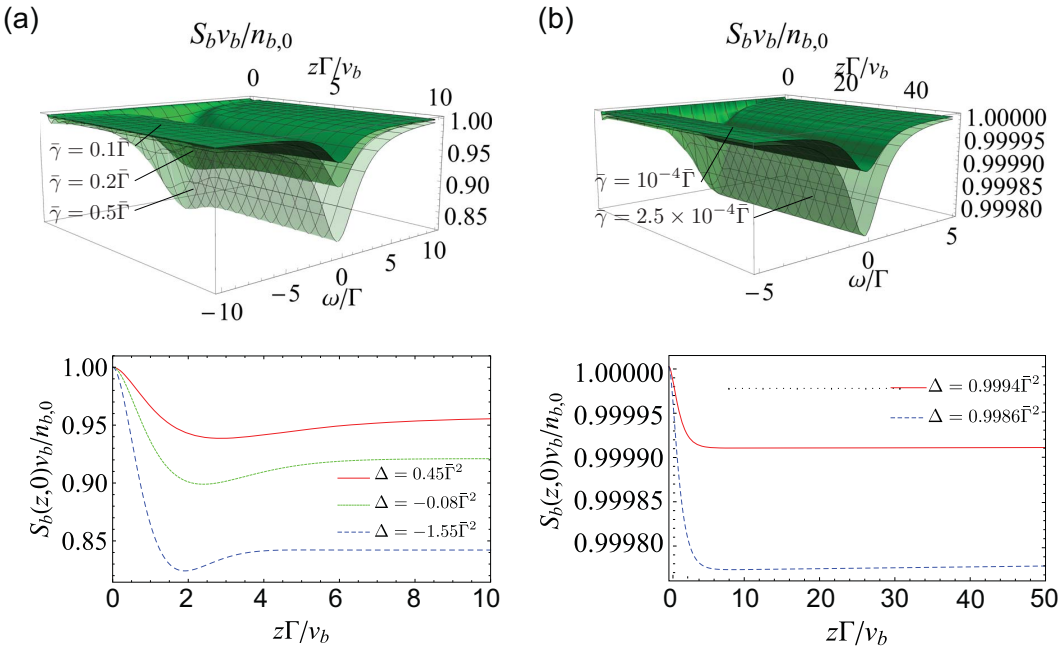

Figure 7.2: Spectra of (a) phonon density and (b) anti-Stokes photon density as functions of z and ω for cooling of high group velocity phonons. We set $\gamma = 1000\Gamma$ and $g = 30\Gamma$. The group velocity of the acoustic mode is set to $v_b = 10^{-4}v$, $v_b = 2 \times 10^{-4}v$, and $v_b = 5 \times 10^{-4}v$ corresponding to spatial loss rates of $\bar{\gamma} = 0.1\bar{\Gamma}$, $\bar{\gamma} = 0.2\bar{\Gamma}$, and $\bar{\gamma} = 0.5\bar{\Gamma}$. The corresponding discriminants are $\Delta = 0.45\bar{\Gamma}^2$, $\Delta = -0.08\bar{\Gamma}^2$, and $\Delta = -1.55\bar{\Gamma}^2$, respectively. The bottom panel of the figure shows the evolution of the spectrum at center frequency $\omega = 0$. With larger group velocity v_b, the acoustic spectrum exhibits oscillatory behavior near the beginning of the waveguide corresponding to a negative value of Δ.

Here we note that these properties of the noise source lead to a divergent solution of the phonon density at a particular point in the waveguide $\langle b^\dagger(z,t)b(z,t)\rangle = \lim_{dz\to 0} \frac{n_{b,0}}{dz}$, which results from taking continuous limit of the discrete waveguide model. However, we can formally rewrite the phonon density as

$$\langle b^\dagger(z,t)b(z,t)\rangle = \lim_{z\to 0} n_{b,0}\delta(z) = \lim_{z\to 0} \frac{1}{2\pi}\int_{-\infty}^{\infty} n_{b,0}e^{ikz}dk = \frac{1}{2\pi}\int_{-\infty}^{\infty} n_{b,0}dk. \quad (7.3)$$

The spectrum of the phonon density in the k-space is therefore flat and has a constant value $n_{b,0}$ for this model of the noise source. In fact, as we will see later, important information about the phonon mode can be extracted from a narrow range in the k-space centered around $k = 0$.

High group velocity acoustic modes at thermal equilibrium

We can now examine the behavior of high group velocity acoustic modes. The equation of motion for the acoustic field without coupling to the optical fields is given by

$$\frac{\partial b}{\partial t} + v_b \frac{\partial b}{\partial z} = -\Gamma b + \xi. \tag{7.4}$$

To avoid the divergent problem we try to look at the power spectral density of $S_b(z,\omega)$ of $b(z,t)$[2] . It is reasonable to assume that the correlations $\langle \tilde{b}^\dagger(0,\omega)\tilde{\xi}(z',\omega')\rangle$ and $\langle \tilde{\xi}^\dagger(0,\omega)\tilde{b}(z',\omega')\rangle$ vanish, i.e. the acoustic field is uncorrelated to the noise at different spatial point. We can then invoke the properties of the noise to find

$$\begin{aligned} S_b(z,\omega) &= S_b(0,\omega)e^{-2\Gamma z/v_b} + \frac{2\Gamma n_{b,0}}{v_b^2}\int_0^z dz' e^{-2\Gamma(z-z')/v_b} \\ &= S_b(0,\omega)e^{-2\Gamma z/v_b} + \frac{n_{b,0}}{v_b}(1-e^{-2\Gamma z/v_b}), \end{aligned} \tag{7.5}$$

where $S_b(0,\omega)$ is the spectral density of b at $z = 0$ under the initial condition $\tilde{b}(0,\omega)$. For $z \to \infty$ the spectral density is independent of its initial form $S_b(0,\omega)$ as anticipated.

$$S_b(\infty,\omega) = \frac{n_{b,0}}{v_b}. \tag{7.6}$$

From Eq. (7.5) we see that regardless of the detail of initial acoustic spectrum, the effect of the noise always bring the acoustic spectrum back to the value $n_{b,0}/v_b$. In fact, if we substitute Eq. (7.6) into Eq. (7.5) as the initial spectral density $S_b(0,\omega)$, we immediately find that the spectral density $S_b(z,\omega)$ is independent of position z in the waveguide, as it should be in the case without coupling.

We successfully linearize Eqs. (7.1) through the non-deplete approximation, as the pump field is in general dominant over the other modes. With help of the Laplace transform in the z-direction for the Fourier transformed variables, one obtains solutions for the acoustic spectral density over the spatial and frequency domains.

[2]Here we use the Fourier transform as defined by

$$\tilde{b}(z,\omega) = \int_{-\infty}^{\infty} b(z,t)e^{i\omega t}dt, \quad \text{and} \quad b(z,t) = \frac{1}{2\pi}\int_{-\infty}^{\infty} \tilde{b}(z,\omega)e^{-i\omega t}d\omega,$$

Figure 7.2(a) and (b) illustrate the spectra of phonon density and as functions of z and ω for cooling of high group velocity and low group velocity phonons, respectively. We conclude this section with a comparison between our solution and that of a recent study on noise in Brillouin systems [179], which only solves for low group velocity phonons and in which cooling is not discussed. The optical loss was set to zero in the calculation of [179] which also means that no phonon cooling can occur. For finite coupling g, we can integrate the anti-Stokes spectrum to obtain the anti-Stokes photon number per unit length $\langle a_2^\dagger(z,t)a_2(z,t)\rangle$ (See the further explanation in our paper [26]).

7.2.4 Practical considerations for observing Brillouin cooling in linear waveguides

We can now use known experimental results to evaluate how much cooling could potentially be achieved in a waveguide. In the following discussion we fix the pump wavelength at 1550 nm and focus only on silicon photonic waveguides [182, 183, 184]. The group velocity of the optical field in these waveguides is approximately $v \approx c/n \approx 8.62 \times 10^7$ m/s for low dispersion modes, but is certainly dependent on the specific optical mode. Since the optical decay length in photonic waveguides is typically of the order of cm, we fix the optical loss at $\bar{\gamma}$ at 3.456 m^{-1} corresponding to a good value of 0.3 dB/cm reported in [185].

The acoustic loss can be obtained from the Q-factor of the acoustic modes using the expression $\bar{\Gamma} = \Omega/2v_bQ$. The theoretical limits on the acoustic Q-factor in silicon have been suggested previously in [186]. Using these data, for a 500 MHz phonon the Q-factor for silicon can theoretically approach 50000, giving an acoustic loss of 3.7 m^{-1} for phonons traveling at the speed of sound $v_b = 8500$ m/s. However, the Q-factors of the phonon modes in recent experiments are not so high, and are typically of the order of a few hundreds [182, 183, 184]. Since these prior studies are for low group velocity phonons ~ 1 m/s, it will lead to acoustic loss of the order $\sim 10^6$ m^{-1} for phonons in the 500 MHz range. As we show above, higher group velocity phonon modes are more practical for cooling. For the sake of calculation we fix the velocity at $v_b \approx 8500$ m/s [186] corresponding to traveling acoustic phonons in silicon but assume a low Q-factor ($Q \sim 100$), giving us an acoustic loss of 1848 m^{-1}. Recently reported SBS gain in silicon waveguides ranges from 1000 $\mathrm{W}^{-1}\mathrm{m}^{-1}$ [182, 183] to 10^4 $\mathrm{W}^{-1}\mathrm{m}^{-1}$ [184]. Gain as high as 4×10^6 $\mathrm{W}^{-1}\mathrm{m}^{-1}$ was also reported for acousto-optic

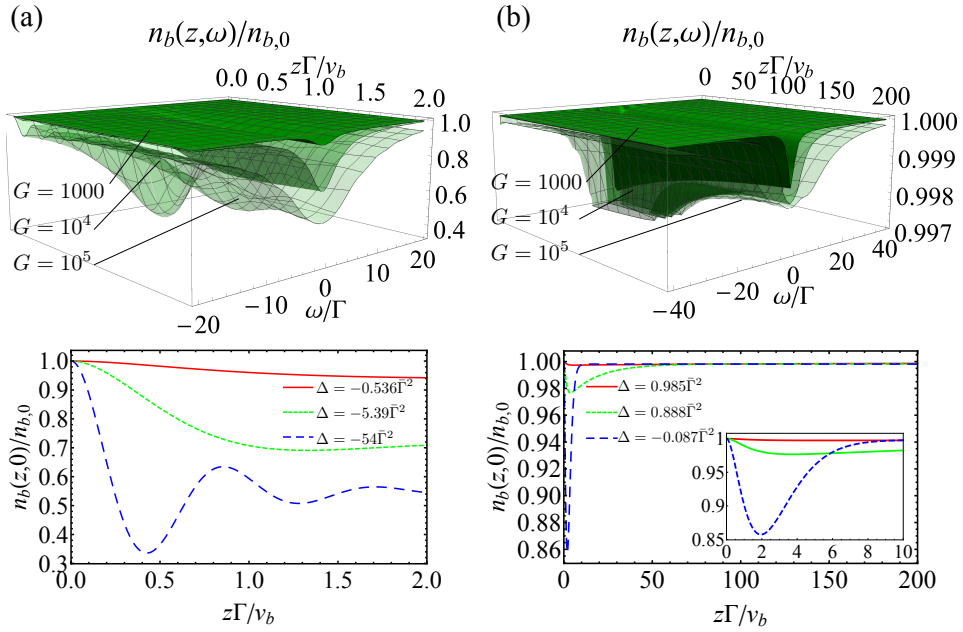

Figure 7.3: Spectral cooling ratio of 500 MHz phonons for (a) a high-Q acoustic mode $Q = 50000$ ($\bar{\Gamma} = 3.7$ m^{-1}), with 1 mW pump power, and (b) a low-Q acoustic mode $Q = 100$ ($\bar{\Gamma} = 1848$ m^{-1}), with 10 mW pump power. In both cases optical parameters are $\bar{\gamma} = 3.456$ m^{-1} and $v = 8.62 \times 10^7$ m/s, while phonon group velocity is set to a high number $v_b = 8500$ m/s. The bottom panel of the figure shows the evolution of the spectrum at center frequency $\omega = 0$. The inset in (b) shows that the cooling ratio for high SBS gain $G = 10^5$ W^{-1}m^{-1} can reach far below the long range limit in the beginning portion of the waveguide.

scattering from a 6 MHz phonon mode in a specialized optical fiber [187].[3] Using the parameters described above, we can now plot (in Fig. 7.3) the spectral cooling ratio for acoustic modes for both $Q = 50000$ and $Q = 100$ at 500 MHz with various SBS gain G and pump power P_1. For the high-Q mode (Fig. 7.3a) with large gain, cooling at the central frequency can reach the saturation limit of 0.517 within a few decay lengths with just 1 mW pump. The spectrum in this strong coupling regime also exhibits oscillatory behavior as discussed previously. For the low Q mode (Fig.

[3]The above parameters now allow evaluation of g through

$$g = \sqrt{\frac{GP_2v\Gamma}{2}}.$$

7.3b), the cooling limit 0.9981 is reached after a few hundred decay lengths with a larger 10 mW pump. Note that at the entrance region of the waveguide the cooling ratio can momentarily dip far below the limit, but it will return to this limit at larger z. These results show that to observe appreciable cooling in an experiment, a high-Q phonon with large group velocity is required. Similar calculation can be carried out for low group velocity phonons (v_b ~1 m/s), however, no appreciable cooling can be achieved even with modes with Q as high as 50000.

7.2.5 Proposal: How can we break TRS in linear waveguides via Brillouin scattering and suppress disorder-induced scattering

So far, we have investigated how Brillouin cooling can occur in linear waveguides under different situations. Here, I would like to introduce the brief proposal that is able to expand our previous idea to waveguide systems. In general, the whole equations for photonic systems are presented in Eqs. (7.1). Particularly, the time derivatives are considered in the case of resonators as previously discussed (See Eqs. (2.19)). In the meantime, the spatial derivatives can be considered in waveguides so that they become under the non-depleted approximation in the classical limit:

$$\frac{\partial a_-}{\partial z} = -\frac{\kappa_l}{2}a_- - i\frac{G}{v_a}b - iV_l a_+, \tag{7.7a}$$

$$\frac{\partial a_+}{\partial z} = -\frac{\kappa_l}{2}a_+ - iV_l a_-, \tag{7.7b}$$

$$\frac{\partial b_-}{\partial z} = -\frac{\Gamma_l}{2}b_- - i\frac{G^*}{v_b}a_-. \tag{7.7c}$$

where the loss rates are $\kappa_l = \kappa_2/v_2$ and $\Gamma_l = \Gamma/v_b$, and the optomechanical coupling rate in waveguides is G_l. Here V_l is the backscattering between these two modes $a_\pm$ where these two modes are propagating in the forward (+) and backward (-) directions, due to disorder-induced scattering. Specifically, the optomechanical coupling is engaged in the backward direction (-) only.

Now, the disorder-induced "back"scattering should be examined in the waveguide. Suppose the backscattering is caused by inhomogeneity within host materials and/or surface roughness, so we have to calculate the backscattering rate compared to the entire disorder-induced scattering. This conversion entirely relies on the numerical aperture of the waveguide such that we consider high-index contrast

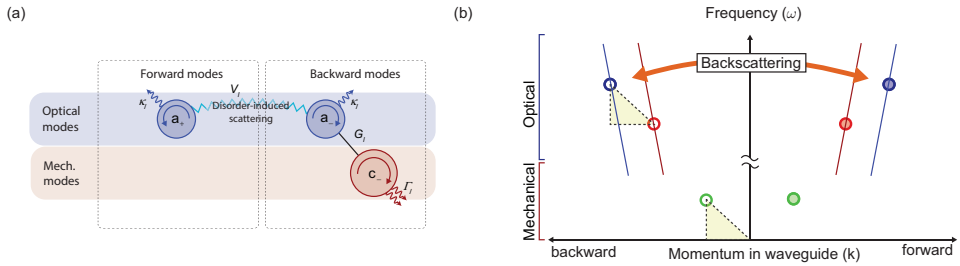

Figure 7.4: (a) Toy model for the suppression of disorder-induced backscattering in waveguides. a_+ (or a_-) mode represents the forward (or backward) propagating mode in the system, and b_- is the mechanical mode in the backward direction. These two optical modes are coupled by the backscattering V_l. (b) $\omega - k$ diagram for the system. The optomechanical coupling is engaged in the backward direction only.

waveguides (See in [188]). For a silicon waveguide, the efficiency is around 20% which is reasonable.

We can also evaluate the effective loss rates for these two optical modes as follows:

$$\kappa_{\text{eff}}^{+} = \kappa(1 + C_l) + \frac{4V^2}{\kappa} \tag{7.8a}$$

$$\kappa_{\text{eff}}^{-} = \kappa + \frac{4V^2}{\kappa(1 + C_l)} \tag{7.8b}$$

where the optomechanical cooperativity in waveguides is $C_l = \frac{4G^2}{v_a v_b \Gamma}$. Similar to what we have discuss in the previous chapters, the loss rates for their modes become asymmetric under the unidirectional pumping. As a result, the backward optical mode can become fully coherent in the limit of infinite optomechanical coupling rate.

7.2.6 Conclusions

We have investigated the anti-Stokes Brillouin scattering process in linear waveguides for the possibility of achieving phonon annihilation and cooling. We show that the degree of cooling depends strongly on the acoustic and optical spatial loss rates. The results can be categorized into two regimes that depend on the strength of the acousto-optical interaction: strong coupling ($\Delta > 0$) and low coupling ($\Delta < 0$). In the first case the spectrum of the fields shows oscillatory behavior before reaching

steady-state. In the second case, the spectrum exhibits no oscillatory behavior and only reaches its steady-state after longer propagation distances. The limit on the cooling ratio in waveguides takes the same form as in optomechanical cooling in resonators, as expected, with the temporal variables replaced by corresponding spatial loss variables. The effect of higher phonon group velocity is to not only increase the spatial coupling strength but also give an improved cooling ratio limit.

Our analysis indicates that for potential cooling experiments, traveling phonons with high group velocity are more favorable, and the design of waveguides should be focused on improving the quality factor of such high group velocity phonon modes. Additionally, enhancement of SBS gain is also highly desirable for cooling [83, 79]. With a combination of high-Q, high group velocity phonons, and gain of the order of 10^5 $\mathrm{W}^{-1}\mathrm{m}^{-1}$, appreciable cooling may be observed with a pump power of a few mW. A key difference between cavity optomechanical cooling and Brillouin cooling is that the latter annihilates traveling phonons, whose higher frequency cousins are also responsible for heat transport in micro- and nano-scale devices. The possibility of accessing Brillouin cooling in linear systems thus opens up a new approach to laser cooling, and may in the future impact phonon management in photonic circuits and quantum information transport via phonons.

More importantly, this Brillouin cooling process can be also utilized to suppress the disorder-induced backscattering in linear waveguides. This Rayleigh scattering, which is caused by defects introduced during the fabrication process, can limit the performance of linear waveguides and lead to serious issues in photonic systems. Here, our proposal to mitigate the backscattering in linear waveguide can enhance the efficiency of the integrated photonic circuits.

7.3 Breaking time-reversal symmetry by acousto-optic scattering in nanophotonic devices

7.3.1 Motivation

[4] We experimentally demonstrate an alternative method to break time-reversal symmetry in an on-chip aluminum nitride resonator via acousto-optic scattering. In

[4]Portions of this chapter are reprinted with permission from Sohn, D.B., Kim, S et al., (2018), "Time-reversal symmetry breaking with acoustic pumping of nanophotonic circuits," Nature Photonics, 12, pp. 91-97.

principle, piezoelectrically driven acoustic waves can effectively generate grating within aluminum nitride, thereby leading to optical scattering. Here, we use aluminum nitride since it is one of the most prominent materials for acousto-optics at microwave frequencies. Similar to the previous works, momentum-selective interaction within aluminum nitride based resonators among two orthogonal optical modes mediated through the piezoelectrically driven acoustic wave. Specifically, this approach also utilizes interband transitions to achieve nonreciprocity as shown in Fig. 7.5c, as inspired by the coupled-mode theory [49].

This method represents some advantages over other methods for TRS breaking through optomechanics or electro-optics; Our method gives broader nonreciprocal bandwidth compared to the optomechanical approaches [20, 18, 189]. Similarly, electro-optic implementations provide very large bandwidth but require a sophisticated electric network to slow down the phase velocity of the microwave which leads to very poor insertion loss [106].

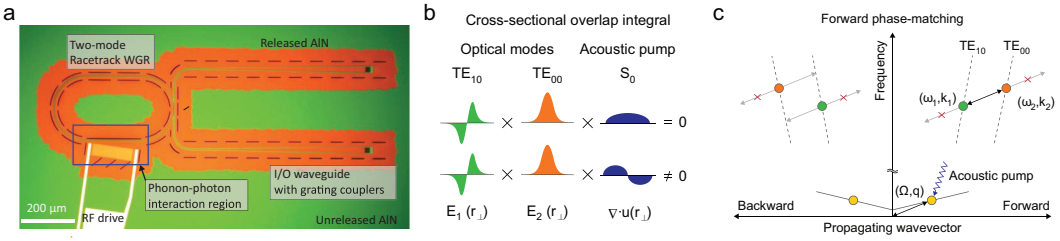

Figure 7.5: Conceptual schematic of acoustically pumped non-reciprocal nanophotonic modulator. (a) The device is composed of a racetrack resonator supporting two optical modes (TE_{10} and TE_{00}). An electrically driven 2-dimensional acoustic wave (pump) simultaneously breaks orthogonality between the optical modes while also satisfying the phase matching condition. s_{in} and s_{out} represent input and output signals from the waveguide. (b) Illustration of the transverse mode profiles ($E_1(\mathbf{r}_\perp)$, $E_2(\mathbf{r}_\perp)$ are electric fields, $u(\mathbf{r}_\perp)$ is material displacement) shows the odd acoustic pump profile needed to obtain non-zero overlap integral. (c) The required phase matching condition illustrated in frequency-momentum space. The acoustic pump is launched in the forward direction with frequency and momentum (Ω, q). When the resonance frequency of the TE_{00} mode (ω_2, k_2) is higher than of the TE_{10} mode (ω_1, k_1), the phase matching condition can be satisfied in the forward direction.

As shown in Fig. 7.5b, the electric fields of TE_{10} and TE_{00} modes within an appropriately designed waveguide have odd and even shapes in the transverse direction, respectively. Therefore, the density variation associated with the acoustic wave must be asymmetric with respect to the center of the waveguide to ensure non-zero acousto-optic coupling β. In the case where the node is located exactly at

the center of the waveguide, we can maximize the intermodal coupling and simultaneously suppress intramodal scattering by balancing out compressive and tensile strain in the waveguide.

The acousto-optic interaction in the forward phase matched case (Fig. 7.5c) can now be described using the coupled equations of motion for the optical fields:

$$\frac{\partial}{\partial t}\begin{pmatrix} a_1 \\ a_2 \end{pmatrix} = -i\begin{pmatrix} \omega_1 - i\kappa_1/2 & G_{ph}^{*}e^{i\Omega t} \\ G_{ph}e^{-i\Omega t} & \omega_2 - i\kappa_2/2 \end{pmatrix}\begin{pmatrix} a_1 \\ a_2 \end{pmatrix} + \begin{pmatrix} \sqrt{\kappa_{ex1}} \\ \sqrt{\kappa_{ex2}} \end{pmatrix} s_{in}e^{-i\omega_l t} \tag{7.9}$$

where a_1 (a_2) is the intracavity field, κ_1 (κ_2) is the loaded decay rate of the TE_{10} (TE_{00}) mode, $G_{ph} = \beta u$ is the phonon-enhanced optomechanical coupling rate, and u is displacement associated with the acoustic pump. We assume that an input field s_{in} at carrier frequency ω_l is provided to the resonator via an evanescently coupled waveguide (Fig. 7.5a) with coupling rates κ_{ex1} and κ_{ex2} to the TE_{10} and TE_{00} optical racetrack modes respectively. In the case where we probe the a_2 mode, we can express the optical susceptibility as $\chi_{om}(\omega) = [\kappa_2/2 + i(\omega_2 - \omega) + \alpha(\omega)]^{-1}$ where ω is Fourier frequency and $\alpha(\omega) = |G_{ph}|^2 / [\kappa_1/2 + i(\omega_1 + \Omega - \omega)]$ is an additional optical loss rate induced by the acousto-optic interaction. In contrast, optically pumped optomechanical systems [22, 101, 114, 190, 191, 19, 20, 18] have an interaction term of the form $\alpha(\omega) = |G|^2 / [\Gamma/2 + i(\Omega_m + \omega_p - \omega)]$ where $G = \beta a_1$ is the photon-enhanced optomechanical coupling rate, Γ is decay rate of the mechanical mode, Ω_m is the mechanical resonant frequency, and ω_p is the pump laser frequency [20]. We can immediately see that the interaction bandwidth in the acoustically pumped case is no longer defined by the linewidth Γ of the mechanical mode, but instead by the linewidth κ_1 of the a_1 optical mode. This feature enables an orders-of-magnitude higher bandwidth non-reciprocal interaction.

7.3.2 Demonstration of breaking time-reversal symmetry

We experimentally demonstrated non-reciprocal modulation within the system by measuring the optical sidebands for forward and backward probe signals. The measured reflection coefficient (s_{11} parameter) shows a resonant dip corresponding to conversion efficiency of the input electronic stimulus into the acoustic wave. We can directly measure this characteristic acoustic resonance at 4.82 GHz, corresponding to the S_0 Lamb surface acoustic wave on the AlN substrate. We measure the optical transmission spectrum from the perspective of the coupling waveguide, where the

transmission dips corresponding to the modes of the racetrack resonator are clearly visible. The TE_{00} mode is seen to have higher Q factor ($Q_{TE_{00},loaded} \approx 171{,}000$) than the TE_{10} mode ($Q_{TE_{10},loaded} \approx 95{,}000$). The measured free spectral ranges (FSR) of TE_{00} and TE_{10} resonances are respectively 140.5 GHz and 136 GHz near 194.7 THz optical frequency. Therefore, the intermodal frequency difference changes by approximately 4.5 GHz for each consecutive mode pair. On the other hand, the momentum difference of each mode pair is the same since the azimuthal mode order of the pairs is the same.

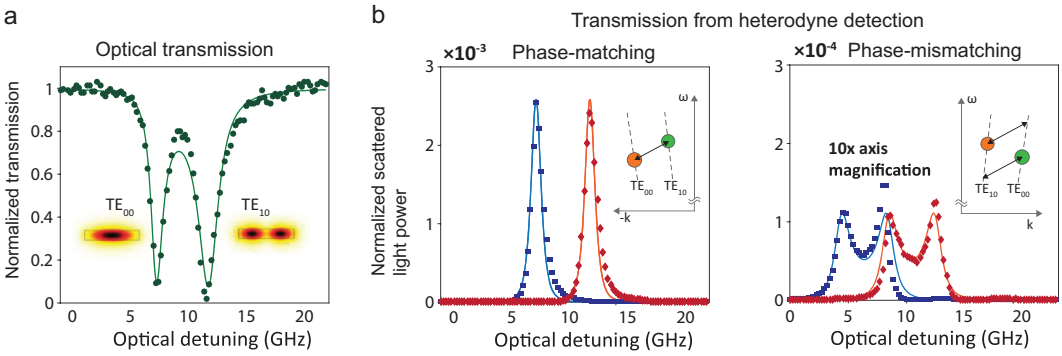

Figure 7.6: Experimental demonstration of non-reciprocal optomechanical modulation. Mode pair corresponds to a near-perfect backward phase-matching condition. Here the optical modes are separated by $\omega_1 - \omega_2 = 4.55$ GHz (TE_{00} mode is located at lower frequency) such that a 4.82 GHz acoustic mode has the correct momentum to enable phase matching. (a) It presents the backward transmitted signal at the optical carrier frequency component (Green). Carrier transmission measurements in the forward direction are nearly identical. (b) Measurements of Stokes (Red) and anti-Stokes (Blue) sidebands when the system probed in the backward direction and the third row. (c) Sideband measurements for forward probing.

In this experiment, the RF frequency is fixed to 4.82 GHz where the IDT can most efficiently actuate the acoustic wave. We sweep the optical probe across each pair of modes while measuring the power of forward and backward transmitted carrier frequency component ($s_{out,0}$), down-converted Stokes sideband ($s_{out,-1}$), and up-converted anti-Stokes sideband ($s_{out,+1}$) (Fig. 7.6b) simultaneously. All measured optical outputs are normalized against the input field within the waveguide (s_{in}). In these measurements, we present only the on-chip (i.e. waveguide input to waveguide output) power transmission coefficients while calibrating out the grating coupler efficiencies. The RF drive power is set to 0 dBm so that the optical sidebands are small compared to the input light. The carrier frequency transmission coefficients in both directions effectively remain identical for such small RF drive. Even so, the

nonreciprocal inter-modal scattering implies that the optical modes in the phase-matched direction will experience a small increase in their intrinsic loss rate.

We examine sideband generation and reciprocity in the case where both phase matching and the frequency matching are well satisfied (Fig. 7.5c and Fig. 7.6). Here, the optical resonance frequency of the TE_{00} mode is lower than the resonance frequency of the TE_{10} optical mode by 4.55 GHz, implying that the phase matching condition is satisfied in the backward direction for a forward directed phonon pump (as illustrated in Fig. 7.5c). Measurements show (Fig. 7.6b) that when each optical mode is probed in the backward direction, resonant sideband generation occurs with the assistance of the second optical mode. For laser detuning between 5-10 GHz (arbitrary reference) light from the waveguide primarily enters TE_{00} mode resulting in a strong anti-Stokes sideband. Scattering to Stokes is strongly suppressed (45 dB smaller than the anti-Stokes) since there is no optical mode available in the resonator. Similarly, for laser detuning between 10-15 GHz, light from the waveguide primarily enters the TE_{10} mode, and only the Stokes sideband is generated through resonant enhancement from the TE_{00} optical mode. The transmission, Stokes, and anti-Stokes spectra that share parameters are simultaneously fitted using our model discussed in Appendix B.1. Based on the fitting of the experimental data, we obtained a -3 dB bandwidth (full width half maximum) of $\sim$1.14 GHz for this modulation effect, which is determined by the optical resonance linewidths. We can also quantify the intermodal optomechanical coupling coefficient as $\beta = 1.64$ GHz/nm.

On the other hand, when light enters the system in the forward direction where the momentum matching condition is not satisfied, very small light scattering is observed (Fig. 7.6b). At the laser detuning where the maximum sideband amplitude is obtained in the backward direction, the sideband generated for forward probing is $\sim$15 dB smaller than that obtained for a backward laser probe. The measurement presented in Fig. 7.6b needs to be magnified by 10x (see inset) in order for the data trends to be observable. The residual scattering that is observed has the characteristic functional shape of conventional intramodal modulation occurring from optical path length change4. While this effect should nominally be zero, there are practical constraints associated with non-zero overlap integral due to acoustic-optical misalignment and the curvature of the racetrack. We account for this with empirical intramodal scattering parameters in our model.

7.3.3 Conclusions

We have experimentally demonstrated time-reversal symmetry breaking through acousto-optic on an AlN device achieved by piezoelectrically pumping. The data acquired from the heterodyne detection shows clear nonreciprocal behavior of the transmissions in the cases of phase-matched condition and phase-mismatched condition. The nanophotonic system that we have presented operates as a frequency shifting isolator in which light propagating in one direction experiences a fixed frequency offset, while in the opposite direction light is simply absorbed. The operational optical wavelength and pumping strategy of this system are entirely lithographically defined, which ensures rapid adaptability to other wavelength regimes. More broadly, this acoustic pumping technique and the level of performance achieved indicates a clear path towards foundry-compatible integration of linear isolators, circulators, and non-reciprocal phase shifters, that overcome the fundamental challenges currently plaguing state of the art non-magnetic non-reciprocal devices. This approach can also potentially introduce new non-reciprocal functionality to chip-scale photonics including frequency shifters [192] and dynamic converters for mode division multiplexing [193]. Most importantly, such nonreciprocity can pave a novel way to suppress disorder-induced scattering in on-chip waveguides and resonators which is not avoidable during the fabrication process.

Appendix A

Analytic analysis of optical WGMs

Optical WGMs are governed by the Helmholtz equations in Eq. (2.1) with boundary conditions determined by geometries in Eq. (2.2). Equation (2.1) rewritten in spherical coordinate is given by:

$$\frac{1}{r}\frac{\partial^2}{\partial r^2}(rE) + \frac{1}{r^2\sin\theta}\frac{\partial}{\partial\theta}\left(\sin\theta\frac{\partial E}{\partial\theta}\right) + \frac{1}{r^2\sin^2\theta}\frac{\partial^2 E}{\partial\phi^2} = 0. \tag{A.1}$$

Suppose that the vectorial E-field becomes $E(r,\theta,\phi) = R(r)P(\theta)Q(\phi)$ in spherical coordinates, so the azimuthal component $Q(\phi)$ is readily given by

$$Q = e^{\pm m\phi}, \tag{A.2}$$

where m is the eigenvalue of the azimuthal component, i.e. the azimuthal mode order. Consequently, the radial and polar components become

$$\frac{1}{\sin\theta}\frac{\partial}{\partial\theta}\left(\sin\theta\frac{\partial P}{\partial\theta}\right) + \left[l(l+1) - \frac{m^2}{\sin^2\theta}\right]P = 0 \tag{A.3a}$$

$$r^2\frac{\partial^2 R}{\partial r^2} + 2r\frac{\partial R}{\partial r} + \left[n(r)^2k^2r^2 - l(l+1)\right]R = 0 \tag{A.3b}$$

The solution of Eq. (A.3a) is the associated Legendre polynomial $P_l^m(\cos\theta)$, where l is a positive integer and m runs over integer values from $[-l, l]$. Combined with the azimuthal solution in Eq. (A.2), $P_l^m(\cos\theta)$ becomes the vectorial spherical harmonics $\boldsymbol{Y}_{lm}$. Meanwhile, the solution of Eq. (A.3b) of our interest is the spherical Bessel functions j_l and y_l. By the change of variable $R(r) = \frac{Z(r)}{\sqrt{knr}}$, equation A.3(b) becomes

$$r^2\frac{\partial^2 Z}{\partial r^2} + r\frac{\partial Z}{\partial r} + \left[n(r)^2k^2r^2 - (l+\frac{1}{2})^2\right]Z = 0 \tag{A.4}$$

whose solution is the Bessel function of $(l+1/2)$ order. The solution of Eq. (A.3b) thus should be the spherical Bessel functions $j_l(nkr) = \sqrt{\pi/2nkr}J_{l+1/2}(nkr)$ and $y_l(nkr) = \sqrt{\pi/2nkr}Y_{l+1/2}(nkr)$. The silica sphere with its radius a having the refractive index n has the solution.

$$\begin{aligned} R(r) &= j_l(nkr) && \text{for} \quad r < a \\ &= Aj_l(kr) + By_l(kr) && \text{for} \quad r > a \end{aligned} \tag{A.5}$$

Owing to the origin inside the sphere, the solution $R(r)$ for $r < a$ must have only the first kind function $j_l(r)$, while the solution has $j_l(r)$ and $y_l(r)$ outside the sphere. As the E field is continuous across the boundary at $r = a$, one can obtain these following relations.

$$\begin{aligned} j_l(nka) &= Aj_l(ka) + By_l(ka) \\ nj_l'(nka) &= Aj_l'(ka) + By_l'(ka) \end{aligned}$$

The following equations represent the exact solutions for the radial component of E field[1], however they cannot be solvable in a typical way. As the field outside of the sphere is a leaky wave, such radiative part would be negligible, i.e. $A \to 0$. As a result, the continuous conditions described in Eq. (2.2) can be obtained. Unfortunately, equation (2.2 is not solved analytically, as it has multiple Bessel functions. Such Bessel functions give the multiple roots at each point which is related to the radial order s. Therefore equation (2.2 is only dependent on (l, s) so that mode shapes are degenerate under different the azimuthal orders m. Lam et al., have asymptotically analyzed Eq.(2.2) by expanding each Bessel function to find these roots that are positions of resonances [44].

$$\begin{aligned} nx_{l,s} = \nu + 2^{-1/3}\alpha_s\nu^{1/3} - \frac{n}{(n^2-1)^(1/2)} + \frac{3}{10}2^{-2/3}\alpha_s^2\nu^{-1/3} \\ - \frac{2^{-1/3}n(n^2-2n^2/3)}{(n^2-1)^{3/2}}\alpha_s\nu^{-2/3} + O(\nu^{-1}), \end{aligned}$$

where α_s are the s-th roots of $\mathrm{Ai}(-z)$.

[1] In the introduction chapter, the radial component is written in $U(r) = R(r)/r$ for TE modes.

Appendix B

Numerical analysis of WGMs

COMSOL is one of the best multiphysics tools for numerical analysis through the finite element method (FEM) simulation. All simulation performed in this thesis has done by COMSOL, therefore this section goes over how to simulate mechanical and optical WGMs through the COMSOL program.

B.1 Mechanical WGMs

An understanding of the acoustic wave equation is a key for analyzing Brillouin optomechanical interaction accurately. The acoustic wave equation is given by:

$$\frac{\partial^2 u_i}{\partial t^2} = v^2 \nabla^2 u_i + \Gamma' \nabla^2 \frac{\partial u_i}{\partial t} + \frac{F_i}{\rho}, \tag{B.1}$$

where u_i is the vectorial expression for the acoustic amplitude, Γ' is the damping rate, and ρ is the density of the medium in which the acoustic wave propagates. Suppose that the acoustic wave satisfies the phase matching condition, and F_i is the external force, i.e. electrostriction force, for driving the wave. Under the slowly varying amplitude approximation in steady state, the solution of Eq.(B.1) becomes when the acoustic wave travels with its frequency Ω and wavenumber k

$$u_i = \frac{F_i/\rho}{\Omega_B^2 - \Omega^2 - i\Omega\Gamma_B},$$

where $\Omega_B = vk$ is the acoustic resonant frequency of the medium and $\Gamma_B = \Gamma' k^2$ is the Brillouin linewidth. However, one cannot obtain the dynamic behavior of the acoustic wave from the above expression due to the approximations applied. As a result, the numerical analysis through the FEM simulation is needed to investigate the acoustic wave in WGMs due to Brillouin scattering.

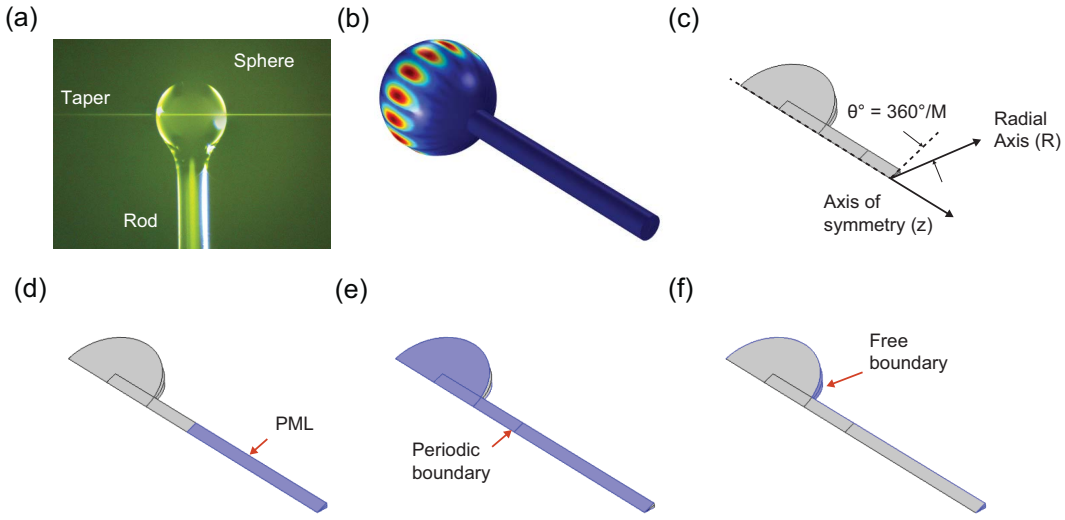

Figure B.1: Geometry and boundary conditions for simulating an acoustic WGM with a rod.

The Structural Mechanics Analysis package is employed to simulate the acoustic WGMs in resonators as shown in Fig. B.1. For the sake of reducing computational cost, 2D asymmetric dimension is chose in Model Wizard so that the the azimuthal mode order, m-number, restores a whole structure as shown in Fig. B.1(c). Note that as clamping loss induced by the rod in Fig. B.1(a) definitely affects the acoustic WGMs, a perfectly matched layer (PML) condition [1] must be set in the major part of the rod. The periodic boundary condition is also applied to the facets which are supposed to be next to periodic structures (See Fig. B.1(e)). Meanwhile the free boundary condition is set on the rest of facets as expected.

[1] A good intuitive explanation of PML has been given in reference [194]. In computational region, waves should be reflected by adjacent numerical boundaries which is similar to how a typical wave equation is reflected in analytic region. These boundaries called PMLs keep waves from reflecting at boundaries which can absorb the waves. The concept of PML is mathematically achievable through the transform $\frac{\partial}{\partial x} \rightarrow \frac{1}{1+i\frac{\sigma_x(x)}{\omega}}\frac{\partial}{\partial x}$ so that the exponential term becomes $e^{ikx-\frac{k}{\omega}\int^x dx'\sigma_x(x')}$. This expression naturally indicates attenuation of waves relying on the sign of $\sigma_x(x)$. Therefore the propagating waves through the PML can decay exponentially after a few round trips bounced at boundaries.

B.2 Optical WGMs

Optical WGMs in resonators can also be simulated by the COMSOL Multiphysics package. However, the m-numbers of optical WGMs are in general larger than the number of acoustic WGMs[2]. Specifically, the optical m-number is around hundreds[3] so that the finite element mess could be larger than a scale of outward facets.

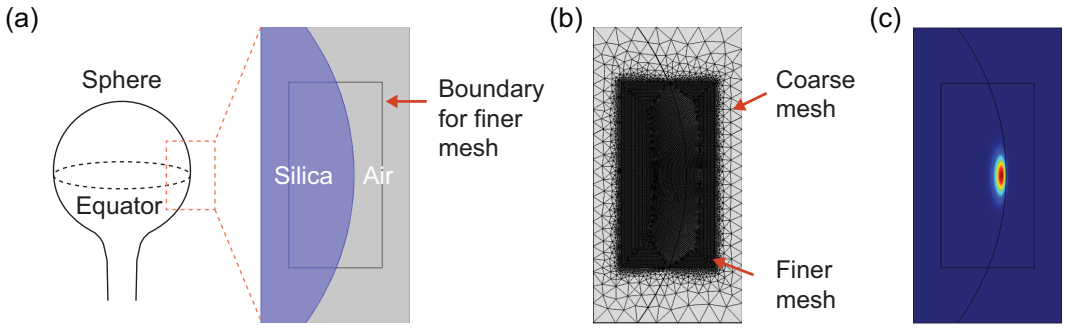

Figure B.2: (a) Simplified domain for the FEM simulation. As an optical modal volume is small enough, we take a part of 2d projected domain. Here, we set the specific boundary for finer mesh. (b) Construction of mesh. Finer mesh is utilized for analyzing optical modes accurately. (c) Example of the result from the FEM. For this optical mode, it is well confined within the boundary for finer mesh.

Figure B.2(a) illustrates that the sphere resonator projected on the side view is constructed with the boundary for building finer mesh. The boundary is adjusted to ensure that the boundary must be larger than the effective mode volumes of optical WGMs[4]. Typically, the cavity mode volume is few micron if $|l-m| < 10$. The size of free triangle element is controlled within this boundary as shown in Fig. B.2(b). One of the FEM simulation results shows the radial component of E field on resonance under $|l-m| = 0$ and $s = 0$ (See Fig. B.2(c)). As seen here, the modal volume is a bit smaller than this boundary for finer mesh so that one can obtain accurate solutions through the COMSOL package.

[2]Suppose that two optical modes and a mechanical mode are interacting under the phase matching condition, so Brillouin scattering occurs in the end. Such phase matching condition can be written in the azimuthal order, $m_{\text{acoustic}} = m_{\text{pump}} - m_{\text{Stokes}}$. Here, m_{acoustic}, m_{pump}, and m_{Stokes} are the acoustic m-number, pump and Stokes scattering modes, respectively. Consequently, the acoustic azimuthal order is typically much smaller than the optical azimuthal orders.

[3]The optical m number in WGM resonators can be defined by $m = kr = \frac{n2\pi r}{\lambda}$, where r is the radius of resonators, and k is the wavenumber. Suppose that light propagates along the resonator whose radius is 100 μm at C-band, so the azimuthal order is around 570.

[4]In WGMs, the effective mode volume is defined by $V_{\text{eff}} = \frac{\int_V \epsilon |E|^2 dV}{max[\epsilon |E|^2]}$, where the integral volume V is the volume that EM fields are confined [195].

Here, it is important to compare the numerical solution to the analytic one which is described in Eq. (A.5). The analytic solution is given under the continuous condition in Eq.(2.2). Note that however this solution can only give eigenfunctions so that this result should be normalized as illustrated in Fig. B.3. As the line

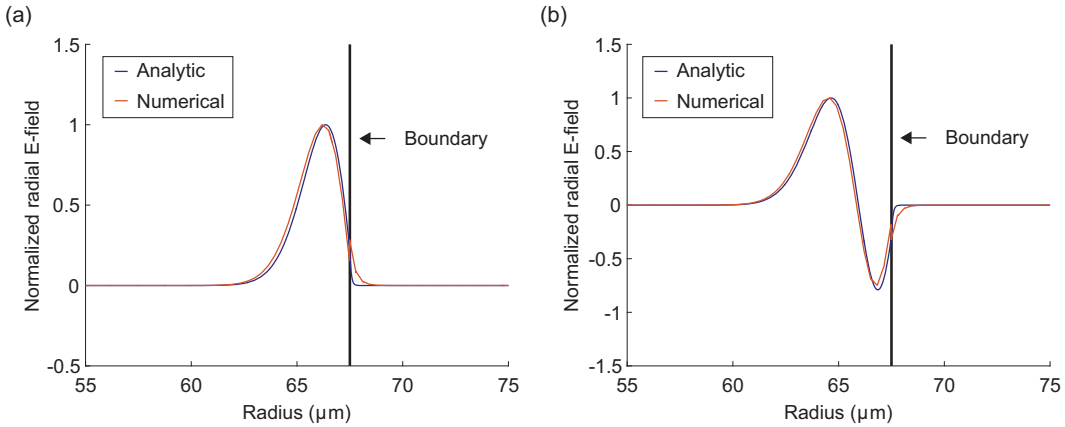

Figure B.3: Comparison of the analytic solutions to the numerical results. In both figures, we set the boundary for a sphere resonator at 67.5 μm. (a) The fundamental mode ($s = 1$) represented at $l = 382$. (b) The second-order mode ($s = 2$) represented at $l = 372$. Note that the azimuthal order m cannot affect the mode shape.

cuts through the resonator, the 1D numerical results are extracted from the FEM solutions. These numerical results are well fit to the analytic solutions in the silica resonator with 67.5 μm radius as shown in Fig. B.3.

Appendix C

Derivation of optical Q-factor

In Chapter 2, we discussed that an optical Q-factor is inversely proportional to the optical loss rate κ as presented in Eq. (2.5). To derive Eq. (2.5), we consider a simple equation of motion for an optical mode.

$$\frac{da(t)}{dt} = -\left(\frac{\kappa}{2} + i\omega_o\right) a. \tag{C.1}$$

Here, let us suppose that the optical mode a is initially excited as $a(0) = a_o$ and there is no external input for the sake of convenience. Now, the dimensionless energy of the optical mode a is readily given by $E(t) = a(t)a(t)^*$. To obtain dissipated energy per cycle, we should take a derivative on the energy.

$$\begin{aligned}\frac{dE}{dt} &= \frac{da(t)}{dt}a^*(t) + a(t)\frac{da^*(t)}{dt} \\ &= -\left(\frac{\kappa}{2} + i\omega_o\right) a(t)a^*(t) - \left(\frac{\kappa}{2} - i\omega_o\right) a(t)a^*(t) = -\kappa a(t)a^*(t)\end{aligned} \tag{C.2}$$

Therefore, the dissipated energy per cycle becomes

$$\Delta E = -\int_0^T \frac{dE(t)}{dt}dt = \kappa T a(t)a^*(t) = \kappa\frac{2\pi}{\omega_o}a(t)a^*(t) \tag{C.3}$$

where T is the cycle or period. As a result, one can get an optical Q-factor very easily.

$$Q = \frac{E}{\Delta E}2\pi = \frac{\omega_o}{\kappa}. \tag{C.4}$$

Bibliography

[1] G. A. Kao, K. C.; Hockham, "Dielectric-fibre surface waveguides for optical frequencies," *Proc. IEE.*, vol. 113, no. 7, pp. 1151–166, July 1966.

[2] J. Jackson, *Classical Electrodynamics*, 3rd ed. Wiley, 1999.

[3] J. A. Ogilvy, *Theory of wave scattering from random rough surfaces.* Adam Hilger, Bristol, Philadelphia, and New York, 1991.

[4] K. A. O'Donnell and E. R. Mendez, "Experimental study of scattering from characterized random surfaces," *J. Opt. Soc. Am. A*, vol. 4, no. 7, pp. 1194–1205, Jul 1987.

[5] A. Maradudin, T. Michel, A. McGurn, and E. Méndez, "Enhanced backscattering of light from a random grating," *Annals of Physics*, vol. 203, no. 2, pp. 255 – 307, 1990.

[6] M. L. Gorodetsky, A. D. Pryamikov, and V. S. Ilchenko, "Rayleigh scattering in high-Q microspheres," *J. Opt. Soc. Am. B*, vol. 17, no. 6, pp. 1051–1057, Jun 2000.

[7] L. Knopoff and J. A. Hudson, "Scattering of elastic waves by small inhomogeneities," *The Journal of the Acoustical Society of America*, vol. 36, no. 2, pp. 338–343, Feb. 1964.

[8] Y. H. Pao and V. Varatharajulu, "Huygens Principle, Radiation Conditions, and Integral Formulas for Scattering of Elastic-Waves," *Journal of the Acoustical Society of America*, vol. 59, no. 6, pp. 1361–1371, 1976.

[9] D. Marcuse, "Mode conversion caused by surface imperfections of a dielectric slab waveguide," *Bell Syst. Tech. J*, vol. 48, no. 10, pp. 3187–3215, 1969.

[10] D. Pinnow, T. Rich, F. Ostermayer, and M. DiDomenico, "Fundamental optical attenuation limits in the liquid and glassy state with application to fiber optical waveguide materials," *Applied Physics Letters*, vol. 22, no. 10, pp. 527–529, 1973.

[11] D. S. Weiss, V. Sandoghdar, J. Hare, V. Lefèvre-Seguin, J.-M. Raimond, and S. Haroche, "Splitting of high-Q Mie modes induced by light backscattering in silica microspheres," *Opt. Lett.*, vol. 20, no. 18, pp. 1835–1837, Sep 1995.

[12] D. Jalas, A. Petrov, M. Eich, W. Freude, S. Fan, Z. Yu, R. Baets, M. Popovic, A. Melloni, J. D. Joannopoulos, M. Vanwolleghem, C. R. Doerr, and H. Renner, "What is and what is not an optical isolator," *Nature Photon.*, vol. 7, no. 8, pp. 579–582, Aug. 2013.

[13] A. A. Golubentsev, "Suppression of interference effects in multiple scattering of light," *Sov. Phys. JETP*, vol. 59, no. 1, p. 26, Janunary 1984.

[14] F. C. MacKintosh and S. John, "Coherent backscattering of light in the presence of time-reversal-noninvariant and parity-nonconserving media," *Phys. Rev. B*, vol. 37, pp. 1884–1897, Feb 1988.

[15] R. Lenke and G. Maret, "Magnetic field effects on coherent backscattering of light," *The European Physical Journal B-Condensed Matter and Complex Systems*, vol. 17, no. 1, pp. 171–185, Sep 2000.

[16] M. Büttiker, "Absence of backscattering in the quantum hall effect in multiprobe conductors," *Phys. Rev. B*, vol. 38, pp. 9375–9389, Nov 1988.

[17] Z. Wang, Y. Chong, J. D. Joannopoulos, and M. Soljacic, "Observation of unidirectional backscattering-immune topological electromagnetic states," *Nature*, vol. 461, no. 7265, pp. 772–775, Aug. 2009.

[18] J. Kim, M. C. Kuzyk, K. Han, H. Wang, and G. Bahl, "Non-reciprocal Brillouin scattering induced transparency," *Nat. Phys.*, vol. 11, no. 3, pp. 275–280, Mar. 2015.

[19] C.-H. Dong, Z. Shen, C.-L. Zou, Y.-L. Zhang, W. Fu, and G.-C. Guo, "Brillouin-scattering-induced transparency and non-reciprocal light storage," *Nat. Commun.*, vol. 6, p. 6193, Feb. 2015.

[20] J. Kim, S. Kim, and G. Bahl, "Complete linear optical isolation at the microscale with ultralow loss," *Sci. Rep.*, vol. 7, no. 1, p. 1647, 2017.

[21] G. Bahl, J. Zehnpfennig, M. Tomes, and T. Carmon, "Stimulated optomechanical excitation of surface acoustic waves in a microdevice," *Nature Communications*, vol. 2, p. 403, Jul. 2011.

[22] M. S. Kang, A. Butsch, and P. S. J. Russell, "Reconfigurable light-driven opto-acoustic isolators in photonic crystal fibre," *Nature Photonics*, vol. 5, p. 549, Aug. 2011.

[23] S. Kim, X. Xu, J. M. Taylor, and G. Bahl, "Dynamically induced robust phonon transport and chiral cooling in an optomechanical system," *Nat. Commun.*, vol. 8, no. 1, p. 205, 2017.

[24] S. Kim, J. M. Taylor, and G. Bahl, "Dynamic suppression of rayleigh light scattering in dielectric resonators," *arXiv.org*, 2018, arXiv:1803.02366.

[25] D. B. Sohn, S. Kim, and G. Bahl, "Time-reversal symmetry breaking with acoustic pumping of nanophotonic circuits," *Nature Photonics*, vol. 12, no. 2, pp. 91–97, 2018.

[26] Y.-C. Chen, S. Kim, and G. Bahl, "Brillouin cooling in a linear waveguide," *New Journal of Physics*, vol. 18, no. 115004, Nov 2016.

[27] E. A. Kittlaus, H. Shin, and P. T. Rakich, "Large Brillouin amplification in silicon," *Nature Photon.*, vol. 10, pp. 463–468, Jun. 2016.

[28] S. Kim and G. Bahl, "Role of optical density of states in brillouin optomechanical cooling," *Opt. Express*, vol. 25, no. 2, pp. 776–784, Jan 2017.

[29] J. W. S. Rayleigh, *The Theory of Sound*, 1st ed. London, MacMillan, 1878, vol. 12.

[30] B. E. Saleh and M. C. Teich, *Fundamentals of photonics*. Wiley-Interscience, 2007.

[31] K. J. Vahala, "Optical microcavities," *Nature*, vol. 424, p. 839, Aug. 2003.

[32] R. D. Richtmyer, "Dielectric resonators," *Journal of Applied Physics*, vol. 10, no. 6, pp. 391–398, 1939.

[33] V. Braginsky, M. Gorodetsky, and V. Ilchenko, "Quality-factor and nonlinear properties of optical whispering-gallery modes," *Physics Letters A*, vol. 137, no. 7, pp. 393 – 397, 1989.

[34] T. Aoki, B. Dayan, E. Wilcut, W. P. Bowen, A. S. Parkins, T. J. Kippenberg, K. J. Vahala, and H. J. Kimble, "Observation of strong coupling between one atom and a monolithic microresonator," *Nature*, vol. 443, no. 7112, pp. 671–674, Oct. 2006.

[35] P. Del'Haye, A. Schliesser, O. Arcizet, T. Wilken, R. Holzwarth, and T. J. Kippenberg, "Optical frequency comb generation from a monolithic microresonator," *Nature*, vol. 450, p. 1214, Dec. 2007.

[36] T. J. Kippenberg, R. Holzwarth, and S. A. Diddams, "Microresonator-based optical frequency combs," *Science*, vol. 332, no. 6029, pp. 555–559, 2011.

[37] S. B. Papp, K. Beha, P. Del'Haye, F. Quinlan, H. Lee, K. J. Vahala, and S. A. Diddams, "Microresonator frequency comb optical clock," *Optica*, vol. 1, no. 1, pp. 10–14, Jul 2014.

[38] F. Vollmer and S. Arnold, "Whispering-gallery-mode biosensing: label-free detection down to single molecules," *Nature Methods*, vol. 5, p. 591, Jun. 2008.

[39] G. Righini, G. Conti, S. Soria, Y. Dumeige, P. Feron, M. Ferrari, and D. Ristic, "Whispering gallery mode micro resonators: Fundamentals and applications," *Rivista del Nuovo Cimento della Societa Italiana di Fisica*, vol. 34, no. 7, pp. 435–488, 2011.

[40] S. Schiller and R. L. Byer, "High-resolution spectroscopy of whispering gallery modes in large dielectric spheres," *Opt. Lett.*, vol. 16, no. 15, pp. 1138–1140, Aug 1991.

[41] S. V. Boriskina, P. Sewell, T. M. Benson, and A. I. Nosich, "Accurate simulation of two-dimensional optical microcavities with uniquely solvable boundary integral equations and trigonometric galerkin discretization," *J. Opt. Soc. Am. A*, vol. 21, no. 3, pp. 393–402, Mar 2004.

[42] A. B. Matsko and V. S. Ilchenko, "Optical resonators with whispering-gallery modes-part i: basics," *IEEE Journal of Selected Topics in Quantum Electronics*, vol. 12, no. 1, pp. 3–14, Jan 2006.

[43] M. Abramowitz and C. A. Stegun, Eds., *Handook of Mathematical Functions with FormulaHandbook of Mathematical Functions: with Formulas, Graphs, and Mathematical Tables*, 9th ed. New York: Dover, 1972.

[44] C. C. Lam, P. T. Leung, and K. Young, "Explicit asymptotic formulas for the positions, widths, and strengths of resonances in mie scattering," *J. Opt. Soc. Am. B*, vol. 9, no. 9, pp. 1585–1592, Sep 1992.

[45] M. L. Gorodetsky and A. E. Fomin, "Geometrical theory of whispering-gallery modes," *IEEE Journal of Selected Topics in Quantum Electronics*, vol. 12, no. 1, pp. 33–39, Jan 2006.

[46] G. Schunk, J. U. Fürst, M. Förtsch, D. V. Strekalov, U. Vogl, F. Sedlmeir, H. G. L. Schwefel, G. Leuchs, and C. Marquardt, "Identifying modes of large whispering-gallery mode resonators from the spectrum and emission pattern," *Opt. Express*, vol. 22, no. 25, pp. 30 795–30 806, Dec 2014.

[47] M. L. Gorodetsky, A. A. Savchenkov, and V. S. Ilchenko, "Ultimate q of optical microsphere resonators," *Opt. Lett.*, vol. 21, no. 7, pp. 453–455, Apr 1996.

[48] G. S. Agarwal and S. S. Jha, "Multimode phonon cooling via three-wave parametric interactions with optical fields," *Phys. Rev. A*, vol. 88, p. 013815, Jul 2013.

[49] H. A. Haus, *Waves and Fields in Optoelectronics*. Prentice-Hall, 1984.

[50] C. W. Gardiner and P. Zoller, *Quantum noise: a handbook of Markovian and non-Markovian quantum stochastic methods with applications to quantum optics*, 3rd ed. Springer Science & Business Media, 2004, vol. 56.

[51] M. Aspelmeyer, T. J. Kippenberg, and F. Marquardt, "Cavity optomechanics," *Rev. Mod. Phys.*, vol. 86, pp. 1391–1452, Dec 2014.

[52] M. L. Gorodetsky and V. S. Ilchenko, "Optical microsphere resonators: optimal coupling to high-q whispering-gallery modes," *J. Opt. Soc. Am. B*, vol. 16, no. 1, pp. 147–154, Jan 1999.

[53] A. Serpengüzel, S. Arnold, and G. Griffel, "Excitation of resonances of microspheres on an optical fiber," *Opt. Lett.*, vol. 20, no. 7, pp. 654–656, Apr 1995.

[54] M. Cai, O. Painter, and K. J. Vahala, "Observation of critical coupling in a fiber taper to a silica-microsphere whispering-gallery mode system," *Phys. Rev. Lett.*, vol. 85, pp. 74–77, Jul 2000.

[55] I. L. Fabelinskii, *Molecular scattering of light*. Plenum, New York, 1968.

[56] R. W. Boyd, *Nonlinear Optics*, 3rd ed. Academic Press, 2008.

[57] G. P. Agrawal, *Nonlinear Fiber Optics*, 5th ed. Academic Press, 2013.

[58] R. G. Smith, "Optical power handling capacity of low loss optical fibers as determined by stimulated raman and brillouin scattering," *Appl. Opt.*, vol. 11, no. 11, pp. 2489–2494, Nov 1972.

[59] A. Kobyakov, M. Sauer, and D. Chowdhury, "Stimulated brillouin scattering in optical fibers," *Adv. Opt. Photon.*, vol. 2, no. 1, pp. 1–59, Mar 2010.

[60] B. J. Eggleton, C. G. Poulton, and R. Pant, "Inducing and harnessing stimulated brillouin scattering in photonic integrated circuits," *Adv. Opt. Photon.*, vol. 5, no. 4, pp. 536–587, Dec 2013.

[61] K. O. Hill, B. S. Kawasaki, and D. C. Johnson, "cw brillouin laser," *Applied Physics Letters*, vol. 28, no. 10, pp. 608–609, 1976.

[62] M. Tomes and T. Carmon, "Photonic micro-electromechanical systems vibrating at x-band (11-ghz) rates," *Phys. Rev. Lett.*, vol. 102, p. 113601, Mar 2009.

[63] I. S. Grudinin, A. B. Matsko, and L. Maleki, "Brillouin lasing with a caf_2 whispering gallery mode resonator," *Phys. Rev. Lett.*, vol. 102, p. 043902, Jan 2009.

[64] N. T. Otterstrom, R. O. Behunin, E. A. Kittlaus, Z. Wang, and P. T. Rakich, "A silicon brillouin laser," *Science*, vol. 360, no. 6393, pp. 1113–1116, 2018.

[65] T. Kurashima, T. Horiguchi, and M. Tateda, "Distributed-temperature sensing using stimulated brillouin scattering in optical silica fibers," *Opt. Lett.*, vol. 15, no. 18, pp. 1038–1040, Sep 1990.

[66] M. González-Herráez, K.-Y. Song, and L. Thévenaz, "Optically controlled slow and fast light in optical fibers using stimulated brillouin scattering," *Applied Physics Letters*, vol. 87, no. 8, p. 081113, 2005.

[67] Y. Okawachi, M. S. Bigelow, J. E. Sharping, Z. Zhu, A. Schweinsberg, D. J. Gauthier, R. W. Boyd, and A. L. Gaeta, "Tunable all-optical delays via brillouin slow light in an optical fiber," *Phys. Rev. Lett.*, vol. 94, p. 153902, Apr 2005.

[68] G. Bahl, M. Tomes, F. Marquardt, and T. Carmon, "Observation of spontaneous brillouin cooling," *Nature Physics*, vol. 8, p. 203, Jan. 2012.

[69] Z. Zhu, D. J. Gauthier, and R. W. Boyd, "Stored light in an optical fiber via stimulated brillouin scattering," *Science*, vol. 318, no. 5857, pp. 1748–1750, 2007.

[70] M. Merklein, B. Stiller, K. Vu, S. J. Madden, and B. J. Eggleton, "A chip-integrated coherent photonic-phononic memory," *Nature Communications*, vol. 8, no. 1, p. 574, 2017.

[71] L. Brillouin, "Diffusion de la lumière et des rayons x par un corps transparent homogène - influence de l'agitation thermique," *Ann. Phys.*, vol. 9, no. 17, pp. 88–122, 1922.

[72] F.-K. L.I. Mandelstam, Zh. Russ, "Light scattering by inhomogeneous media," *Ova.*, vol. 58, no. 381, 1926.

[73] R. Y. Chiao, C. H. Townes, and B. P. Stoicheff, "Stimulated brillouin scattering and coherent generation of intense hypersonic waves," *Phys. Rev. Lett.*, vol. 12, pp. 592–595, May 1964.

[74] R. M. Shelby, M. D. Levenson, and P. W. Bayer, "Guided acoustic-wave brillouin scattering," *Phys. Rev. B*, vol. 31, pp. 5244–5252, Apr 1985.

[75] R. M. Shelby, M. D. Levenson, and P. W. Bayer, "Resolved forward brillouin scattering in optical fibers," *Phys. Rev. Lett.*, vol. 54, pp. 939–942, Mar 1985.

[76] K. C. Schwab and M. L. Roukes, "Putting mechanics into quantum mechanics," *Physics Today*, vol. 58, no. 7, pp. 36–42, 2005.

[77] M. S. Kang, A. Nazarkin, A. Brenn, and P. S. J. Russell, "Tightly trapped acoustic phonons in photonic crystal fibres as highly nonlinear artificial raman oscillators," *Nature Physics*, vol. 5, p. 276, Mar. 2009.

[78] H. Shin, W. Qiu, R. Jarecki, J. A. Cox, R. H. Olsson III, A. Starbuck, Z. Wang, and P. T. Rakich, "Tailorable stimulated brillouin scattering in nanoscale silicon waveguides," *Nature Communications*, vol. 4, p. 1944, Jun. 2013.

[79] P. T. Rakich, C. Reinke, R. Camacho, P. Davids, and Z. Wang, "Giant enhancement of stimulated brillouin scattering in the subwavelength limit," *Phys. Rev. X*, vol. 2, p. 011008, Jan 2012.

[80] M. S. Kang, A. Brenn, and P. St.J. Russell, "All-optical control of gigahertz acoustic resonances by forward stimulated interpolarization scattering in a photonic crystal fiber," *Phys. Rev. Lett.*, vol. 105, p. 153901, Oct 2010.

[81] E. A. Kittlaus, N. T. Otterstrom, and P. T. Rakich, "On-chip inter-modal brillouin scattering," *Nature Communications*, vol. 8, p. 15819, Jul. 2017.

[82] N. T. Otterstrom, R. O. Behunin, E. A. Kittlaus, and P. T. Rakich, "Optomechanical cooling in a continuous system," *arXiv.org*, 2018, arXiv:1805.02502.

[83] N. Dostart, S. Kim, and G. Bahl, "Giant gain enhancement in surface-confined resonant stimulated brillouin scattering," *Laser & Photonics Reviews*, vol. 9, no. 6, pp. 689–705, 2015.

[84] R. Loudon, *The Quantum Theory of Light*, 3rd ed. Oxford Science Publications, 2010.

[85] X. Xu, S. Kim, G. Bahl, and J. M. Taylor, "A quasi-mode theory of chiral phonons," *arXiv.org*, Dec 2016, arXiv:1612.09240.

[86] L. Mandel and E. Wolf, *Optical Coherence and Quantum Optics*. Cambridge University Press, 1995.

[87] W. P. Bowen and G. J. Milburn, *Quantum Optomechanics*. CRC Press, 2016.

[88] M. L. Gorodetsky and I. S. Grudinin, "Fundamental thermal fluctuations in microspheres," *J. Opt. Soc. Am. B*, vol. 21, no. 4, pp. 697–705, Apr 2004.

[89] R. Apetz and M. P. B. Bruggen, "Transparent alumina: A light-scattering model," *Journal of the American Ceramic Society*, vol. 86, no. 3, pp. 480–486, 2003.

[90] E. A. J. Marcatili and S. E. Miller, "Improved relations describing directional control in electromagnetic wave guidance," *The Bell System Technical Journal*, vol. 48, no. 7, pp. 2161–2188, Sept 1969.

[91] F. P. Kapron, D. B. Keck, and R. D. Maurer, "Radiation losses in glass optical waveguides," *Applied Physics Letters*, vol. 17, no. 10, pp. 423–425, 1970.

[92] J. C. Knight, G. Cheung, F. Jacques, and T. A. Birks, "Phase-matched excitation of whispering-gallery-mode resonances by a fiber taper," *Opt. Lett.*, vol. 22, no. 15, pp. 1129–1131, Aug 1997.

[93] A. H. Safavi-Naeini and O. Painter, "Proposal for an optomechanical traveling wave phonon-photon translator," *New Journal of Physics*, vol. 13, no. 1, p. 013017, 2011.

[94] R. Wolfe, J. F. Dillon, R. A. Lieberman, and V. J. Fratello, "Broadband magneto-optic waveguide isolator," *Appl. Phys. Lett.*, vol. 57, no. 10, pp. 960–962, 1990.

[95] J. Ballato and E. Snitzer, "Fabrication of fibers with high rare-earth concentrations for Faraday isolator applications," *Appl. Optics*, vol. 34, no. 30, pp. 6848–6854, Oct 1995.

[96] M.-C. Tien, T. Mizumoto, P. Pintus, H. Kromer, and J. E. Bowers, "Silicon ring isolators with bonded nonreciprocal magneto-optic garnets," *Opt. Express*, vol. 19, no. 12, pp. 11 740–11 745, Jun 2011.

[97] L. Bi, J. Hu, P. Jiang, D. H. Kim, G. F. Dionne, L. C. Kimerling, and C. A. Ross, "On-chip optical isolation in monolithically integrated non-reciprocal optical resonators," *Nature Photon.*, vol. 5, no. 12, pp. 758–762, Dec. 2011.

[98] Y. Shoji, T. Mizumoto, H. Yokoi, I.-W. Hsieh, and R. M. Osgood, "Magneto-optical isolator with silicon waveguides fabricated by direct bonding," *Appl. Phys. Lett.*, vol. 92, no. 7, 2008.

[99] T. Goto, M. C. Onbaşli, and C. A. Ross, "Magneto-optical properties of cerium substituted yttrium iron garnet films with reduced thermal budget for monolithic photonic integrated circuits," *Opt. Express*, vol. 20, no. 27, pp. 28 507–28 517, Dec 2012.

[100] Z. Yu and S. Fan, "Complete optical isolation created by indirect interband photonic transitions," *Nature Photon.*, vol. 3, no. 2, pp. 91–94, Feb. 2009.

[101] C. G. Poulton, R. Pant, A. Byrnes, S. Fan, M. J. Steel, and B. J. Eggleton, "Design for broadband on-chip isolator using stimulated Brillouin scattering in dispersion-engineered chalcogenide waveguides," *Opt. Express*, vol. 20, no. 19, pp. 21 235–21 246, Sep 2012.

[102] K. Fang, Z. Yu, and S. Fan, "Photonic Aharonov-Bohm Effect Based on Dynamic Modulation," *Phys. Rev. Lett.*, vol. 108, no. 15, p. 153901, Apr. 2012.

[103] X. Zhu, L. Feng, P. Zhang, X. Yin, and X. Zhang, "One-way invisible cloak using parity-time symmetric transformation optics," *Opt. Lett.*, vol. 38, no. 15, pp. 2821–2824, 2013.

[104] D. L. Sounas, C. Caloz, and A. Alu, "Giant non-reciprocity at the subwavelength scale using angular momentum-biased metamaterials," *Nature Commun.*, vol. 4, no. 2407, Sep. 2013.

[105] D. L. Sounas and A. Alu, "Angular-momentum-biased nanorings to realize magnetic-free integrated optical isolation," *ACS Photonics*, vol. 1, no. 3, pp. 198–204, Mar. 2014.

[106] H. Lira, Z. Yu, S. Fan, and M. Lipson, "Electrically driven nonreciprocity induced by interband photonic transition on a silicon chip," *Phys. Rev. Lett.*, vol. 109, p. 033901, Jul 2012.

[107] L. Fan, J. Wang, L. T. Varghese, H. Shen, B. Niu, Y. Xuan, A. M. Weiner, and M. Qi, "An All-Silicon Passive Optical Diode," *Science*, vol. 335, no. 6067, pp. 447–450, Jan. 2012.

[108] L. D. Tzuang, K. Fang, P. Nussenzveig, S. Fan, and M. Lipson, "Non-reciprocal phase shift induced by an effective magnetic flux for light," *Nat. Photon.*, vol. 8, p. 701, Aug. 2014.

[109] B. Peng, a. K. Özdemir, F. Lei, F. Monifi, M. Gianfreda, G. L. Long, S. Fan, F. Nori, C. M. Bender, and L. Yang, "Parity-time-symmetric whispering-gallery microcavities," *Nat. Phys.*, vol. 10, p. 394, Apr. 2014.

[110] C. Sayrin, C. Junge, R. Mitsch, B. Albrecht, D. O'Shea, P. Schneeweiss, J. Volz, and A. Rauschenbeutel, "Nanophotonic optical isolator controlled by the internal state of cold atoms," *Phys. Rev. X*, vol. 5, p. 041036, Dec 2015.

[111] Y. Shi, Z. Yu, and S. Fan, "Limitations of nonlinear optical isolators due to dynamic reciprocity," *Nature Photon.*, vol. 9, no. 6, pp. 388–392, May 2015.

[112] X. Huang and S. Fan, "Complete all-optical silica fiber isolator via stimulated brillouin scattering," *J. Lightwave Technol.*, vol. 29, no. 15, pp. 2267–2275, Aug 2011.

[113] R. Van Laer, B. Kuyken, D. Van Thourhout, and R. Baets, "Interaction between light and highly confined hypersound in a silicon photonic nanowire," *Nature Photon.*, vol. 9, pp. 199–203, Mar. 2015.

[114] Z. Shen, Y.-L. Zhang, Y. Chen, C.-L. Zou, Y.-F. Xiao, X.-B. Zou, F.-W. Sun, G.-C. Guo, and C.-H. Dong, "Experimental realization of optomechanically induced non-reciprocity," *Nat. Photon.*, vol. 10, p. 657, Aug. 2016.

[115] A. H. Safavi-Naeini, T. P. M. Alegre, J. Chan, M. Eichenfield, M. Winger, Q. Lin, J. T. Hill, D. E. Chang, and O. Painter, "Electromagnetically induced transparency and slow light with optomechanics," *Nature*, vol. 472, no. 7341, pp. 69–73, Apr. 2011.

[116] S. Weis, R. Rivière, S. Deléglise, E. Gavartin, O. Arcizet, A. Schliesser, and T. J. Kippenberg, "Optomechanically induced transparency," *Science*, vol. 330, no. 6010, pp. 1520–1523, 2010.

[117] J. D. Teufel, T. Donner, A. Castellanos-Beltran, M., J. W. Harlow, and K. W. Lehnert, "Nanomechanical motion measured with an imprecision below that at the standard quantum limit," *Nature Nanotech.*, vol. 4, no. 12, pp. 820–823, Dec. 2009.

[118] A. G. Krause, M. Winger, T. D. Blasius, Q. Lin, and O. Painter, "A high-resolution microchip optomechanical accelerometer," *Nature Photon.*, vol. 6, no. 11, pp. 768–772, Nov. 2012.

[119] E. Gavartin, P. Verlot, and T. J. Kippenberg, "A hybrid on-chip optomechanical transducer for ultrasensitive force measurements," *Nature Nanotech.*, vol. 7, no. 8, pp. 509–514, Aug. 2012.

[120] A. D. O'Connell, M. Hofheinz, M. Ansmann, R. C. Bialczak, M. Lenander, E. Lucero, M. Neeley, D. Sank, H. Wang, M. Weides, J. Wenner, J. M. Martinis, and A. N. Cleland, "Quantum ground state and single-phonon control of a mechanical resonator," *Nature*, vol. 464, no. 7289, pp. 697–703, Apr. 2010.

[121] M. Bagheri, M. Poot, M. Li, W. P. H. Pernice, and H. X. Tang, "Dynamic manipulation of nanomechanical resonators in the high-amplitude regime and non-volatile mechanical memory operation," *Nature Nanotech.*, vol. 6, no. 11, pp. 726–732, Nov. 2011.

[122] P. F. Cohadon, A. Heidmann, and M. Pinard, "Cooling of a mirror by radiation pressure," *Phys. Rev. Lett.*, vol. 83, pp. 3174–3177, Oct 1999.

[123] C. H. Metzger and K. Karrai, "Cavity cooling of a microlever," *Nature*, vol. 432, no. 7020, pp. 1002–1005, Dec. 2004.

[124] O. Arcizet, P.-F. Cohadon, T. Briant, M. Pinard, and A. Heidmann, "Radiation-pressure cooling and optomechanical instability of a micromirror," *Nature*, vol. 444, no. 7115, pp. 71–74, Nov 2006.

[125] S. Gigan, H. Bohm, M. Paternostro, F. Blaser, G. Langer, J. Hertzberg, K. Schwab, D. Bauerle, M. Aspelmeyer, and A. Zeilinger, "Self-cooling of a micromirror by radiation pressure," *Nature*, vol. 444, no. 7115, pp. 67–70, Nov 2006.

[126] A. Schliesser, P. Del'Haye, N. Nooshi, K. J. Vahala, and T. J. Kippenberg, "Radiation pressure cooling of a micromechanical oscillator using dynamical backaction," *Phys. Rev. Lett.*, vol. 97, p. 243905, Dec 2006.

[127] A. Schliesser, R. Riviere, G. Anetsberger, O. Arcizet, and T. J. Kippenberg, "Resolved-sideband cooling of a micromechanical oscillator," *Nature Phys.*, vol. 4, no. 5, pp. 415–419, May 2008.

[128] Y.-S. Park and H. Wang, "Resolved-sideband and cryogenic cooling of an optomechanical resonator," *Nature Phys.*, vol. 5, no. 7, pp. 489–493, Jul. 2009.

[129] J. Chan, T. P. M. Alegre, A. H. Safavi-Naeini, J. T. Hill, A. Krause, S. Groblacher, M. Aspelmeyer, and O. Painter, "Laser cooling of a nanomechanical oscillator into its quantum ground state," *Nature*, vol. 478, no. 7367, pp. 89–92, Oct. 2011.

[130] J. D. Teufel, T. Donner, D. Li, J. W. Harlow, M. S. Allman, K. Cicak, A. J. Sirois, J. D. Whittaker, K. W. Lehnert, and R. W. Simmonds, "Sideband cooling of micromechanical motion to the quantum ground state," *Nature*, vol. 475, no. 7356, pp. 359–363, Jul. 2011.

[131] T. P. Purdy, R. W. Peterson, and C. A. Regal, "Observation of radiation pressure shot noise on a macroscopic object," *Science*, vol. 339, no. 6121, pp. 801–804, 2013.

[132] J. D. Thompson, B. M. Zwickl, A. M. Jayich, F. Marquardt, S. M. Girvin, and J. G. E. Harris, "Strong dispersive coupling of a high-finesse cavity to a micromechanical membrane," *Nature*, vol. 452, no. 7183, pp. 72–75, Mar. 2008.

[133] A. M. Jayich, J. C. Sankey, B. M. Zwickl, C. Yang, J. D. Thompson, S. M. Girvin, A. A. Clerk, F. Marquardt, and J. G. E. Harris, "Dispersive optomechanics: a membrane inside a cavity," *New Journal of Physics*, vol. 10, no. 9, p. 095008, 2008.

[134] G. Heinrich, J. G. E. Harris, and F. Marquardt, "Photon shuttle: Landau-zener-stückelberg dynamics in an optomechanical system," *Phys. Rev. A*, vol. 81, p. 011801, Jan 2010.

[135] I. S. Grudinin, H. Lee, O. Painter, and K. J. Vahala, "Phonon laser action in a tunable two-level system," *Phys. Rev. Lett.*, vol. 104, p. 083901, Feb 2010.

[136] T. Carmon, L. Yang, and K. J. Vahala, "Dynamical thermal behavior and thermal self-stability of microcavities," *Opt. Express*, vol. 12, no. 20, pp. 4742–4750, Oct 2004.

[137] M. Tomes, F. Marquardt, G. Bahl, and T. Carmon, "Quantum-mechanical theory of optomechanical Brillouin cooling," *Physical Review A - Atomic, Molecular, and Optical Physics*, vol. 84, no. 6, 2011.

[138] A. A. Clerk, M. H. Devoret, S. M. Girvin, F. Marquardt, and R. J. Schoelkopf, "Introduction to quantum noise, measurement, and amplification," *Rev. Mod. Phys.*, vol. 82, pp. 1155–1208, Apr 2010.

[139] M. Hossein-Zadeh and K. J. Vahala, "Observation of optical spring effect in a microtoroidal optomechanical resonator," *Opt. Lett.*, vol. 32, no. 12, pp. 1611–1613, 2007.

[140] I. Wilson-Rae, N. Nooshi, J. Dobrindt, T. J. Kippenberg, and W. Zwerger, "Cavity-assisted backaction cooling of mechanical resonators," *New Journal of Physics*, vol. 10, no. 9, p. 095007, 2008.

[141] P. Rabl, C. Genes, K. Hammerer, and M. Aspelmeyer, "Phase-noise induced limitations on cooling and coherent evolution in optomechanical systems," *Phys. Rev. A*, vol. 80, p. 063819, Dec 2009.

[142] Y.-C. Liu, Y.-F. Xiao, X. Luan, and C. W. Wong, "Dynamic dissipative cooling of a mechanical resonator in strong coupling optomechanics," *Phys. Rev. Lett.*, vol. 110, no. 15, p. 153606, Apr. 2013.

[143] J. Li, X. Yi, H. Lee, S. A. Diddams, and K. J. Vahala, "Electro-optical frequency division and stable microwave synthesis," *Science*, vol. 345, no. 6194, pp. 309–313, 2014.

[144] W. Loh, A. A. S. Green, F. N. Baynes, D. C. Cole, F. J. Quinlan, H. Lee, K. J. Vahala, S. B. Papp, and S. A. Diddams, "Dual-microcavity narrow-linewidth brillouin laser," *Optica*, vol. 2, no. 3, pp. 225–232, Mar 2015.

[145] J. Chan, T. M. Alegre, A. H. Safavi-Naeini, J. T. Hill, A. Krause, S. Gröblacher, M. Aspelmeyer, and O. Painter, "Laser cooling of a nanomechanical oscillator into its quantum ground state," *Nature*, vol. 478, no. 7367, pp. 89–92, 2011.

[146] E. Verhagen, S. Deleglise, S. Weis, A. Schliesser, and T. J. Kippenberg, "Quantum-coherent coupling of a mechanical oscillator to an optical cavity mode," *Nature*, vol. 482, no. 7383, pp. 63–67, Feb. 2012.

[147] J. D. Teufel, T. Donner, M. A. Castellanos-Beltran, J. W. Harlow, and K. W. Lehnert, "Nanomechanical motion measured with an imprecision below that at the standard quantum limit," *Nat. Nanotech.*, vol. 4, no. 12, pp. 820–823, Nov. 2009.

[148] G. Anetsberger, E. Gavartin, O. Arcizet, Q. P. Unterreithmeier, E. M. Weig, M. L. Gorodetsky, J. P. Kotthaus, and T. J. Kippenberg, "Measuring nanomechanical motion with an imprecision below the standard quantum limit," *Phys. Rev. A*, vol. 82, p. 061804, Dec 2010.

[149] A. G. Krause, M. Winger, T. D. Blasius, Q. Lin, and O. Painter, "A high-resolution microchip optomechanical accelerometer," *Nat. Photonics*, vol. 6, no. 11, pp. 768–772, Oct. 2012.

[150] E. Gavartin, P. Verlot, and T. J. Kippenberg, "A hybrid on-chip optomechanical transducer for ultrasensitive force measurements," *Nat. Nanotech.*, vol. 7, pp. 509–514, Jun. 2012.

[151] B. I. Halperin, "Quantized hall conductance, current-carrying edge states, and the existence of extended states in a two-dimensional disordered potential," *Phys. Rev. B*, vol. 25, pp. 2185–2190, Feb 1982.

[152] M. Hafezi, S. Mittal, J. Fan, A. Migdall, and J. M. Taylor, "Imaging topological edge states in silicon photonics," *Nat. Photonics*, vol. 7, pp. 1001–1005, Oct. 2013.

[153] R. Süsstrunk and S. D. Huber, "Observation of phononic helical edge states in a mechanical topological insulator," *Science*, vol. 349, no. 6243, pp. 47–50, 2015.

[154] V. Peano, M. Houde, C. Brendel, F. Marquardt, and A. A. Clerk, "Topological phase transitions and chiral inelastic transport induced by the squeezing of light," *Nat. Commun.*, vol. 7, Mar. 2016.

[155] R. Fleury, D. L. Sounas, C. F. Sieck, M. R. Haberman, and A. Alu, "Sound Isolation and Giant Linear Nonreciprocity in a Compact Acoustic Circulator," *Science*, vol. 343, no. 6170, pp. 516–519, Jan. 2014.

[156] N. A. Estep, D. L. Sounas, J. Soric, and A. Alu, "Magnetic-free non-reciprocity and isolation based on parametrically modulated coupled-resonator loops," *Nat. Phys.*, vol. 10, no. 12, pp. 923–927, Nov. 2014.

[157] X. Xu, T. Purdy, and J. M. Taylor, "Cooling a harmonic oscillator by optomechanical modification of its bath," *Phys. Rev. Lett.*, vol. 118, p. 223602, May 2017.

[158] F. Marquardt, A. A. Clerk, and S. M. Girvin, "Quantum theory of optomechanical cooling," *J. Mod. Opt.*, vol. 55, no. 19-20, pp. 3329–3338, 2008.

[159] Y.-S. Park and H. Wang, "Resolved-sideband and cryogenic cooling of an optomechanical resonator," *Nat. Phys.*, vol. 5, no. 7, pp. 489–493, 2009.

[160] Y. Liu, H. Miao, V. Aksyuk, and K. Srinivasan, "Wide cantilever stiffness range cavity optomechanical sensors for atomic force microscopy," *Opt. Express*, vol. 20, no. 16, pp. 18 268–18 280, Jul 2012.

[161] R. W. Andrews, A. P. Reed, K. Cicak, J. D. Teufel, and K. W. Lehnert, "Quantum-enabled temporal and spectral mode conversion of microwave signals," *Nat. Commun.*, vol. 6, 11 2015.

[162] J. Bochmann, A. Vainsencher, D. D. Awschalom, and A. N. Cleland, "Nanomechanical coupling between microwave and optical photons," *Nat. Phys.*, vol. 9, no. 11, pp. 712–716, 11 2013.

[163] A. Mazzei, S. Götzinger, L. de S. Menezes, G. Zumofen, O. Benson, and V. Sandoghdar, "Controlled coupling of counterpropagating whispering-gallery modes by a single rayleigh scatterer: A classical problem in a quantum optical light," *Phys. Rev. Lett.*, vol. 99, p. 173603, Oct 2007.

[164] A. G. Griffith, R. K. W. Lau, J. Cardenas, Y. Okawachi, A. Mohanty, R. Fain, Y. H. D. Lee, M. Yu, C. T. Phare, C. B. Poitras, A. L. Gaeta, and M. Lipson, "Silicon-chip mid-infrared frequency comb generation," *Nat. Commun.*, vol. 6, p. 6299, Feb. 2015.

[165] M.-G. Suh, Q.-F. Yang, K. Y. Yang, X. Yi, and K. J. Vahala, "Microresonator soliton dual-comb spectroscopy," *Science*, vol. 354, no. 6312, pp. 600–603, 2016.

[166] T. Schwartz, G. Bartal, S. Fishman, and M. Segev, "Transport and Anderson localization in disordered two-dimensional photonic lattices," *Nature*, vol. 446, p. 52, Mar. 2007.

[167] P. Nagpal, N. C. Lindquist, S.-H. Oh, and D. J. Norris, "Ultrasmooth patterned metals for plasmonics and metamaterials," *Science*, vol. 325, no. 5940, pp. 594–597, 2009.

[168] F. Morichetti, A. Canciamilla, C. Ferrari, M. Torregiani, A. Melloni, and M. Martinelli, "Roughness induced backscattering in optical silicon waveguides," *Phys. Rev. Lett.*, vol. 104, p. 033902, Jan 2010.

[169] T. J. Kippenberg, A. L. Tchebotareva, J. Kalkman, A. Polman, and K. J. Vahala, "Purcell-factor-enhanced scattering from si nanocrystals in an optical microcavity," *Phys. Rev. Lett.*, vol. 103, p. 027406, Jul 2009.

[170] F. D. M. Haldane and S. Raghu, "Possible realization of directional optical waveguides in photonic crystals with broken time-reversal symmetry," *Phys. Rev. Lett.*, vol. 100, p. 013904, Jan 2008.

[171] M. C. Rechtsman, J. M. Zeuner, Y. Plotnik, Y. Lumer, D. Podolsky, F. Dreisow, S. Nolte, M. Segev, and A. Szameit, "Photonic Floquet topological insulators," *Nature*, vol. 496, p. 196, Apr. 2013.

[172] S. Groblacher, K. Hammerer, M. R. Vanner, and M. Aspelmeyer, "Observation of strong coupling between a micromechanical resonator and an optical cavity field," *Nature*, vol. 460, no. 7256, pp. 724–727, Aug. 2009.

[173] T. J. Kippenberg, S. M. Spillane, and K. J. Vahala, "Modal coupling in traveling-wave resonators," *Opt. Lett.*, vol. 27, no. 19, pp. 1669–1671, Oct 2002.

[174] A. B. Matsko and L. Maleki, "Bose-Hubbard hopping due to resonant Rayleigh scattering," *Opt. Lett.*, vol. 42, no. 22, pp. 4764–4767, Nov 2017.

[175] A. Yariv, "Universal relations for coupling of optical power between microresonators and dielectric waveguides," *Electron. Lett.*, vol. 36, no. 4, pp. 321–322, Feb 2000.

[176] J. D. Teufel, D. Li, M. S. Allman, K. Cicak, A. J. Sirois, J. D. Whittaker, and R. W. Simmonds, "Circuit cavity electromechanics in the strong-coupling regime," *Nature*, vol. 471, no. 7337, pp. 204–208, Mar. 2011.

[177] C. E. Rüter, K. G. Makris, R. El-Ganainy, D. N. Christodoulides, M. Segev, and D. Kip, "Observation of parity-time symmetry in optics," *Nat. Phys.*, vol. 6, p. 192, Jan. 2010.

[178] C. Wolff, M. J. Steel, B. J. Eggleton, and C. G. Poulton, "Stimulated Brillouin scattering in integrated photonic waveguides: Forces, scattering mechanisms, and coupled-mode analysis," *Phys. Rev. A*, vol. 92, p. 013836, Jul 2015.

[179] P. Kharel, R. Behunin, W. Renninger, and P. Rakich, "Noise and dynamics in forward Brillouin interactions," *Physical Review A*, vol. 93, no. 6, p. 063806, 2016.

[180] J. Sipe and M. Steel, "A hamiltonian treatment of stimulated brillouin scattering in nanoscale integrated waveguides," *New Journal of Physics*, vol. 18, no. 4, p. 045004, 2016.

[181] R. W. Boyd, K. Rzaẹwski, and P. Narum, "Noise initiation of stimulated brillouin scattering," *Phys. Rev. A*, vol. 42, pp. 5514–5521, Nov 1990.

[182] H. Shin, W. Qiu, R. Jarecki, J. A. Cox, R. H. Olsson III, A. Starbuck, Z. Wang, and P. T. Rakich, "Tailorable stimulated Brillouin scattering in nanoscale silicon waveguides," *Nature communications*, vol. 4, 2013.

[183] R. Van Laer, B. Kuyken, D. Van Thourhout, and R. Baets, "Interaction between light and highly confined hypersound in a silicon photonic nanowire," *Nature Photonics*, vol. 9, no. 3, pp. 199–203, 2015.

[184] R. Van Laer, A. Bazin, B. Kuyken, R. Baets, and D. Van Thourhout, "Net on-chip Brillouin gain based on suspended silicon nanowires," *New Journal of Physics*, vol. 17, no. 11, p. 115005, 2015.

[185] Y. Vlasov and S. McNab, "Losses in single-mode silicon-on-insulator strip waveguides and bends," *Optics Express*, vol. 12, no. 8, pp. 1622–1631, 2004.

[186] R. Tabrizian, M. Rais-Zadeh, and F. Ayazi, "Effect of phonon interactions on limiting the fQ product of micromechanical resonators," in *IEEE International Solid-State Sensors, Actuators and Microsystems Conference*, 2009, pp. 2131–2134.

[187] A. Butsch, J. Koehler, R. Noskov, and P. S. J. Russell, "CW-pumped single-pass frequency comb generation by resonant optomechanical nonlinearity in dual-nanoweb fiber," *Optica*, vol. 1, no. 3, pp. 158–164, 2014.

[188] R. Hui and M. O'Sullivan, *Fiber optic measurement techniques*. Academic Press, 2009.

[189] C. Dong, V. Fiore, M. C. Kuzyk, and H. Wang, "Optomechanical dark mode." *Science*, vol. 338, no. 6114, pp. 1609–1613, Dec. 2012.

[190] K. Fang, J. Luo, A. Metelmann, M. H. Matheny, F. Marquardt, A. A. Clerk, and O. Painter, "Generalized non-reciprocity in an optomechanical circuit via synthetic magnetism and reservoir engineering," *Nat. Phys*, vol. 13, no. 5, pp. 465–471, 2017.

[191] F. Ruesink, M.-A. Miri, A. Alù, and E. Verhagen, "Nonreciprocity and magnetic-free isolation based on optomechanical interactions," *Nature Communications*, vol. 7, p. 13662, Nov. 2016.

[192] L. Fan, C.-L. Zou, M. Poot, R. Cheng, X. Guo, X. Han, and H. X. Tang, "Integrated optomechanical single-photon frequency shifter," *Nat. Photonics*, vol. 10, no. 12, pp. 766–770, 2016.

[193] L.-W. Luo, N. Ophir, C. P. Chen, L. H. Gabrielli, C. B. Poitras, K. Bergmen, and M. Lipson, "WDM-compatible mode-division multiplexing on a silicon chip," *Nat. Commun.*, vol. 5, p. 3069, 2014.

[194] S. Johnson, "Notes on perfectly matched layers," Massachusetts Institute of Technology, Cambridge, Tech. Rep., 2010.

[195] K. Srinivasan, M. Borselli, O. Painter, A. Stintz, and S. Krishna, "Cavity q, mode volume, and lasing threshold in small diameter algaas microdisks with embedded quantum dots," *Opt. Express*, vol. 14, no. 3, pp. 1094–1105, Feb 2006.